© 2010 Kirk A. Strebel

SIMULATIONS OF THERMOPHORETIC DEPOSITION IN WAVY CHANNELS

BY

KIRK A. STREBEL

THESIS

Submitted in partial fulfillment of the requirements
for the degree of Master of Science in Mechanical Engineering
in the Graduate College of the
University of Illinois at Urbana-Champaign, 2010

Urbana, Illinois

Adviser:

Professor S. Pratap Vanka

Abstract

The use of exhaust gas recirculation coolers is important for minimization of harmful NO_x emissions from large diesel engines. But the use of the soot filled exhaust leads to the deposition of particles on the fins of the EGR cooler. So it is important to understand the soot deposition mechanisms and geometry effects in order to design an efficient fin geometry that minimizes soot deposition. This study developed a fully implicit code with variable property consideration and boundary fitter coordinates to model the fluid flow, heat transfer, and soot deposition in wavy channels. The code was then used to study laminar and turbulent flow with Reynolds numbers ranging from 300 to 10,000. The inlet fluid temperature was held at 750 K and the wall temperature was varied from 300 K to 750 K.

The first set of results is for laminar flow in a wavy channel. Three Reynolds numbers and four wall temperatures were studied for a single wavy geometry. The pressure drop, heat transfer, and soot deposition were predicted for all cases and trends are described. Then the effect of geometry on the pressure drop, heat transfer, and soot deposition in a laminar flow is studied. This is done by comparing the wavy channel results with planar channel results for one Reynolds number and three different wall temperatures.

The second set of results is for turbulent flow in a wavy channel. Once again three Reynolds numbers and four wall temperatures were studied. Trends for the pressure drop, heat transfer, and soot deposition are described. Then once again the wavy channel results are compared with planar channel results to illustrate the effect of geometry.

To my parents, Charles and Debra Strebel

Thank you for your love, support, and inspiration.

Acknowledgements

Although many people have helped me in various ways, I would like to thank my adviser Professor S.P. Vanka the most. The hours he spent working closely with me made it possible for me to complete this research. Next I would like to thank Mark Goodwin for all of his help in rapidly bringing me up to speed at the beginning of the research. Also I would like to thank Modine Manufacturing Company, especially Aroon K. Viswanathan, Ph.D. This study was supported financially by U.S. Army RDECOM, Ft. Belvoir, VA 22060 and Modine Manufacturing Company, Racine, WI 53403 through government contract W15P7T-08-C-P219.

Table of Contents

List of Abbreviations

BFC	Boundary Fitted Coordinates
BL	Boundary Layer
EGR	Exhaust Gas Recirculation
SOR	Successive Over-Relaxation
TDMA	Tri-diagonal Matrix Algorithm

List of Symbols

English

A	wave amplitude
c	concentration of soot particles in the fluid
c_p	specific heat of the fluid
C_c	Cunningham correction factor
d_p	soot particle diameter
D	diffusion coefficient
f	friction factor
g	gravitational constant
Gr	Grashoff number
H	Channel Height
k	turbulent kinetic energy
k_b	Boltzmann constant
K_{th}	thermophoretic coefficient
Kn	Knudsen number
L	channel length
Nu	Nusselt number
p	pressure of the fluid
P_{sys}	system pressure
Pr	Prandtl number
R_{air}	gas constant for air
Re	Reynolds number

Sc	Schmidt number
T	temperature of the fluid
u	x-component of velocity
v	y-component of velocity
x,y	Cartesian coordinates

Greek

β	volumetric thermal expansion coefficient
Γ	generic viscous term for governing equations
ε	turbulence dissipation rate
κ	thermal conductivity of the fluid
λ	mean free path
λ_{wave}	wavelength
μ	dynamic viscosity of the fluid
ξ,η	BFC coordinates
ρ	density of the fluid
τ_{wall}	wall shear stress
ω	relaxation factor

Subscripts and Superscripts

bulk	refers to the bulk fluid property at a given x location
in	refers to the channel inlet
out	refers to the channel outlet
T	turbulent
th	thermophoretic

Chapter 1

Introduction

This chapter presents an overview of the work described in this thesis. This will begin with the motivation behind the study, which is then followed by an introduction to exhaust gas recirculation (EGR) coolers and their importance, after which thermophoresis will be discussed, and will be concluded with an overview of the material presented in this thesis.

1.1 Motivation

Heat exchangers are vital components in many different types of modern machinery and their superior performance is essential. But when exhaust gas is run through a heat exchanger, such as in an EGR cooler, fouling due to soot deposition can affect the performance of the heat exchanger. The fouling can be enhanced in the presence of a temperature gradient, due to the thermophoretic force. The soot layer that develops decreases the amount of heat that can be transferred by the heat exchanger. Although fouling with thermophoresis has been studied in the past, few studies have looked at the fouling of wavy channels.

The present study compares fouling in planar and wavy channels for both laminar and turbulent flows. A computational model is employed that allows the variation of many parameters so that the effect of geometry can be studied and subsequently predicted.

1.2 EGR Coolers

With the increasingly stringent emission controls EGR coolers have become more and more important. The recirculation of exhaust gases back into the engine is a technique that decreases the amount of NO_x in the exhaust of the engine. This occurs through two different mechanisms; the reduction of the oxygen content by diluting it with exhaust gas and the reduction of the combustion temperature due to the exhaust gas which hinders NO_x production that occurs at high temperatures. But there are drawbacks to using EGR coolers, most notably the

increased fuel usage and the collection of soot particles in the cooler itself. This study looks to model the EGR coolers used in heavy duty diesel engines with the hope of using simulation to design geometries that inhibit the collection of soot.

Although many different types of heat exchangers are used throughout industry, the current study is related to those used by Modine Manufacturing Company. Below are two figures pertaining to EGR coolers. The first, figure 1.1 [1], shows an example of the heat exchanger used in an EGR system. The second, figure 1.2 [1], shows a typical EGR system, which shows how exhaust gas is taken and cooled in the EGR heat exchanger and then run back into the engine.

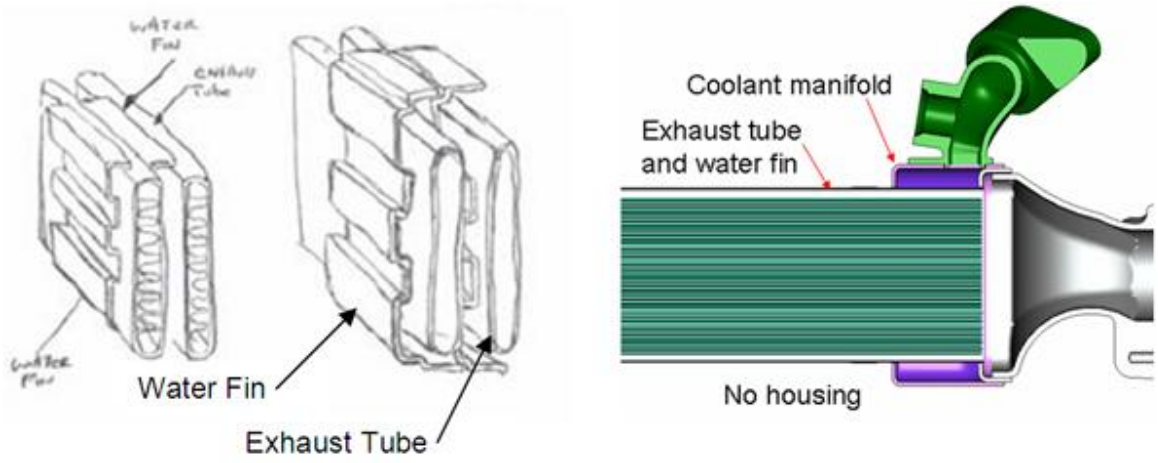

Figure 1.1: Modine EGR Cooler Example

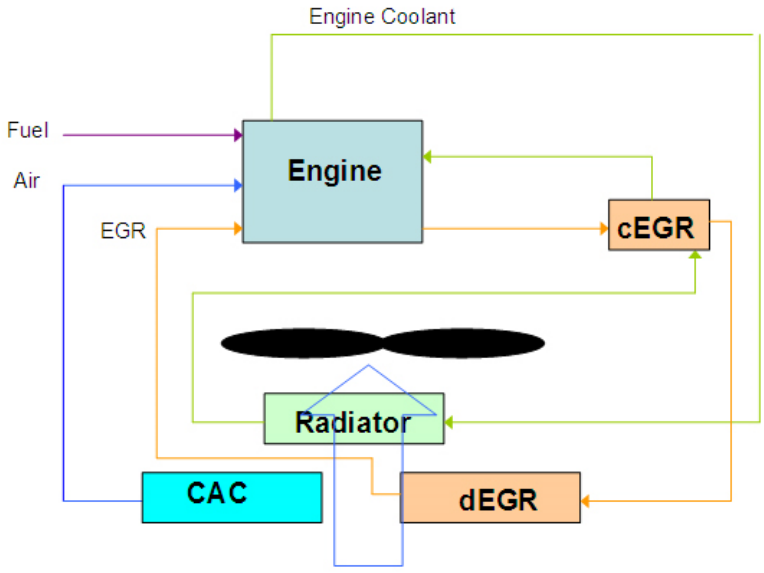

Figure 1.2: Modine EGR System Example

1.3 Thermophoresis and Fouling

The most important driving mechanism of the fouling in EGR coolers is thermophoresis. The equation describing the velocity of particles under the influence of thermophoresis is shown below.

$$V_{th} = -\frac{\mu K_{th}}{\rho T}\nabla T \tag{1.1}$$

Although the diffusion of particles to the walls will occur through other forces, such as Brownian diffusion and impaction, thermophoresis has been consistently shown to be the strongest force. Brownian diffusion is the movement of particles from areas of high concentration to areas of lower concentration and is important for nano-particles. Impaction occurs when a particle hits a wall and sticks. Thermophoresis is driven by a temperature gradient, and in an EGR cooler the temperature gradient can be quite substantial. For example the inlet gas temperature can be around 500 degrees Celsius and the wall temperatures can be as low as 150 degrees Celsius. This gives a temperature gradient in a standard 1.5 mm channel of about 300,000 °C/m.

1.4 Geometries

Many different types of geometries have been used in heat exchangers and subsequently studied numerically and experimentally. For this thesis the serpentine wavy channel is used, but a review of all types of geometries is helpful when designing new geometries to minimize the soot deposition. Below in figure 1.3 are the two types of channels studied in this thesis, planar and sinusoidal (also called serpentine). Figures 1.4 and 1.5 show other common geometries that appear in the previous literature.

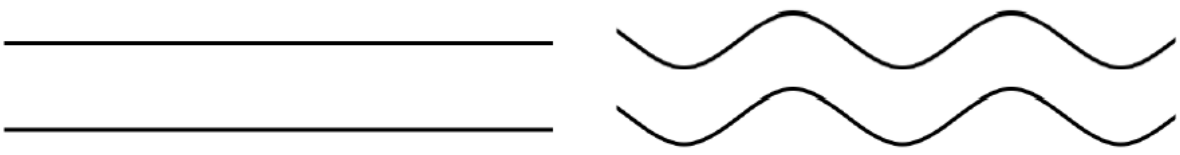

Figure 1.3: Left: Planar Channel Right: Sinusoidal (Serpentine) Channel

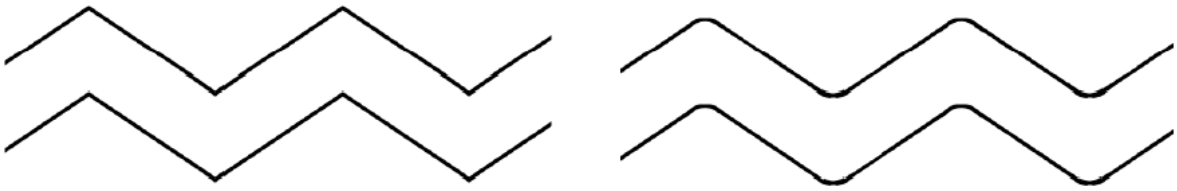

Figure 1.4: Left: Corrugated Channel Right: Corrugated Channel with rounded corners

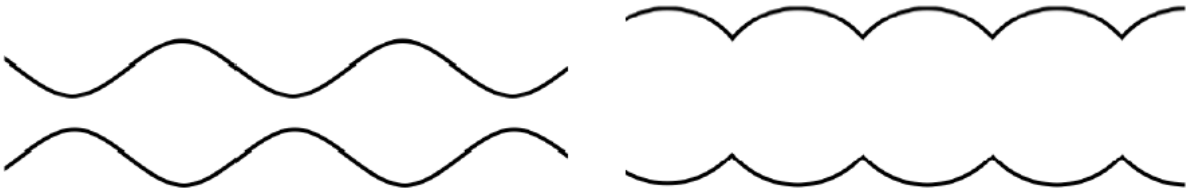

Figure 1.5: Left: Bellowed Channel Right: Arc-Shaped Bellowed Channel

1.5 Thesis Outline

The purpose of this thesis is to compare the heat transfer capabilities and fouling of planar and wavy channels. This first chapter serves to introduce the concepts of thermophoresis and fouling in a wavy channel. Chapter 2 reviews literature on both thermophoresis and flow in a wavy channel and highlights the previous work most relevant to this study. Next chapter 3 details the numerical methods used in all of the simulations presented in this study, including an overview of the BFC transformations used and details on the implicit structure of the code. The first set of results, shown in chapter 4, is for laminar flow in a wavy channel. Various Reynolds numbers and temperature gradients are studied to see the affect on heat transfer and particle deposition. Then laminar flow in a wavy channel is compared with laminar flow in a planar channel to show the increase in heat transfer, as well as the increase in fouling. In chapter 5, a similar approach is used to study turbulent flow in wavy channels. Finally chapter 6 presents the conclusions drawn from this study.

Chapter 2

Literature Review

2.1 Introduction

The relevant literature for the topic of this thesis, thermophoretic deposition of soot particles in wavy channels, can be broken up into three categories. The first section deals with the subject of thermophoresis and how this mechanism causes particles to be deposited. The second section studies the laminar flow of fluids in wavy channels with various geometries such as corrugated, arc shaped, and serpentine. The final section also looks at fluid flow in wavy channels but at high enough Reynolds numbers that turbulence occurs.

2.2 Thermophoresis

2.2.1 Theory

Schadt and Cadle [2] performed experiments to investigate thermal forces on aerosol particles of different sizes and thermal conductivities and found that the measured thermophoretic force did not agree with previously published equations. Brock [3] derived an equation, which included the appropriate boundary conditions and the convective terms of the energy equations, describing the thermophoretic force on a particle in the slip-flow regime. The equation produced results in good agreement with the results reported by Schadt and Cadle [2].

In a study by Talbot et al. [4] particles were seen to move away from a heated flat plate during laminar flow. This motion away from the flat plate was caused by thermophoresis and created a particle free area near the plate that was roughly twice the thickness of the boundary layer. After comparing the thickness of the boundary layer and the particles trajectories with

several theories, the best agreement was found with the theory proposed by Brock [3], when modified coefficients were used. The particles studied were 2 microns in diameter in a flow varying in speed from 1.2 to 4.4 m/s. The heated wall of the channel was varied from 670 to 1280 K. The modified coefficients found by the authors agreed with all of the then available data within 20%.

The results of Talbot et al. were verified in a study by Tsai et al. [5]. The authors studied thermophoresis by studying the deposition of salt particles in a tube. The particles tested ranged in size from 0.038 to 0.498 microns. The tube was 1.18 meters long and 0.43 centimeters in diameters. Both laminar and turbulent flow were studied. In the laminar flows Brownian diffusion and thermophoresis dominated, while in the turbulent flows eddy diffusion and turbulent deposition mechanisms played a role as well.

Another study by Leong [6] investigated the effect of the particle shape on both diffusiophoresis and thermophoresis. The shapes studied include cylinders, oblate spheroids, and prolate spheroids. Diffusiophoresis was shown not to depend on particle shape while thermophoresis varied substantially with different particle shapes. The strength of thermophoresis was also shown to depend on the orientation of the non-spherical particles with the temperature gradient.

Guha [7] presented a simple unified theory of particle deposition for particles of any size and matches well with experimental data. The theory includes the effects of thermophoresis, turbophoresis, electrostatic forces, gravity, lift forces, and surface roughness. This theory was developed by Reynolds averaging the full forms of the continuity and momentum conservation equations for particles. The study showed that surface roughness can have a large effect on deposition as well as thermophoresis, especially on small particles. When particles are in the intermediate size range turbophoresis begins to be just as important as thermophoresis and surface roughness.

Batchelor and Shen [8] approached the problem of particle deposition due to thermophoresis in a gas flowing over a cold surface theoretically. They attempted to show that under specific conditions the particle flux to the surface may be proportional to the heat flux through the surface, specifically when particles come from a region of uniform temperature and

concentration. This hypothesis is then tested against six sets of numerical results. Four of the results are related to cold bodies in a constant gas flow and the other two are related to flow in a circular tube in which there is a sudden drop in wall temperature. By comparing the hypothesis to the results from the six cases it was shown that it is reasonable as long as the thermophoretic coefficient is large enough.

In order to bring the work done on thermophoresis together, Bakanov [9] wrote a paper in 1995 detailing his thoughts on where research in thermophoresis should be focused. The model for small bodies is based on the assumption that the gas surrounding the body is unaffected by the presence of the body. The model for large bodies on the other hand is based on the gas slipping around the non-uniformly heated body. The current model only works for relatively small Knudsen numbers. So, Bakanov states that experiments need to be run for Knudsen numbers much less than one and much greater than one to validate the new models that have been proposed.

2.2.2 Experiments

Many experimental thermophoretic deposition results have been published, spanning various geometries and particle types. Nishio et al. [10] studied the deposition of aerosol particles in a heat exchanger pipe due to thermophoresis. Their goal was to better understand the fouling of pipes in chemical plants. The flow of a hot gas in a cold pipe was studied with varying flow rates, from laminar to turbulent. Without a temperature gradient the deposition efficiency was seen to decrease with increasing Reynolds number in the laminar region with the opposite occurring in the turbulent regime. When only diffusion was causing deposition, the rates were between 0.1% and 0.5%. When thermophoresis was included the rate got as high as 6% - 10%. As expected the deposition due to thermophoresis was shown to increase with increasing temperature gradient.

Ciro et al. [11] experimentally studied the buildup of soot and its effect on heat transfer in order to understand how containers react when surrounded by fire. The authors calculated soot deposition rates for both cooled and uncooled cylinders in fires. Both cylinders were 11.43 cm in diameter, but the cooled cylinder was 10.16 cm long and the uncooled cylinder was 30.48 cm long. A numerical analysis was performed by solving the boundary layer equations for a cylinder

and the results showed good agreement with the experimental results. Thermophoresis was found to be the dominant soot deposition mechanism. The cooled cylinder experienced more deposition as expected, which also led to a reduced heat flux. A 0.4 mm thick layer of soot was required to measure a decrease in heat flux and for a layer 1.2mm thick the heat flux was reduced by 35%.

Walker et al. [12] studied the thermophoretic deposition of particles in laminar tube flow. In their analysis the flow starts out in a tube with a uniform concentration and a temperature equal to the wall temperature. Then at some point along the tube, once the flow is fully developed, the wall temperature is decreased. The approach to finding the deposition is to look at the deposition in a very short section right after the temperature change. The majority of the flow can still be assumed to be at the initial temperature and thus only the small boundary layer must be examined. The concentration gradient becomes very large due to the thin boundary layer, so the concentration equations must be solved. Finally an equation for the deposition efficiency is derived, but it is limited to the beginning of thermal boundary layer otherwise the efficiency can go to infinity. Next they decided to find a solution that was not so limited. The energy equation was solved numerically with finite difference methods and the transport of particles was solved with particle trajectories. It was finally found that there is a limiting efficiency in laminar flow which is achieved when there is no longer a temperature gradient. They also showed that the efficiency is dependent on the thermal diffusivity of the liquid and not on the diffusion coefficient of the particles.

Montassier et al. [13] wrote a paper about the thermophoretic deposition of particles in a laminar flow with a set up very similar to Walker et al. [14] but with different particles. Again the experiment studied laminar flow through a tube with a step change in wall temperature. The particles were made of uranin with sizes 0.05, 0.1, 0.2, 0.38, 1, 4, and 8 micrometers and were in purified air. The apparatus consisted of a heated smooth walled tube with a diameter of 2 cm and a length of 90 cm and a cooled vertical tube with a diameter of 2 cm and a length of 58.6 cm. Heaters around the tube maintained them wall temperature at 373 K and a water cooling system kept the cooled tube at either 283 or 293 K. After the experiment was run the cooled deposition tube was cut into 5 cm length in order to measure the deposition. To verify the theoretical boundary conditions were met, tests were run to check for a flat radial temperature profile at the inlet of the deposition tube and check that the only cause of deposition was thermophoresis. They

found that as the flow rate was decreased the deposition was increased as expected and that the efficiency increased as the particle size decreased. From the experimental data they were able to derive empirical equations for the cumulative efficiency as a function of distance along a tube; one for small Knudsen numbers ($Kn < 2$) and the other for large Knudsen numbers ($Kn \geq 2$).

Chang et al. [14] wrote a paper about experimentally measuring the thermophoretic deposition of glass spheres in an annulus. In their experiment they used a tube that was either solid or porous and was 1.2 cm in diameter and 15 cm long. A wire was then run along the center of the tube that was electrically heated to create the necessary temperature gradient for thermophoresis. The wire is heated to between 50 and 100 degrees Celsius and the working fluid is nitrogen gas. In order to test only the thermophoretic deposition the experiment was first run without a temperature gradient to find the deposition due to other factors. The experiments were run with temperature gradients of 0, 55, and 75 degrees Celsius and the Reynolds number was 55. The particle size was also varied from 0.09 to 3 μm. The deposition efficiency was nearly 0 percent for the case with no temperature gradient and about 20 percent for both of the cases with a temperature gradient. There was also a general downward trend in efficiency as the particle size was increased.

Switching to external flow, Chiou and Cleaver [15] wrote a paper about the effects of thermophoresis on the deposition of particles in a laminar flow over a cylinder. The cylinder was held at a constant temperature and the effects of both Brownian diffusion and thermophoresis were studied. In order to solve the problem a perturbation method was used with a zeroth-order. Theoretical approximations of the wall shear stress, the heat rate, and the deposition velocities were found. Next an experiment was run to test the approximations. Temperature gradients of 50, 25, and -6 K were tested using uranin particles. Two Reynolds numbers were tested, 853 and 1673. The theoretical predictions for deposition were found to be about an order of magnitude too low, which could be caused by the surface roughness being around the same order of magnitude as the particles. As expected the amount of deposition decreased as particle size increased. If the effect of the roughness is taken into account the experimental results show a good agreement with the theoretical results.

Messerer et al. [16] studied the thermophoretic deposition of soot particles in a diesel engine, the same type of soot particles studied in this thesis. The conditions of a modern medium

duty diesel engine were replicated by a thin channel running between two plates. The top plate was heated and the bottom plate was cooled. The inlet was 4 mm and the length of the channel was 450 mm. The temperature gradient was adjusted by changing the plate separation and the temperature difference between the plates. The experiments varied the soot particle sizes from 34-300 nm, the plate separation from 0.45-1.45 mm, the temperature gradient from 10^4-10^5 K m^{-1}, and the flow velocity from 2-11 m/s. The results showed that, unlike previous studies, increasing the particle size did not decrease the thermophoretic deposition efficiency. The results also showed that the assumption that the thermophoretic coefficient is a constant 0.55 is valid for the soot produced by a diesel engine.

Finally, in a study relevant to this thesis, Lee et al. [17] experimentally studied thermophoresis with ultrafine particles in a set up made to mimic a car's exhaust pipe. A special emphasis was placed on having equal particle residence times between a real exhaust pipe and the simulation. The simulation exhaust pipe used was 0.7 cm in diameter and 1.5 meters in length. The initial temperature gradient was 250 degrees Celsius which decreased to around 77 degrees Celsius near the end of the pipe. The Reynolds number was 5800, showing turbulent flow. In further experiments the inlet gas temperature was varied from 30 to 360 degrees Celsius. As expected, the larger the temperature gradient the more particles were deposited. Particles smaller than 20 nm were found to maintain their concentration throughout the pipe. The authors propose that this could be due to the condensation of exhaust by products. Finally it was concluded that thermophoresis is the dominant mechanism for particle deposition in exhaust flow.

2.2.3 Numerical Simulations

As the current study is a numerical one, it is important to see how others have gone about numerically simulating thermophoresis. Lin and Tsai [18] wrote a paper about the efficiency of thermophoretic deposition when considering the developing flow at the inlet. The problem was analyzed numerically using the finite volume method and the SIMPLE algorithm. A grid of 12,000 was used with 200 in the axial direction and 60 in the radial direction. The tube used was 0.905 m in length and 0.0049 m. It was found that the thermophoretic efficiency is increased at the inlet by the developing flow, but the increase is found to be insignificant if the tube is sufficiently long.

Sasse et al. [19] numerically studied particle migration in concentric tube and parallel plate natural convection flows. The authors intended to create a smoke control device which, when placed over an ashtray, inhibited side-stream smoke air pollution. The two surfaces were held at constant temperatures, one hot and one cold. The flow was steady and laminar and the fluid was assumed to have constant properties. But, the density was allowed to vary in the buoyancy term of the momentum equation in order to model natural convection. Also boundary layers assumptions were made in this study. The authors used an implicit, finite-difference model that marched in space and solved each line with a tridiagonal matrix. The channel width was varied between 0.2 cm and 0.5 cm, while the height was constant at 30 cm. Temperature differences of 5 K, 10 K, 15 K and 20 K were used. Deposition was shown to be highly dependent on the channel width. Also an increase in performance was seen with larger cold wall surface areas. Finally as particle diameters increased, the efficiency of the smoke filter decreased.

Changfu and Guanghui [20] wrote a paper about a direct numerical simulation of microparticle motion while considering thermophoresis. The main purpose for studying the deposition of microparticles is to develop a way to remove them from industrial exhaust that pollutes the air. The flow was simulated using a DNS and the particle motion was tracked using a Lagrangian simulation. In the flow domain the cold wall was set at 20 degrees Celsius and the hot wall was varied. A grid of 64x128x64 was utilized with uniform elements in the x and z direction and non uniform elements in the y. They tested 1, 2.5, 10, 20 and 100 μm particles in temperature differences of 0, 130, and 180 degrees Celsius. Their results followed the expected trend, with the efficiency of the deposition decreasing as particle size increased and the efficiency increasing as the temperature gradient increased.

Iman Zahmatkesh [21] wrote a paper on the importance of Brownian diffusion and thermophoresis on the deposition of micro and nano particles. The system studied consists of a heated cylinder with a diameter of 0.25mm inside of a two dimensional duct with sections of the walls being both adiabatic and isothermal. The governing equations, consisting of the continuity, momentum and energy equations, are solved using a finite volume based computational procedure. The grid used for all calculations was 6600 cells. The boundary conditions consisted of the inlet air being at 300K with a velocity of 0.2 m/s, the heat cylinder having two temperature

zones (one at 350K and one at 400K), and the isothermal portions of the wall being held at 300K. In the end two main ideas were described. One was that for particles around 100 μm are deposited by inertial impaction. The second was that particles around 10 μm were deposited mostly by thermophoresis.

He and Ahmadi [22] wrote a paper about the thermophoretic deposition of particles in laminar and turbulent flows. They ran simulations of particle dispersion from a point source in laminar and turbulent flows with a temperature gradient. The trajectories of each particle were tracked instead of solely tracking the concentration change. The channel used was 2 cm wide by 2 m long. For the laminar case an air velocity of 1 m/s with constant density, viscosity, and thermal conductivity was used giving a Reynolds number of 1332. Particles of NaCl ranging from 0.01 to 10 μm were used. It was found that the thermophoretic force increases with increasing temperature gradient and with a fixed temperature gradient the thermophoretic force decreases as the particle size increases. It was also shown that with sufficient temperature gradient the thermophoretic force dominates both Brownian diffusion forces and gravity. The next case that was studied was the deposition under a constant concentration of particles in a laminar flow. They compared their data with previous work and found once again that thermophoretic forces increase as the temperature gradient is increased and decrease when the particle size increases. Next turbulent flow was studied using the Reynolds Stress Transport model in Fluent. A duct that was 2 cm wide by 0.4 m long with a grid of 402 x 41 was used. The inlet was set with a velocity of 5 m/s and a temperature of 150 degrees Celsius with a turbulence intensity of 5% and constant properties. They found that in a turbulent flow, particles need to be closer to the wall for the thermophoretic force to overcome the turbulent forces and deposit them. For both the point source and constant concentration cases it was found that the thermophoretic force depended on the temperature gradient and particle size, just like in the laminar cases.

Finally, Chein and Liao [23] wrote a paper about the thermophoretic effects on nano particles in channel flow. They studied the deposition in a channel that was 20 times longer than it was high. Particles of silicon oxide that were 3 nm, 5 nm, and 10 nm in size were studied in two different types of tests. The first set consisted of a fixed wall temperature with varying inlet temperatures and the second consisted of a fixed inlet temperature with varying wall temperatures. The numerical method employed by the authors was the Crank-Nicholson method.

The first and second derivatives were discretized using second order finite difference approximations and a grid size of 0.001 in the x and 0.005 in the y was used. It was found that higher deposition rates occur for the varying inlet temperature and constant wall temperature cases than in the other case. This was due to almost no deposition on the heated wall of the channel.

2.3 Particles and Condensation

In the present study the type of particles present in exhaust gases and the condensation of hydrocarbons are also important. Pratsinis and Kim [24] studied diffusion, thermophoresis and coagulation of submicron particles in a tube. The flow was laminar but non-isothermal. A model was developed by solving the general equation governing aerosol dynamics in conjunction with the heat equation for the tube geometry. The model was validated for each of the three cases, diffusion, thermophoresis, and coagulation individually with previously reported data. It was shown that thermophoresis and diffusion served as the upper and lower bounds, respectively, for deposition efficiency. Particle coagulation caused the average particle size to increase which lowered the deposition efficiency.

Neer and Koylu [25] studied the effect of operating conditions on disel gas exhaust particles. Specifically the authors investigated the effect on the aggregate size, the fractal dimensions and volume fractions. The particles in general had diameters between 20 and 35 nm and the size was shown to increase with increasing load on the engine. The authors used a transmission electron microscope visualization method that allowed for the accurate measurement of concentrations on the order of 0.001 – 0.1 ppm.

In order to simulate the fouling of an EGR cooler, Abarham et al. [26] numerically simulated the deposition of soot and condensation of hydrocarbons in a tube. The tube used was 5.54 mm in diameter and 0.3m long. The inlet temperature was 659 K and the wall temperature was 313 K. A finite difference approach was used for their 1-D model. The tube length was discretized into a 150 elements. Thermophoresis was assumed to be the only important soot deposition mechanism since the particles were too small for impaction and diffusion forces were weak. A simple model of mass condensation flux based on the partial pressure of the

hydrocarbon in the free-stream and at the wall was used to model condensation. Also the tube diameter and wall temperature were updated at each time-step as more soot deposited and hydrocarbons formed. The authors went on to compare their code with experimental data obtained by Oak Ridge National Lab. The deposition results were correct within one order of magnitude, but further investigation needs to be made to find the mechanisms causing soot removal.

Zhang and Watkinson [27] developed a mathematical model to predict the deposition of hydrocarbon formations in a tube. The boundary conditions can be either constant wall temperature of constant wall heat flux. The authors first simulated the fouling of a tube downstream of a bitumen coking reactor. The model compared well with experimental data. A second case used the model to predict the highly turbulent flow and deposition in a heat exchanger tube. Again the model predicted the condensation well. As expected both tests showed that as the vapor temperature is decreased condensation formation increases. The second experiment showed that as the fouling layer increases the wall temperature decreases and eventually a steady state solution is reached when no more hydrocarbon condensation occurs. But this would mean the heat transfer is nearly nonexistent and would be detrimental to the EGR cooler studied in this thesis.

2.4 Laminar Flow in Wavy Channels

In an early study by Nishimura et al. [28] the effects of the wall shear stresses and friction factors in a flow through a symmetric sinusoidal wavy channel were investigated both experimentally and numerically. The experimental apparatus consisted of two wavy plates, each of which had ten crests separated by a distance of 28 mm with an amplitude-to-length ratio of $2a/\lambda$ of 0.25. There was also an upstream 2000 mm long entrance region. The working fluid used was a solution of 40% glycerol and water. The experiments were performed for a range of Reynolds numbers from 40 to 10,000. The axial pressure drop was measured with taps connected to holes in the plate and the wall shear stress was measured by an electrochemical method. Electrodes were placed throughout the channel to generate hydrogen bubbles used to visualize the flow. The numerical investigation was performed using a finite element method with 1120

elements and 620 nodes. The study was performed on Reynolds numbers ranging from 1 to 700 to avoid the onset of turbulence.

In the numerical study, the recirculation vortex forms starting at around a Reynolds number of 15. The experimental study showed that the vortex becomes unsteady after a Reynolds number of about 350. For low Reynolds number the numerical results match well with the experimental results, except for some variations due to the developing unsteadiness in the flow that is not captured by the steady state numerical calculation. The friction factor was found to decrease almost linearly until a Reynolds number of 350, and then after a small peak around 350 the friction factor stays mostly constant with increasing Reynolds number. Finally it was shown that the unsteady vortex motion significantly increases the wall shear stress at the maximum cross section of the bellowed wavy channel while not affecting the wall shear stress at the minimum cross section.

In a similar study again performed by Nishimura et al. [29] the mass transfer coefficients at high Peclet numbers for flow in a bellowed channel were determined experimentally. They also found analytical solutions using both a numerical analysis and the Leveque theory. The Leveque theory works for very small Reynolds numbers where flow detachment does not occur and the numerical analysis works for higher Reynolds number flows where the Schmidt number is lower. The experimental apparatus was the same as the one used in a previous paper by Nishimura et al. [28]. Experiments were run for Reynolds numbers in the range of 100-10,000.

After running many experiments the researchers found that for laminar flow in a wavy channel the mass transfer coefficient is not appreciably larger than for a straight channel. The Sherwood number was shown to be equal to Reynolds number to the one third for laminar flow and the mass transfer length to the negative one third. Finally the largest dependence of the local Sherwood number on the Reynolds number was seen where the channel cross section was the largest.

In a third experimental investigation by Nishimura et al. [30] flow in a serpentine channel was studied in order to discover the relationship between flow structure and mass transfer. Reynolds numbers in the transitional regime were studied by measuring the local shear stress and local mass transfer rate. The experimental apparatus was a wavy channel with a channel height

of 13mm giving an aspect ratio of 15.38. The wavelength was 28mm and there were 10 waves. The flow structure was observed using hydrogen bubbles and the local wall shear stress and local mass transfer rate were measured using the electrochemical method. Finally all measurements were taken once the flow was fully developed.

The results showed that in the laminar regime there was a steady vortex in the valley of the wave with flow reversal occurring all of the time in the valley. But for flow in the turbulent regime the shear layer between the vortex and the main flow folds up and forms a transverse vortex. The vortices are disrupted from non-uniformities upstream and this causes the flow field to be three dimensional and unsteady. It was also shown the when the flow transitions from laminar to turbulent a large increase in the mass transfer rate occurs, especially around the reattachment point of flow in the recirculation vortex, implying a restart of the concentration boundary layer.

Asako et al. [31] performed a numerical study of flow in a corrugated channel with rounded corners, a geometry that was very nearly a serpentine channel. The Prandtl number was set as 0.7 and the Reynolds number was varied from 100 to 1000. The corrugation angle and aspect ratios were also varied. Four different aspect ratios were studied with three different corrugation angles; 15, 30, and 45. The flow was assumed to be periodic once fully developed so a single wave was studied and periodic boundary conditions were applied. Constant thermo-physical properties were assumed and natural convection was neglected.

The numerical method employed a coordinate transformation method as well as the SIMPLE algorithm. Finally the discretized equations were solved using a line solver. The specific Reynolds numbers solved were 100, 200, 500, 700, and 1000. The grid used was 18x34 with a grid stretching near the walls of the channel. It was shown that at a constant corrugation angle of 45 degrees the recirculation region increased in size with increasing Reynolds number. It was also shown that for a corrugated duct without rounded corners not one but two recirculation regions formed. One was in the valley and the other was on the downstream side of the crest. Also for a Reynolds number of 1000 the pressure drop in the channel with rounded corners was about 80% less than in the channel with sharp corners. The local Nusselt number was found to be greatly affected by the rounding of the corners, with the overall Nusselt number dropping by about 40% over the channel without rounded corners. But the Nusselt number is still

greater than that found with a straight channel. It is important to note that under identical pressure drop conditions the rounded corner duct has a higher Nusselt number than the duct with sharp corners. These positive effects of rounding the corners of a corrugated channel further validate the importance of serpentine channels in heat exchangers.

Oyakawa et al. [32] performed an experimental study on the effect of the channel height on the flow in a sinusoidal wavy channel. The experimental geometry consisted of a channel with wave defined by an amplitude of 20 mm, a wavelength P of 80mm, and a varied channel height H. The walls were maintained at a constant heat flux. The pressure was measured by evenly spaced static pressure taps and the wall temperature was measured with thermocouples. Flow visualization was performed with two techniques, a fluorescein dye and the oil-lampblack technique. The channel height was varied from 10mm to 60mm giving Reynolds numbers ranging from 4000 to about 200,000.

The results show that for the best performance a ratio of P/H = 2 is desirable. This was chosen because the friction achieves its best performance at a value of P/H in the range of 2.0-2.29 and the Nusselt number reaches its max at a value of P/H in the range of 1.6 – 2.0. The reattachment point of the flow appears to be independent of the channel height, but the separation point is highly dependent.

Wang and Vanka [33] performed numerical simulations for the flow through a wavy channel. The flow was considered to be two-dimensional and was solved on a curvilinear orthogonal grid using grid mapping. The equations were solved with a two step backward Euler differencing of time and Adams-Bashforth explicit differencing of the convective terms. The diffusion was solved using an implicit Crank-Nicolson scheme. For the line inversion along the ξ-direction periodic boundary conditions are used and along the η-direction Dirichlet conditions are used. The pressure Poisson equation was solved using a multi-grid technique with a Jacobi point solver and a V-cycle correction scheme. The geometry studied was from an experimental study done by Nishimura et al. [28]. A grid independence study was performed and it was shown that sufficient accuracy was obtained with a 64x32 grid but a grid of 256x128 was used. One run was done on three wavelengths to ensure periodicity and it was shown to be a valid assumption. It was shown that below a Reynolds number of 180 a steady laminar flow was observed. Above a Reynolds number of 180, a chaotic flow develops which greatly increases the heat transfer rate.

Rush et al. [34] studied the effect of wavy channels in heat exchangers, specifically looking at the development of the flow. Disturbing the air flow through fins by introducing a wavy pattern disturbs the boundary layer and makes it much thinner, allowing for a better transfer of heat. Ideally, self-sustained unsteadiness can be achieved with wavy fins to reap the mixing benefits. Experiments were run to show the flow in 12 different geometries. A closed loop water tunnel was used to visualize the flows while a wind tunnel was used to measure the heat transfer in the fins. Each test section consisted of between 12-14 waves and the test apparatus was validated with a flat channel flow test. For the heat transfer tests wires were sandwiched between two corrugated steel strips insulated heavily on one side. It is important to note that the geometries for air were close to the water flow geometries but a little off due to manufacturing difficulties. It was shown that the flow characteristics and the transitional Reynolds number both depended heavily on the phase shift between the top and bottom of the wavy channels. A phase shift of 180 degrees was shown to be the most unstable geometry, thus causing the most mixing. Also with increasing Reynolds number, the transition to mixing occurs sooner in the channel. The relative amplitude was important for low Reynolds numbers but not for high Reynolds numbers, as turbulence ensures significant mixing to counteract the amplitude effects. Finally, as in previous studies, there was a heat transfer increase at the onset of mixing therefore as the Reynolds number increased and the mixing started earlier, the heat transfer enhancement began sooner.

Stone and Vanka [35] developed a numerical simulation of a wavy channel whose geometry was identical to one of the channels in the paper by Rush et al. [11]. They looked at developing flow in a wavy channel with a phase shift of 180 degrees between the top and bottom plates, also known as a bellowed channel. Simulations were run both above and below the Hopf bifurcation value, the point at which mixing begins near the end of the channel. The domain looked at is a wavy channel consisting of 14 waves. The numerical procedure was similar to a previous study by Wang and Vanka [10], with an incompressible fluid and constant properties. The numerical integration was done with a two stage fractional step method with backward Euler differencing of the time derivative, central differencing for the diffusion terms, and an Adams-Bashforth explicit differencing of the convection terms. The numerical integration was done on a curvilinear orthogonal grid. A uniform wall temperature was used and the solution was performed on a grid of 1024x64. The time-step was taken to be 0.0025 units and the solution was

run until a steady state was achieved. It was shown that after a Reynolds number of about 300 the mixing started within the prescribed channel length. This mixing resulted in a marked increase in the heat transfer rate as well as pressure drop.

Zhang et al. [36] numerically simulated the laminar flow of air in a two dimensional serpentine channel. Periodic boundary conditions were applied along with constant temperature walls. The fluid properties were also assumed to be constant. Reynolds number varying from 10 – 1000 were tested for wall corrugation severity (γ = 2*amplitude/wavelength) in the range of 0.125 – 0.5 and fin spacing (ε = channel height/2*amplitude) in the range of 0.1 – 3.0. The domain was transformed using body-fitted coordinates and the governing equations were discretized using the finite volume method. The SIMPLE algorithm was employed to couple the pressure and the velocity. Finally the code was validated using the parallel plate geometry and found to be accurate within two percent.

The results showed that the wavy wall induces vortices in the trough regions with the size of the vortices growing with increasing Reynolds number or corrugation severity γ. The fin spacing ε also has a strong effect on the growth of vortices. When ε is less than about 0.5 the channel constricts the flow and does not allow any recirculation regions. When the fin spacing is increased to above 1.0 the flow almost always gives rise to vortices in the trough regions. The recirculation regions and core flow acceleration caused by the vortices increases the convective heat transfer but also increases the pressure drop. When vortices are formed, a significant enhancement over flat fins is shown for all values of γ. On the other hand, in the flows without vortices, a very large γ is needed in order to see any improvement over the flat fins.

Metwally and Manglik [37] studied the laminar steady flow of viscous fluids in parallel, sinusoidal shaped wavy channels. The studies occurred over Reynolds numbers from 100 to 1000 with Prandtl numbers of 5, 35, and 150. The duct walls were maintained at a constant temperature and the plate separation was twice the amplitude of the waviness of the fins. The velocity components were considered to have periodicity so only one period of the channel was considered. The standard governing equations were used and subjected to no slip, uniform wall temperature, and periodicity conditions. The equations were solved using a control volume method with finite differencing over a non-orthogonal grid. The grids used were 120x41 and 120x81 and were verified by testing grid independence. The integrals for the wall shear stress,

heat flux, and wall length were solved using the trapezoid rule. It was first shown that at a fixed Reynolds number, as the aspect ratio was increased, pockets of recirculation became more severe. Then it was shown that at a fixed aspect ratio, increasing the Reynolds number had the same effect. The wall shear stress increased drastically as the recirculation bubbles were formed and increasing aspect ratios lead to increasing losses due to friction. Importantly, the heat transfer is increased greatly as both the Reynolds number and aspect ratios are increased due to the development of the recirculation. But the authors felt it must be noted that there needs to be experimental data to verify these numerical results.

Manglik et al. [38] performed a three dimensional numerical study of air flowing in a wavy channel. The flow was laminar with Reynolds numbers between 10 and 1000 being considered. The geometry used was a sinusoidal serpentine wavy channel with the wave described by the height, fin spacing, amplitude, and wavelength. Both the constant wall temperature and the constant wall heat flux cases were considered. The solution domain was a single wave with periodic boundary conditions and a boundary fitted coordinate system. The properties were considered constant and viscous dissipation was neglected. The governing equations were discretized using the finite volume method with a uniform grid in the x-direction and grid stretching in the y and z direction. Diffusion and convection were handled by the power law scheme and the SIMPLE algorithm was used. Finally central differencing was used for the source terms. The grid was 91x41x41 and the code was validated by comparing with previous experimental results presented by Muley et al. [39].

The results show that secondary cross flow vortices form affecting the core flow of fluid through the channel. These ‘heart shaped’ counter rotating vortices slow down the flow near the center of the duct and are the strongest at the peaks and valleys of the wave. These vortices are also dependent on the Reynolds number and are shown to grow in strength as the Reynolds number is increased. Cross section of the flow showing the isotherms show how the thermal boundary layer is thinned by both the cross flow vortices and core flow acceleration. As expected this affect increased with Reynolds number and the increased heat transfer effects are evident. The effect of the fin spacing is also studied as the channel geometry is changed from a square duct to a larger aspect ratio rectangular duct. As the spacing between the fins is increased the effect of the counter rotating cross flow vortices is increased as expected. In other words for a

rectangular duct the edge effects become less important. It was also shown that increasing the fin density or decreasing the fin spacing causes the heat exchanger to become more effective per the area goodness factor. Finally the constant heat flux boundary condition has a better thermal performance than the constant wall temperature condition.

Gradeck et al. [40] performed an experimental evaluation of hydrodynamic conditions on the enhancement of heat transfer. The study focused on the local temperature distribution and the affect it has on the local flow pattern. The working fluid in the experiment was water which was run through a system with the ability to vary the temperature from 5 °C to 95 °C and the flow rate from 0 to 10^{-3} m^3s^{-1}. The test section consisted of two corrugated plates whose shapes were described by a series of alternating semi-circles, one with a radius of 2mm and the other with a radius of 10 mm, connected by straight lines. In total there were 8 waves in the entire test section with a nearly constant hydraulic diameter. One test section was made of PMMA and allows the flow to be visualized and the second was made of metal and can be heated with a heat flux of up to 62.5 W/cm^2. Nine thermocouples were used to measure the temperature and the plates were insulated to ensure no heat is lost.

The temperature profiles were found for two inlet temperatures, 27 and 60 °C, with a heating power of 56.9 kW/m^2. As expected the temperature behind the top of the corrugation, where reverse flow occurs, was higher than the temperature at the top of the corrugation. The difference was sometimes nearly 15 °C higher. The heat transfer was almost 3 times higher on the upper part of the corrugation that near the bottom. The heat transfer in the upper part of the corrugation was strongly dependant on flow characteristics while the bottom was nearly constant for different flow rates. Finally the overall heat transfer was seen to increase by a factor of two over the flat channel.

In a numerical study by Xie et al. [41] the flow through a 2-D wavy channel was investigated. The geometry used consisted of a channel 2mm high, with a wave spacing of 13mm, an amplitude of 1mm, and a flat 8mm section between each wave. The numerical solution assumed that the fluid properties were constant, the flow and heat transfer were steady state, and that the body force and dissipation forces were negligible. The grid used a curvilinear coordinate system and the discretization was done using the finite volume method and the SIMPLER algorithm. The convection terms were discretized with second order up-winding and

the diffusion terms were done using central differencing. After a grid investigation, a grid size of 80x20 was chosen.

It was found that below a Reynolds number of 300 no recirculation regions were found and that the flow characteristics were very similar to that of a planar channel. Above a Reynolds number of 300 two recirculation regions form, one at the apex of the wave and one on the leeward side of the wave. With increasing Reynolds number both of these recirculation regions increased in size. The friction factor was shown to decrease linearly with increasing Reynolds number, until a Reynolds number of about 300. In higher Reynolds number flows, the friction factor begins increasing with Reynolds number due to the recirculation regions. It was also shown that with increasing wave height, the flow transitions to turbulence at a lower Reynolds number and the Nusselt number increases. Similarly, decreasing the channel height causes the flow to transition at a lower Reynolds number.

Yoon and Kim [42] performed an experimental investigation on the heat transfer and friction behavior in sinusoidal wavy channels. They studied the flow through 29 different heat exchangers with 18 having sinusoidal fins, 9 having herringbone fins and 2 having plain fins. The fin spacing, wave amplitude, and number of tube rows were varied in order to create the variety of different heat exchangers. For the sinusoidal wave fins two set amplitudes were used, 1.5 mm and 2 mm, while all of the herringbone fins had amplitudes of 1.45 mm. The fin spacing was varied between 1.3 mm and 1.7 mm and the number of tube rows was between 1 and 3. The wavelength, tube spacing and tube diameter were nearly constant for all of the heat exchangers with slight variations between the herringbone and sinusoidal wave heat exchangers. The testing apparatus consisted of a suction wind tunnel, water circulation and control units, and a data collection system. The air inlet was held constant by maintaining the temperature and humidity of the chamber. The water temperature was held at 45 degrees Celsius and the air was held at 25 degrees Celsius with 60% relative humidity. The air flow rate was then varied from 0.75 to 2.5 m/s.

The experimental data was organized in order to show the differences between sinusoidal wave and herringbone heat exchangers. For similar amplitudes, the sinusoidal wave geometry produced higher heat transfer coefficients as well as higher friction factors than the herringbone geometry. The difference between the two appeared to increase with increasing rows of tubes.

The sinusoidal geometry seemed to shrink the recirculation regions and cause an earlier transition to turbulence. The ratio between the heat transfer and friction factor was larger for the herringbone geometry and the difference between the two geometries decreased with increasing Reynolds number. The effect of the position along the channel was weak for the sinusoidal wave geometry, implying a good heat transfer characteristic for fully developed flow. Also the effects of the amplitude and fin spacing were negligible. Finally a new correlation for predicting the j and f factors was developed, as the previous correlations over predicted the values.

Naphon [43] performed a numerical study on the heat transfer and fluid flow in a corrugated channel and validated his results by performing experiments and comparing the results. Three different geometries with constant corrugation amplitudes and various corrugation angles were tested. The corrugated plates were 130mm wide and 300mm long. The experimental tests were performed in a standard wind tunnel. Reynolds numbers in the range of 400-1600 were tested with the constant heat flux being varied from 0.5-1.2 kW/m^2. The numerical simulation of the flow was performed using the finite volume method discretized with second order upwinding and with coupling performed by the SIMPLEC algorithm. The turbulence was modeled with the standard κ-ε equations. A grid with 120,000 nodes is used and solved using the commercial software NASTRAN/CFDsign. It was shown that there is good agreement between the numerical simulation and the experimental data. As expected the corrugation increased the heat transfer due to the disruption to the thermal boundary layer. This affect is also shown to be dependent on the corrugation angle.

2.5 Turbulent Flow in Wavy Channels

In order to study the turbulent flow a turbulence model was utilized. In a paper by Radmehr and Patankar [44] the computation of turbulent boundary layer transitions by various turbulent models was studied. They started by showing the discrepancies in and the problems with the previous turbulence models. The most accurate model is the Launder Sharma model, but in general all of the models require well thought out entrance properties in order to exhibit reasonable results. The first approach was the elliptic approach, using Boussinesq's eddy-viscosity hypothesis. In order to solve the turbulent equations, a control volume methodology

was used. The grid in the y direction was always at least 40 grid points and the minimum size was 0.005. The second method was the parabolic approach which is also based on a control volume approach with Rodi and Scheuerer's proposal. A grid refinement similar to earlier is used. After comparing the models it was shown that both require a specific range of Reynolds numbers to work and even then do not do a great job of accurately predicting the behavior in the transition region.

In one of the first studies on flow in wavy channels, Goldstein and Sparrow [45] experimentally determined the heat and mass transfer characteristics of flow in a corrugated channel. Reynolds numbers studied ranged from 500-3100 to cover the laminar, transitional, and turbulent regimes. The channel used had a height of 1.65 mm, a width of 70.1 mm, and a length of 18.5 mm; with the large width helping to negate edge effects. The corrugation angle was set at 21 degrees off the horizontal. Numerous different flow phenomena were observed in the channel including secondary flows with span-wise variations, the suppression by centrifugal forces of the secondary flows, the elimination of the secondary flows due to turbulence, the possibility of having different flow regimes along the channel, and the flow separating and reattaching to the walls. An increase in the heat and mass transfer was found in laminar flow when compared to a straight channel, with an even larger increase occurring in turbulent flow. The authors concluded that the use of a corrugated channel is a viable way to increase the heat and mass transfer.

O'Brien and Sparrow [46] experimentally studied the effect of a corrugated geometry on the heat and mass transfer in a channel. For their experiment the Reynolds numbers ranged from 1,500 to 25,000 and the Prandtl number ranged from 3.8 to 8.2. The corrugation angle used in their experimental channel was 30 degrees off the horizontal. The Nusselt numbers were found by measuring the bulk temperature increase and then using the least squares method to find the slope of the temperature increase. The heat transfer coefficient was found from the Nusselt number. Comparing their experimental results to the Dittus-Boelter and Petukhov-Popov correlations the minimum heat transfer enhancement factor was 2.14 at a Reynolds number of 25,000 and a Prandtl number of 8, and the maximum was 2.71 at a Reynolds number of 10,000 and a Prandtl number of 4. Finally the friction factor was found by measuring the pressure drop, with typical values around 0.57 which is higher than for straight pipe flows. Also the pressure drop was not seen to vary greatly with Reynolds number.

In the previously mentioned study by Nishimura et al. [28] turbulent flow was experimentally studied. For turbulent flow the recirculation region was shown to increase until a Reynolds number of about 3000. Also the friction factor was shown, as expected, to be nearly constant at high Reynolds numbers. Finally the wall shear stress was shown to increase log-linearly with increasing Reynolds number in the turbulent flow regime. In another study by Nishimura et al. [29] turbulent flow was investigated. For turbulent flow the mass transfer coefficient in a wavy channel is significantly larger than in a straight channel, unlike in laminar flow where little difference is seen. Also for the turbulent regime the Sherwood number was equal to the Reynolds number to the three fifths with no dependence on the mass transfer length.

In an early numerical turbulent flow simulation by Patel et al. [47] a channel with one wavy wall is studied. The turbulence was modeled using a combination of a standard two-equation k-epsilon model for the bulk flow and a one-equation model near the wall. The momentum and turbulence equations were discretized using analytical solutions to the linearized forms of the equations. The pressure-continuity coupling was achieved using the SIMPLER algorithm. The channel used was 80H long, where H was the channel height. Two simulations were run, one with an amplitude to wavelength ratio of 0.0625 and a Reynolds number of 12,800. The grid used was 328 x 99. The second simulation had an amplitude to wavelength ratio of 0.4 and a Reynolds number of 8,160. The authors were able to get their simulation to match previous experimental data. It was shown that the wall function used is invalid as it breaks down due to the various structures seen in a wavy channel. This justifies the usage of the low Reynolds number model in our study in order to model the turbulence correctly.

Snyder et al. [48] performed an experimental study on the flow of water and air in a wavy channel. The channel consists of 15 waves all with a radius of curvature of 30mm and is defined by a channel height of 10.5mm, a wavelength of 74.2mm, and amplitude of 23.3mm. The channel also had a uniform width given by W/H about equal to 19. The air flow was visualized using smoke and the water flow was visualized using a pH sensitive dye. The upper wavy wall was heated to a uniform temperature and the lower wall was cooled to a uniform temperature. The heat transfer measurements were made at the 13^{th} wave along the centerline of the top wavy plate. Since only the top wall was outfitted with heat transfer instrumentation, some approximations had to be made to find the overall heat transfer. So the flow was assumed to be

thermally fully developed so that all of the heat that left the top wall went into the bottom wall. Reynolds numbers ranging from 250 to 10,000 were tested with the Reynolds number based on the hydraulic diameter. The temperature difference between the walls was also varied between 0 and 8 degrees centigrade.

The authors went on to compare their results with previous work done by Kays and London [49] and O'Brien and Sparrow [46]. Many different mechanisms could contribute to the increased heat transfer observed in the wavy channel. Flow separation causing recirculation and corner vortices are two mechanisms for increased heat transfer. The geometry specifically studied in this paper increased the heat transfer by interrupting the boundary layer growth while the flow separation was minimized by the channel walls to minimize the friction losses.

In another experimental study, Gschwind et al. [50] investigated Taylor Goerteler vortices in sinusoidal wavy channels. The channel is defined by constant amplitude (A) and wavelength (λ), 1.825 mm and 26 mm respectively. The channel height (H) is then varied from 1.8 to 6.4 mm to give the dimensionless parameter H/A values of 1, 1.5, 2.5, 2.9, 3.2, and 3.5. The Reynolds number based on the duct height was then varied from 50 to 10,000. Finally the duct length was limited to 400 mm.

Gcshwind et al. [50] first showed, as expected, that heat and mass transfer rates are highly dependent on the geometry and Reynolds number. It was shown that it is possible to introduce longitudinal vortices in wavy flows with instabilities. But the flow instabilities depend strongly on the channel height. Finally it was shown that flows with longitudinal vortices have a significantly lower pressure drop than turbulent flows in identical geometries.

Maaß and Schumann [51] performed a direct numerical simulation of turbulent flow in a channel with one wavy wall. The wavy wall is defined by an amplitude of 0.05 and a wavelength of 1 both in units of channel height. The Reynolds number was 6760, based on the mean velocity and mean channel height. The differential equations were solved using the finite difference method on a 256x128x96 grid with stretching near the surfaces. Periodic boundary conditions were applied at the inlet and outlet and no slip conditions were applied on the top and bottom walls. As expected a recirculation region appears. It was also shown that the effective friction velocity was 50% larger on the wavy surface than on the flat surface. The velocity and

turbulence profiles agree well with experimental data, with the one exception being the size of the recirculation region which was larger in the simulation. Importantly it was shown that the Reynolds number at low turbulence levels is much less important than the shape of the walls.

Delil et al. [52] performed a numerical simulation of turbulent flow and convective heat transfer in a wavy wall channel. The geometry used was inspired by heat exchangers that use geometric variations in the wall to break up the flow and increase the heat transfer. The study was done using RANS (Reynolds Averaged Navier Stokes equations) in conjunction with a two-equation κ-ε turbulence model. A zonal modeling strategy was employed using the 2 equation model for the bulk of the fluid with a one equation model used in the near wall region. The equations were solved using a finite volume method with a cell centered grid arrangement. The SIMPLEC algorithm was used to solve the pressure-velocity coupling. The algebraic difference equations were solved with the Strongly Implicit Procedure (SIP) and the convection fluxes are solved using the QUICK scheme. The diffusion fluxes on the other hand are solved using 2^{nd} order central differencing.

The geometry used was that of 10 waves with a flat section at both the inlet and outlet. The geometry was originally used by Patel et al. [47]. The wave spacing was H with an amplitude of 0.05H. The Reynolds number was set to match previous DNS results with a value of 6760 and the turbulence was set with an intensity of 5%. The grid used was a 421 x 100 grid with limited grid stretching. The first run was compared with a pervious study by Maaß and Schumann [51]. The velocity profiles show good agreement and the recirculation is captured, but the turbulent kinetic energy is globally underestimated. A parametric study was performed on the affect of the geometry by varying the wave amplitude from 0 to 0.1H with a step of 0.02H. The results agree with the DNS results well. The maximum turbulence zone increases its intensity and moves in the downstream direction as the amplitude is increased. Also, as predicted, the heat transfer is increased when switching from a plane channel to a wavy channel while the pressure drop also increases.

Pham et al. [53] performed a large eddy simulation of the flow and heat transfer in a serpentine channel with turbulence. The geometry is defined by three dimensionless parameters using the amplitude A, the wavelength L, fin height H, and fin spacing S; the channel spacing ratio ($\varepsilon = S/2A$), the flow cross section ($\alpha = S/H$), and the waviness aspect ratio ($\gamma = 2A/L$). The

study focuses in general on the effect of having two wavy walls forming a channel as opposed to flow over a single wavy wall and the effect of the channel spacing ratio. A low Mach number compressible formulation of the Navier-Stokes equations was used with a constant Prandtl number of 0.71 representing air. Reynolds numbers ranging from 750 to 4500 were studied in order to show flow in the transition regime. A Smagorinsky model was used for the subgrid scale viscosity. The governing equations were discretized with a second order accurate scheme on a staggered grid in Cartesian coordinates with the time marching governed by a Mac-Cormack scheme. The wavy geometry was handled using an immersed boundary method. The boundary conditions consist of a set inlet velocity and temperature profile, no slip conditions on the wavy walls, periodic boundary conditions in the span-wise direction, and a passive flow condition at the outlet. Finally a grid of 2048x320x64 was used for all calculations.

First a wavy channel with a fixed geometry defined by a channel spacing ratio of 1.0 and a waviness aspect ratio of 0.2 was used to study the growth of the vortex structure. The first observation was that the unsteadiness occurred sooner in the channel as the Reynolds number was increased. Turbulence seemed to start after a Reynolds number of roughly 1500 and would begin around the 4^{th} wave. Next the influence of the channel spacing ratio was investigated by studying 3 different values at a set Reynolds number of 3000. It was shown that with decreasing channel spacing the flow in the stream-wise direction increased. Also the addition of the top wall affected the flow by reducing the breakdown of the flow structures created along the up slope of the bottom wall. Finally the heat and mass transfer was studied by varying the channel spacing ratio. Although the heat transfer did not seem to be significantly affected by variations in the ratio the friction factor was very dependent on the ratio. This is likely because of the limitation on the friction arising from shear layers when the ratio is small.

2.6 Literature Review Summary

After reviewing the relevant literature, it was found that a lot of research has been performed on thermophoresis and flow in wavy channels. The previous research showed that thermophoresis is the dominate mechanism in particle deposition. It also showed that heat transfer and pressure drop both increase in wavy channels when compared to planar channels. But no previous study has combined wavy channels and thermophoresis, to study the deposition of soot in a heat exchanger. So the deposition of soot particles in a wavy channel due to thermophoresis will be studied in this thesis.

Chapter 3

Numerical Methods

3.1 Introduction

The purpose of this chapter is to detail the numerical methods used in this thesis. First the inclusion of variable properties is discussed, followed by the relevant assumptions and inputs. Then the structure of the BFC code is described. This includes the BFC transformation, with an example of the conversion of a standard equation into BFC coordinates. The rest of the equations are then presented in both their original and converted forms. Finally the numerical methods used to solve the elliptic governing equations are presented, including the multi-grid method used to solve the pressure correction. This section will describe both an explicit formulation as well as an implicit formulation of the code. The implicit code is faster, but the explicit code can be used to solve for unsteady flow at low Reynolds numbers.

3.2 Variable Properties

The temperature gradients used in this study are high enough that the properties of the fluid, such as density, viscosity, and thermal conductivity, can no longer be considered constant. In order to consider the variability of the fluid properties, the following equations are solved at every point in the flow at each time step. The ideal gas law was used to calculate density, with a system pressure of 250 kPa.

$$\rho = \frac{P_{sys}}{R_{air}\,T} \tag{3.1}$$

In order to determine the viscosity and thermal conductivity Sutherland's law was used. The equations were solved with μ_0 = 1.716E-5 N·s/m^2 k_0 = 0.0241 W/m·K, T_0 = 273 K, S_μ = 111 K, and S_k = 194 K.

$$\frac{\mu}{\mu_0} = \left(\frac{T}{T_0}\right)^{\frac{3}{2}} \frac{T_0 + S_\mu}{T + S_\mu} \tag{3.2}$$

$$\frac{k}{k_0} = \left(\frac{T}{T_0}\right)^{\frac{3}{2}} \frac{T_0 + S_k}{T + S_k} \tag{3.3}$$

The diffusion coefficient was determined using the Stokes-Einstein equation, where C_c is the Cunningham correction factor, k_b is the Boltzmann constant, and d_p is the particle diameter. For this study the particle diameter was held at 20 nm.

$$D = \frac{C_c k_b T}{3\pi\mu d_p} \tag{3.4}$$

3.3 Assumptions and Inputs

In the study by Talbot [4], he derives an expression that shows that for very large Knudsen numbers the thermophoretic coefficient approaches 0.55. In this study, the Knudsen number for the 20 nm particles is around 23, so the thermophoretic coefficient is taken to be a constant 0.55. Also, due to the small size of the soot particles, they do not affect the mass, momentum or scalar transport equations, allowing the soot properties to be neglected. Mixed convection was neglected because the Gr/Re^2 was sufficiently less than 1, indicating that forced convection dominates. Finally thermal radiation heat transfer was neglected since the temperatures are low enough that conduction and convection dominate.

3.4 BFC Code

3.4.1 Overview

The BFC code is meant to solve for the flow in a wavy channel where recirculation can occur, so it must solve the fully elliptic governing equations. It uses the finite-difference method and marches in time. An overview of the steps taken by the code can be seen below.

- Read input Data
- Define the geometry
- Initialize the variables
- Start the time step loop
    - Solve for the viscosity
    - Solve the x-momentum
    - Solve the y-momentum
    - Solve the pressure correction equation
    - Update the x and y velocities based on the pressure correction
    - Solve the energy equation
    - Solve the concentration equation
    - Solve the turbulent kinetic energy
    - Solve the turbulent dissipation
- End the time step loop and plot results

3.4.2 BFC Transformation

Boundary fitted coordinates were used in this code in order to allow it to solve complex geometry such as a wavy channel. The governing equations are solved on the square uniform grid defined by ξ and η coordinates and then transformed into the complex geometry defined by the standard x and y coordinates. This transformation can be seen below in Figure 3.1 [54].

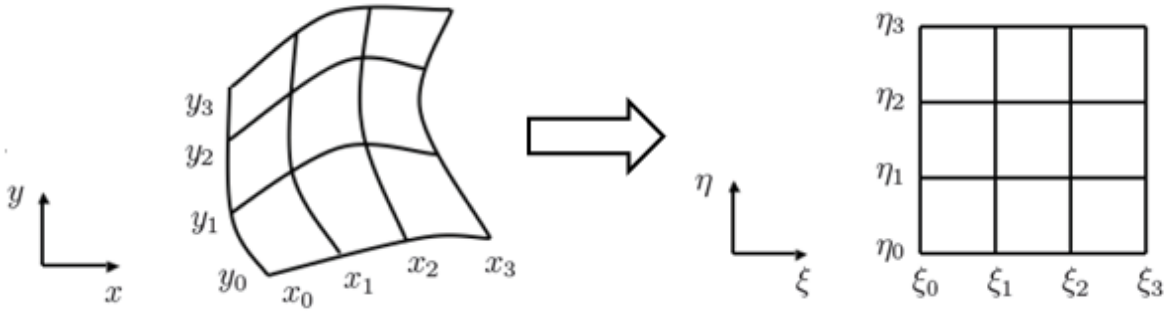

Figure 3.1: BFC coordinate transformation

3.4.3 Transforming Governing Equations

The expressions that can be used to transform equations from an (x,y) coordinate system to a (ξ,η) coordinate system are the following.

$$\frac{\partial \phi}{\partial x} = \frac{\partial \phi}{\partial \xi}\frac{\partial \xi}{\partial x} + \frac{\partial \phi}{\partial \eta}\frac{\partial \eta}{\partial x} \tag{3.5}$$

$$\frac{\partial \phi}{\partial y} = \frac{\partial \phi}{\partial \xi}\frac{\partial \xi}{\partial y} + \frac{\partial \phi}{\partial \eta}\frac{\partial \eta}{\partial y} \tag{3.6}$$

$$dx = \frac{\partial x}{\partial \xi}d\xi + \frac{\partial x}{\partial \eta}d\eta \tag{3.7}$$

$$dy = \frac{\partial y}{\partial \xi}d\xi + \frac{\partial y}{\partial \eta}d\eta \tag{3.8}$$

$$d\xi = \frac{\partial \xi}{\partial x}dx + \frac{\partial \xi}{\partial y}dy \tag{3.9}$$

$$d\eta = \frac{\partial \eta}{\partial x} dx + \frac{\partial \eta}{\partial y} dy \tag{3.10}$$

These equations can also be put into matrix form, seen below.

$$\begin{Bmatrix} dx \\ dy \end{Bmatrix} = \begin{bmatrix} \frac{\partial x}{\partial \xi} & \frac{\partial x}{\partial \eta} \\ \frac{\partial y}{\partial \xi} & \frac{\partial y}{\partial \eta} \end{bmatrix} \begin{Bmatrix} d\xi \\ d\eta \end{Bmatrix} \tag{3.11}$$

$$\begin{Bmatrix} d\xi \\ d\eta \end{Bmatrix} = \begin{bmatrix} \frac{\partial \xi}{\partial x} & \frac{\partial \xi}{\partial y} \\ \frac{\partial \eta}{\partial y} & \frac{\partial \eta}{\partial y} \end{bmatrix} \begin{Bmatrix} dx \\ dy \end{Bmatrix} \tag{3.12}$$

From these two matrices, the following relation can be found where J is the Jacobian and is also defined below.

$$\begin{bmatrix} \frac{\partial \xi}{\partial x} & \frac{\partial \xi}{\partial y} \\ \frac{\partial \eta}{\partial y} & \frac{\partial \eta}{\partial y} \end{bmatrix} = \frac{1}{J} \begin{bmatrix} \frac{\partial y}{\partial \eta} & -\frac{\partial x}{\partial \eta} \\ -\frac{\partial y}{\partial \xi} & \frac{\partial x}{\partial \xi} \end{bmatrix} \tag{3.13}$$

$$J = \frac{\partial x}{\partial \xi}\frac{\partial y}{\partial \eta} - \frac{\partial x}{\partial \eta}\frac{\partial y}{\partial \xi} \tag{3.14}$$

The continuity equation for a two dimensional, compressible flow is shown below.

$$\frac{\partial \rho}{\partial t} + \frac{\partial}{\partial x}(\rho u) + \frac{\partial}{\partial y}(\rho v) = 0 \tag{3.15}$$

Transforming into η and ξ coordinates it becomes,

$$\frac{\partial \rho}{\partial t} + \frac{\partial \xi}{\partial x}\frac{\partial}{\partial \xi}(\rho u) + \frac{\partial \eta}{\partial x}\frac{\partial}{\partial \eta}(\rho u) + \frac{\partial \xi}{\partial y}\frac{\partial}{\partial \xi}(\rho v) + \frac{\partial \eta}{\partial y}\frac{\partial}{\partial \eta}(\rho v) = 0 \tag{3.16}$$

Using the transformation matrix (3.13) above it takes the following form.

$$J\frac{\partial \rho}{\partial t} + \frac{\partial y}{\partial \eta}\frac{\partial}{\partial \xi}(\rho u) - \frac{\partial y}{\partial \xi}\frac{\partial}{\partial \eta}(\rho u) - \frac{\partial x}{\partial \eta}\frac{\partial}{\partial \xi}(\rho v) + \frac{\partial x}{\partial \xi}\frac{\partial}{\partial \eta}(\rho v) = 0 \tag{3.17}$$

Employing the product rule the following equations arise.

$$\frac{\partial y}{\partial \eta}\frac{\partial}{\partial \xi}(\rho u) = \frac{\partial}{\partial \xi}\left(\rho u \frac{\partial y}{\partial \eta}\right) - \rho u \frac{\partial^2 y}{\partial \eta \partial \xi} \tag{3.18}$$

$$\frac{\partial x}{\partial \eta}\frac{\partial}{\partial \xi}(\rho v) = \frac{\partial}{\partial \xi}\left(\rho v \frac{\partial x}{\partial \eta}\right) - \rho v \frac{\partial^2 x}{\partial \eta \partial \xi} \tag{3.19}$$

$$\frac{\partial y}{\partial \xi}\frac{\partial}{\partial \eta}(\rho u) = \frac{\partial}{\partial \eta}\left(\rho u \frac{\partial y}{\partial \xi}\right) - \rho u \frac{\partial^2 y}{\partial \eta \partial \xi} \tag{3.20}$$

$$\frac{\partial x}{\partial \xi}\frac{\partial}{\partial \eta}(\rho v) = \frac{\partial}{\partial \eta}\left(\rho v \frac{\partial x}{\partial \xi}\right) - \rho v \frac{\partial^2 x}{\partial \eta \partial \xi} \tag{3.21}$$

Substituting these back into (3.17) and canceling terms it follows,

$$J\frac{\partial \rho}{\partial t} + \frac{\partial}{\partial \xi}\left(\rho u \frac{\partial y}{\partial \eta}\right) - \frac{\partial}{\partial \xi}\left(\rho v \frac{\partial x}{\partial \eta}\right) - \frac{\partial}{\partial \eta}\left(\rho u \frac{\partial y}{\partial \xi}\right) + \frac{\partial}{\partial \eta}\left(\rho v \frac{\partial x}{\partial \xi}\right) = 0 \tag{3.22}$$

If the contravariant velocities U and V are defined as:

$$U = u\frac{\partial y}{\partial \eta} - v\frac{\partial x}{\partial \eta} \tag{3.23}$$

$$V = v\frac{\partial x}{\partial \xi} - u\frac{\partial y}{\partial \xi} \tag{3.24}$$

They can be used to simplify equation (3.22) into the following final form of the continuity.

$$J\frac{\partial \rho}{\partial t} + \frac{\partial}{\partial \xi}(\rho U) + \frac{\partial}{\partial \eta}(\rho V) = 0 \tag{3.25}$$

The original form of the x-momentum equation for a 2-D compressible flow is

$$\frac{\partial}{\partial t}(\rho u) + \frac{\partial}{\partial x}(\rho u u) + \frac{\partial}{\partial y}(\rho u v) = -\frac{\partial p}{\partial x} + \frac{\partial}{\partial x}\left(2\Gamma\frac{\partial u}{\partial x}\right) + \frac{\partial}{\partial y}\left[\Gamma\left(\frac{\partial u}{\partial y} + \frac{\partial v}{\partial x}\right)\right] \tag{3.26}$$

And for y-momentum the equation is

$$\frac{\partial}{\partial t}(\rho v) + \frac{\partial}{\partial x}(\rho v u) + \frac{\partial}{\partial y}(\rho v v) = -\frac{\partial p}{\partial y} + \frac{\partial}{\partial y}\left(2\Gamma\frac{\partial v}{\partial y}\right) + \frac{\partial}{\partial x}\left[\Gamma\left(\frac{\partial v}{\partial x} + \frac{\partial u}{\partial y}\right)\right] \tag{3.27}$$

The two momentum equations can be transformed into boundary fitted coordinates and made to fit the general conservation equation shown below.

$$\begin{aligned} J\frac{\partial}{\partial t}(\rho\phi) + \frac{\partial}{\partial \xi}(\rho U\phi) + \frac{\partial}{\partial \eta}(\rho V\phi) \\ = \frac{\partial}{\partial \xi}\left(\Gamma a_{11}\frac{\partial \phi}{\partial \xi}\right) + \frac{\partial}{\partial \eta}\left(\Gamma a_{22}\frac{\partial \phi}{\partial \eta}\right) + \frac{\partial}{\partial \xi}\left(\Gamma a_{12}\frac{\partial \phi}{\partial \eta}\right) + \frac{\partial}{\partial \eta}\left(\Gamma a_{21}\frac{\partial \phi}{\partial \xi}\right) \\ + S^{\phi}(\xi, \eta) \end{aligned} \tag{3.28}$$

Where

$$a_{11} = \frac{1}{J}\left[\left(\frac{\partial y}{\partial \eta}\right)^2 + \left(\frac{\partial x}{\partial \eta}\right)^2\right] \tag{3.29}$$

$$a_{22} = \frac{1}{J}\left[\left(\frac{\partial y}{\partial \xi}\right)^2 + \left(\frac{\partial x}{\partial \xi}\right)^2\right] \tag{3.30}$$

$$a_{12} = a_{21} = -\frac{1}{J}\left(\frac{\partial y}{\partial \xi}\frac{\partial y}{\partial \eta} + \frac{\partial x}{\partial \xi}\frac{\partial x}{\partial \eta}\right) \tag{3.31}$$

The source terms to the equation are the distinguishing factors between the equations. For x-momentum the source term is

$$\begin{aligned} S^u = & -\frac{\partial y}{\partial \eta}\frac{\partial p}{\partial \xi} + \frac{\partial y}{\partial \xi}\frac{\partial p}{\partial \eta} \\ & + \frac{\partial}{\partial \xi}\left[\frac{\Gamma}{J}\left(\left(\frac{\partial y}{\partial \eta}\right)^2 \frac{\partial u}{\partial \xi} - \frac{\partial y}{\partial \eta}\frac{\partial y}{\partial \xi}\frac{\partial u}{\partial \eta} - \frac{\partial x}{\partial \eta}\frac{\partial y}{\partial \eta}\frac{\partial v}{\partial \xi} + \frac{\partial x}{\partial \eta}\frac{\partial y}{\partial \xi}\frac{\partial v}{\partial \eta}\right)\right] \\ & + \frac{\partial}{\partial \eta}\left[\frac{\Gamma}{J}\left(\left(\frac{\partial y}{\partial \xi}\right)^2 \frac{\partial u}{\partial \eta} - \frac{\partial y}{\partial \eta}\frac{\partial y}{\partial \xi}\frac{\partial u}{\partial \xi} - \frac{\partial x}{\partial \xi}\frac{\partial y}{\partial \xi}\frac{\partial v}{\partial \eta} + \frac{\partial x}{\partial \xi}\frac{\partial y}{\partial \eta}\frac{\partial v}{\partial \xi}\right)\right] \end{aligned} \tag{3.32}$$

and for y-momentum the source term is

$$\begin{aligned} S^v = & -\frac{\partial x}{\partial \xi}\frac{\partial p}{\partial \eta} + \frac{\partial x}{\partial \eta}\frac{\partial p}{\partial \xi} \\ & + \frac{\partial}{\partial \xi}\left[\frac{\Gamma}{J}\left(\left(\frac{\partial x}{\partial \eta}\right)^2 \frac{\partial v}{\partial \xi} - \frac{\partial x}{\partial \eta}\frac{\partial x}{\partial \xi}\frac{\partial v}{\partial \eta} - \frac{\partial y}{\partial \eta}\frac{\partial x}{\partial \eta}\frac{\partial u}{\partial \xi} + \frac{\partial y}{\partial \eta}\frac{\partial x}{\partial \xi}\frac{\partial u}{\partial \eta}\right)\right] \\ & + \frac{\partial}{\partial \eta}\left[\frac{\Gamma}{J}\left(\left(\frac{\partial x}{\partial \xi}\right)^2 \frac{\partial v}{\partial \eta} - \frac{\partial x}{\partial \eta}\frac{\partial x}{\partial \xi}\frac{\partial v}{\partial \xi} - \frac{\partial y}{\partial \xi}\frac{\partial x}{\partial \xi}\frac{\partial u}{\partial \eta} + \frac{\partial y}{\partial \xi}\frac{\partial x}{\partial \eta}\frac{\partial u}{\partial \xi}\right)\right] \end{aligned} \tag{3.33}$$

The energy equation for a two dimensional flow is the following.

$$\frac{\partial}{\partial t}\left(\rho c_p T\right) + \frac{\partial}{\partial x}\left(\rho c_p u T\right) + \frac{\partial}{\partial y}\left(\rho c_p v T\right) = \frac{\partial}{\partial x}\left(\kappa \frac{\partial T}{\partial x}\right) + \frac{\partial}{\partial y}\left(\kappa \frac{\partial T}{\partial y}\right) \tag{3.34}$$

It can be modeled as the general conservation equation (3.28) with ϕ = T and S^T = 0. The concentration equation is the following.

$$\frac{\partial}{\partial t}(\rho c)+\frac{\partial}{\partial x}(\rho u c)+\frac{\partial}{\partial y}(\rho v c) = \frac{\partial}{\partial x}\left(D\frac{\partial T}{\partial x}\right)+\frac{\partial}{\partial y}\left(D\frac{\partial T}{\partial y}\right)+K_{th}\left[\frac{\partial}{\partial x}\left(\frac{\mu c}{T}\frac{\partial T}{\partial x}\right)+\frac{\partial}{\partial y}\left(\frac{\mu c}{T}\frac{\partial T}{\partial y}\right)\right] \quad (3.35)$$

It can also be modeled as the general conversation equation (3.28) with ϕ = c and the following source term.

$$S^c = K_{th}\frac{\partial}{\partial \xi}\left(\frac{\mu c}{T}a_{11}\frac{\partial T}{\partial \xi}\right)+K_{th}\frac{\partial}{\partial \eta}\left(\frac{\mu c}{T}a_{22}\frac{\partial T}{\partial \eta}\right)+K_{th}\frac{\partial}{\partial \xi}\left(\frac{\mu c}{T}a_{12}\frac{\partial T}{\partial \eta}\right)+K_{th}\frac{\partial}{\partial \eta}\left(\frac{\mu c}{T}a_{21}\frac{\partial T}{\partial \xi}\right) \quad (3.36)$$

The two-equation k-ε turbulence model used in this study is shown below.

$$\begin{aligned}\frac{\partial}{\partial t}(\rho k)+\frac{\partial}{\partial x}(\rho u k)+\frac{\partial}{\partial y}(\rho v k) &= \frac{\partial}{\partial x}\left[\left(\frac{\mu_T}{\sigma_k}+\mu\right)\frac{\partial k}{\partial x}\right]+\frac{\partial}{\partial y}\left[\left(\frac{\mu_T}{\sigma_k}+\mu\right)\frac{\partial k}{\partial y}\right]\\ &+\mu_T\left[\frac{\partial u}{\partial x}\left(2\frac{\partial u}{\partial x}\right)+\left(\frac{\partial u}{\partial y}+\frac{\partial v}{\partial x}\right)\left(\frac{\partial u}{\partial y}+\frac{\partial v}{\partial x}\right)+\frac{\partial v}{\partial y}\left(2\frac{\partial v}{\partial y}\right)\right]-2\mu\left(\frac{\partial\sqrt{k}}{\partial x}\right)^2\\ &-2\mu\left(\frac{\partial\sqrt{k}}{\partial y}\right)^2-\rho\varepsilon\end{aligned} \quad (3.37)$$

$$\begin{aligned}\frac{\partial}{\partial t}(\rho \varepsilon)+\frac{\partial}{\partial x}(\rho u \varepsilon)+\frac{\partial}{\partial y}(\rho v \varepsilon) &= \frac{\partial}{\partial x}\left[\left(\frac{\mu_T}{\sigma_\varepsilon}+\mu\right)\frac{\partial \varepsilon}{\partial x}\right]+\frac{\partial}{\partial y}\left[\left(\frac{\mu_T}{\sigma_\varepsilon}+\mu\right)\frac{\partial \varepsilon}{\partial y}\right]\\ &+C_1\frac{\varepsilon}{k}\mu_T\left[\frac{\partial u}{\partial x}\left(2\frac{\partial u}{\partial x}\right)+\left(\frac{\partial u}{\partial y}+\frac{\partial v}{\partial x}\right)\left(\frac{\partial u}{\partial y}+\frac{\partial v}{\partial x}\right)+\frac{\partial v}{\partial y}\left(2\frac{\partial v}{\partial y}\right)\right]-C_2\rho\frac{\varepsilon^2}{k}\\ &-2\frac{\mu\mu_T}{\rho}\left(\frac{\partial^2 u}{\partial x^2}+\frac{\partial^2 u}{\partial y^2}+\frac{\partial^2 u}{\partial x\partial y}+\frac{\partial^2 v}{\partial x^2}+\frac{\partial^2 v}{\partial y^2}+\frac{\partial^2 v}{\partial x\partial y}\right)\end{aligned} \quad (3.38)$$

As with the equations shown previously, the k-ε turbulence equations can be made to fit into the general conservation (3.28) with the following source terms. The first being for the k equation and the second for the ε equation.

$$
\begin{aligned}
S^k = &-J\rho\varepsilon - 2\mu\left[a_{11}\left(\frac{\partial\sqrt{k}}{\partial\xi}\right)^2 + a_{22}\left(\frac{\partial\sqrt{k}}{\partial\eta}\right)^2 + 2a_{12}\left(\frac{\partial\sqrt{k}}{\partial\xi}\right)\left(\frac{\partial\sqrt{k}}{\partial\eta}\right)\right] \\
&+ \mu_T\left[a_{11}\left(\left(\frac{\partial u}{\partial\xi}\right)^2 + \left(\frac{\partial v}{\partial\xi}\right)^2\right) + 2a_{12}\left(\frac{\partial u}{\partial\eta}\frac{\partial u}{\partial\xi} + \frac{\partial v}{\partial\eta}\frac{\partial v}{\partial\xi}\right)\right. \\
&+ a_{22}\left(\left(\frac{\partial u}{\partial\eta}\right)^2 + \left(\frac{\partial v}{\partial\eta}\right)^2\right) + \left(\frac{\partial y}{\partial\eta}\right)^2\left(\frac{\partial u}{\partial\xi}\right)^2 + \left(\frac{\partial y}{\partial\xi}\right)^2\left(\frac{\partial u}{\partial\eta}\right)^2 + \left(\frac{\partial x}{\partial\eta}\right)^2\left(\frac{\partial v}{\partial\xi}\right)^2 \\
&+ \left(\frac{\partial x}{\partial\xi}\right)^2\left(\frac{\partial v}{\partial\eta}\right)^2 - 2\frac{\partial y}{\partial\eta}\frac{\partial y}{\partial\xi}\frac{\partial u}{\partial\eta}\frac{\partial u}{\partial\xi} - 2\frac{\partial x}{\partial\eta}\frac{\partial x}{\partial\xi}\frac{\partial v}{\partial\eta}\frac{\partial v}{\partial\xi} - 2\frac{\partial x}{\partial\eta}\frac{\partial y}{\partial\eta}\frac{\partial u}{\partial\xi}\frac{\partial v}{\partial\xi} \\
&\left. - 2\frac{\partial x}{\partial\xi}\frac{\partial y}{\partial\xi}\frac{\partial u}{\partial\eta}\frac{\partial v}{\partial\eta} - 2\frac{\partial x}{\partial\xi}\frac{\partial y}{\partial\xi}\frac{\partial u}{\partial\eta}\frac{\partial v}{\partial\eta} + 2\frac{\partial x}{\partial\eta}\frac{\partial y}{\partial\xi}\frac{\partial u}{\partial\xi}\frac{\partial v}{\partial\eta} + 2\frac{\partial x}{\partial\xi}\frac{\partial y}{\partial\eta}\frac{\partial u}{\partial\eta}\frac{\partial v}{\partial\xi}\right]
\end{aligned}
\tag{3.39}
$$

$$
\begin{aligned}
S^{\varepsilon} = & -C_2 J\rho\frac{\varepsilon^2}{k} \\
& + C_1\frac{\varepsilon}{k}\mu_T\left[a_{11}\left(\left(\frac{\partial u}{\partial\xi}\right)^2+\left(\frac{\partial v}{\partial\xi}\right)^2\right)+2a_{12}\left(\frac{\partial u}{\partial\eta}\frac{\partial u}{\partial\xi}+\frac{\partial v}{\partial\eta}\frac{\partial v}{\partial\xi}\right)\right. \\
& + a_{22}\left(\left(\frac{\partial u}{\partial\eta}\right)^2+\left(\frac{\partial v}{\partial\eta}\right)^2\right)+\left(\frac{\partial y}{\partial\eta}\right)^2\left(\frac{\partial u}{\partial\xi}\right)^2+\left(\frac{\partial y}{\partial\xi}\right)^2\left(\frac{\partial u}{\partial\eta}\right)^2+\left(\frac{\partial x}{\partial\eta}\right)^2\left(\frac{\partial v}{\partial\xi}\right)^2 \\
& + \left(\frac{\partial x}{\partial\xi}\right)^2\left(\frac{\partial v}{\partial\eta}\right)^2-2\frac{\partial y}{\partial\eta}\frac{\partial y}{\partial\xi}\frac{\partial u}{\partial\eta}\frac{\partial u}{\partial\xi}-2\frac{\partial x}{\partial\eta}\frac{\partial x}{\partial\xi}\frac{\partial v}{\partial\eta}\frac{\partial v}{\partial\xi}-2\frac{\partial x}{\partial\eta}\frac{\partial y}{\partial\eta}\frac{\partial u}{\partial\xi}\frac{\partial v}{\partial\xi} \\
& \left. - 2\frac{\partial x}{\partial\xi}\frac{\partial y}{\partial\xi}\frac{\partial u}{\partial\eta}\frac{\partial v}{\partial\eta}-2\frac{\partial x}{\partial\xi}\frac{\partial y}{\partial\xi}\frac{\partial u}{\partial\eta}\frac{\partial v}{\partial\eta}+2\frac{\partial x}{\partial\eta}\frac{\partial y}{\partial\xi}\frac{\partial u}{\partial\xi}\frac{\partial v}{\partial\eta}+2\frac{\partial x}{\partial\xi}\frac{\partial y}{\partial\eta}\frac{\partial u}{\partial\eta}\frac{\partial v}{\partial\xi}\right] \\
& - 2\frac{\mu\mu_T}{\rho}\left[\frac{\partial}{\partial\xi}\left(\left(a_{11}-\frac{2}{J}\frac{\partial x}{\partial\eta}\frac{\partial y}{\partial\eta}\right)\left(\frac{\partial u}{\partial\xi}+\frac{\partial v}{\partial\xi}\right)\right)\right. \\
& + \frac{\partial}{\partial\eta}\left(\left(a_{22}-\frac{2}{J}\frac{\partial x}{\partial\xi}\frac{\partial y}{\partial\xi}\right)\left(\frac{\partial u}{\partial\eta}+\frac{\partial v}{\partial\eta}\right)\right)+\frac{\partial}{\partial\xi}\left(\left(a_{12}+\frac{2}{J}\frac{\partial x}{\partial\xi}\frac{\partial y}{\partial\eta}\right)\left(\frac{\partial u}{\partial\eta}+\frac{\partial v}{\partial\eta}\right)\right) \\
& \left. + \frac{\partial}{\partial\eta}\left(\left(a_{21}+\frac{2}{J}\frac{\partial x}{\partial\eta}\frac{\partial y}{\partial\xi}\right)\left(\frac{\partial u}{\partial\xi}+\frac{\partial v}{\partial\xi}\right)\right)\right]
\end{aligned}
\tag{3.40}
$$

3.4.4 Solution Methods

The geometry of the wavy channel is defined by the wavy length, the channel height and the wave amplitude. The geometric derivatives used in the BFC forms of the governing equations were solved using central differencing throughout the interior of the domain and one sided differencing along the boundaries.

3.4.4.1 Implicit Code

In the implicit version of the code each equation was solved implicitly using the SOR method by summing the variables, which are multiplied by coefficients, around the point being solved. The source term is then added to this sum and the resulting equation can be used to solve for the desired variable ϕ. This process can be written into equation form and is shown below.

$$A_P\phi_{i,j} = \omega\big[A_W\phi_{i-1,j} + A_E\phi_{i+1,j} + A_N\phi_{i,j+1} + A_S\phi_{i,j-1} + A_{NW}\phi_{i-1,j+1} + A_{NE}\phi_{i+1,j+1} + A_{SW}\phi_{i-1,j-1} + A_{SE}\phi_{i+1,j-1} + S^{\phi}\big] + (1-\omega)A_p\phi_{i,j} \tag{3.41}$$

The value $\phi_{i,j}$ on the right hand side of the equation is the old value which gets over written when the equation is solved. The value of ω is the relaxation factor and if it is equal to one the equation reduces to the Gauss-Seidel method. The extra directions, northwest, southwest, northeast, and southeast are used because of the mixed derivatives present in the BFC forms of the governing equations. Due to the equations being solved implicitly, the coefficients include both the diffusion terms as well as the convection terms. The equations for each coefficient can be seen below. These coefficients apply to every equation with the exception of the pressure correction.

$$A_N = \frac{(\Gamma a_{22})_{i,j} + (\Gamma a_{22})_{i,j+1}}{2} + \frac{(\Gamma a_{12})_{i+1,j} - (\Gamma a_{12})_{i-1,j}}{8} - V_{i,j} \tag{3.42}$$

$$A_S = \frac{(\Gamma a_{22})_{i,j} + (\Gamma a_{22})_{i,j-1}}{2} - \frac{(\Gamma a_{12})_{i+1,j} - (\Gamma a_{12})_{i-1,j}}{8} + V_{i,j-1} \tag{3.43}$$

$$A_W = \frac{(\Gamma a_{11})_{i,j} + (\Gamma a_{11})_{i-1,j}}{2} + \frac{(\Gamma a_{12})_{i,j-1} - (\Gamma a_{12})_{i,j+1}}{8} + U_{i-1,j} \tag{3.44}$$

$$A_E = \frac{(\Gamma a_{11})_{i,j} + (\Gamma a_{11})_{i+1,j}}{2} - \frac{(\Gamma a_{12})_{i,j-1} - (\Gamma a_{12})_{i,j+1}}{8} - U_{i,j} \tag{3.45}$$

$$A_{NW} = -\frac{(\Gamma a_{12})_{i,j+1} + 2(\Gamma a_{12})_{i,j} + (\Gamma a_{12})_{i-1,j}}{8} \tag{3.46}$$

$$A_{NE} = \frac{(\Gamma a_{12})_{i,j+1} + 2(\Gamma a_{12})_{i,j} + (\Gamma a_{12})_{i+1,j}}{8} \tag{3.47}$$

$$A_{SW} = \frac{(\Gamma a_{12})_{i,j-1} + 2(\Gamma a_{12})_{i,j} + (\Gamma a_{12})_{i-1,j}}{8} \tag{3.48}$$

$$A_{SE} = -\frac{(\Gamma a_{12})_{i,j-1} + 2(\Gamma a_{12})_{i,j} + (\Gamma a_{12})_{i+1,j}}{8} \tag{3.49}$$

The U's and V's are the contravariant velocities and they appear due to the upwinding of the convection terms. If the contravariant velocities are greater than zero they get added to A_S and A_W and if they are negative they get subtracted from A_N and A_E. For the nodes adjacent to the inlet, A_W is zero and similarly for the nodes adjacent to the outlet A_E is zero. The A_P coefficient is equal to the sum of all the other coefficients as well as the time derivative term from the left hand side of each governing equation. For the turbulence equations for k and epsilon, A_P includes $J\rho\varepsilon/k$ and $C_2\rho\varepsilon^2/k$, respectively.

The pressure correction equation has different coefficients due to the implicit coupling of the momentum and continuity equations. The pressure coefficients pick up a dependence on the A_P coefficient from the momentum equations. The coefficients can be seen below, where A_{PM} is the A_P from the momentum equations. As before the A_P for pressure is merely the sum of all of the other coefficients.

$$A_N = (A_{Pm})_{i,j+\frac{1}{2}} \frac{(Ja_{22})_{i,j} + (Ja_{22})_{i,j+1}}{2} + (A_{Pm})_{i+\frac{1}{2},j} \frac{(Ja_{12})_{i,j} + (Ja_{12})_{i+1,j}}{4} - (A_{Pm})_{i-\frac{1}{2},j} \frac{(Ja_{12})_{i,j} + (Ja_{12})_{i-1,j}}{4} \tag{3.50}$$

$$A_S = (A_{Pm})_{i,j-\frac{1}{2}} \frac{(Ja_{22})_{i,j} + (Ja_{22})_{i,j-1}}{2} - (A_{Pm})_{i+\frac{1}{2},j} \frac{(Ja_{12})_{i,j} + (Ja_{12})_{i+1,j}}{4} + (A_{Pm})_{i-\frac{1}{2},j} \frac{(Ja_{12})_{i,j} + (Ja_{12})_{i-1,j}}{4} \tag{3.51}$$

$$A_W = (A_{Pm})_{i-\frac{1}{2},j}\frac{(\mathrm{Ja}_{11})_{i,j} + (\mathrm{Ja}_{11})_{i-1,j}}{2} - (A_{Pm})_{i,j+\frac{1}{2}}\frac{(\mathrm{Ja}_{12})_{i,j} + (\mathrm{Ja}_{12})_{i,j+1}}{4} + (A_{Pm})_{i,j-\frac{1}{2}}\frac{(\mathrm{Ja}_{12})_{i,j} + (\mathrm{Ja}_{12})_{i,j-1}}{4} \quad (3.52)$$

$$A_E = (A_{Pm})_{i+\frac{1}{2},j}\frac{(\mathrm{Ja}_{11})_{i,j} + (\mathrm{Ja}_{11})_{i+1,j}}{2} + (A_{Pm})_{i,j+\frac{1}{2}}\frac{(\mathrm{Ja}_{12})_{i,j} + (\mathrm{Ja}_{12})_{i,j+1}}{4} - (A_{Pm})_{i,j-\frac{1}{2}}\frac{(\mathrm{Ja}_{12})_{i,j} + (\mathrm{Ja}_{12})_{i,j-1}}{4} \quad (3.53)$$

$$A_{NW} = -(A_{Pm})_{i-\frac{1}{2},j}\frac{(\mathrm{Ja}_{12})_{i,j} + (\mathrm{Ja}_{12})_{i-1,j}}{4} - (A_{Pm})_{i,j+\frac{1}{2}}\frac{(\mathrm{Ja}_{12})_{i,j} + (\mathrm{Ja}_{12})_{i,j+1}}{4} \quad (3.54)$$

$$A_{NE} = (A_{Pm})_{i+\frac{1}{2},j}\frac{(\mathrm{Ja}_{12})_{i,j} + (\mathrm{Ja}_{12})_{i+1,j}}{4} + (A_{Pm})_{i,j+\frac{1}{2}}\frac{(\mathrm{Ja}_{12})_{i,j} + (\mathrm{Ja}_{12})_{i,j+1}}{4} \quad (3.55)$$

$$A_{SW} = (A_{Pm})_{i-\frac{1}{2},j}\frac{(\mathrm{Ja}_{12})_{i,j} + (\mathrm{Ja}_{12})_{i-1,j}}{4} + (A_{Pm})_{i,j-\frac{1}{2}}\frac{(\mathrm{Ja}_{12})_{i,j} + (\mathrm{Ja}_{12})_{i,j-1}}{4} \quad (3.56)$$

$$A_{SE} = -(A_{Pm})_{i+\frac{1}{2},j}\frac{(\mathrm{Ja}_{12})_{i,j} + (\mathrm{Ja}_{12})_{i+1,j}}{4} - (A_{Pm})_{i,j-\frac{1}{2}}\frac{(\mathrm{Ja}_{12})_{i,j} + (\mathrm{Ja}_{12})_{i,j-1}}{4} \quad (3.57)$$

The pressure is solved using a multi-grid solver which restricts and solves the pressure residuals onto successively coarser grids and then prolongates the pressure residuals onto successively finer grids following a standard v-cycle. In other words, if the original grid is 64x64, the pressure is first solved on the finest grid then restricted onto a 32x32 grid and solved again. This is repeated until the grid can no longer be coarsened further and then the residuals of the coarse grids are used to update the finer and finer grids until the original fine grid is solved again. The use of multi-grid allows the pressure correction to be solved faster and more accurately. All of the equations use a line solver and relaxation factors are applied to momentum,

pressure, density, energy, turbulent kinetic energy, turbulent dissipation, and turbulent viscosity. The properties are updated at the end of each time step, causing the properties to be lagged temporally.

3.4.4.2 Explicit Code

The explicit version of the code uses all of the same equations as the implicit version and solves them using the SOR method as well. But the convection terms are no longer in the coefficients and are instead in the source term. Also the pressure coefficients are identical to the coefficients for all of the other equations. So the coefficients simplify to the following equations shown below. All of the equations are then solved using a line solver with the exception of the momentum equations which are solved using a point solver.

$$A_N = \frac{(\Gamma a_{22})_{i,j} + (\Gamma a_{22})_{i,j+1}}{2} + \frac{(\Gamma a_{12})_{i+1,j} - (\Gamma a_{12})_{i-1,j}}{8} \tag{3.58}$$

$$A_S = \frac{(\Gamma a_{22})_{i,j} + (\Gamma a_{22})_{i,j-1}}{2} - \frac{(\Gamma a_{12})_{i+1,j} - (\Gamma a_{12})_{i-1,j}}{8} \tag{3.59}$$

$$A_W = \frac{(\Gamma a_{11})_{i,j} + (\Gamma a_{11})_{i-1,j}}{2} + \frac{(\Gamma a_{12})_{i,j-1} - (\Gamma a_{12})_{i,j+1}}{8} \tag{3.60}$$

$$A_E = \frac{(\Gamma a_{11})_{i,j} + (\Gamma a_{11})_{i+1,j}}{2} - \frac{(\Gamma a_{12})_{i,j-1} - (\Gamma a_{12})_{i,j+1}}{8} \tag{3.61}$$

$$A_{NW} = -\frac{(\Gamma a_{12})_{i,j+1} + 2(\Gamma a_{12})_{i,j} + (\Gamma a_{12})_{i-1,j}}{8} \tag{3.62}$$

$$A_{NE} = \frac{(\Gamma a_{12})_{i,j+1} + 2(\Gamma a_{12})_{i,j} + (\Gamma a_{12})_{i+1,j}}{8} \tag{3.63}$$

$$A_{SW} = \frac{(\Gamma a_{12})_{i,j-1} + 2(\Gamma a_{12})_{i,j} + (\Gamma a_{12})_{i-1,j}}{8} \tag{3.64}$$

$$A_{SE} = -\frac{(\Gamma a_{12})_{i,j-1} + 2(\Gamma a_{12})_{i,j} + (\Gamma a_{12})_{i+1,j}}{8} \tag{3.65}$$

3.5 Numerical Methods Summary

This chapter described the code used for this present study. A fully elliptic finite difference code is used with boundary fitted coordinates. Variable properties are considered and the equations are solved with by an SOR method. Also a low Reynolds number k-ε model was used for turbulence. Two formulations were developed, with the explicit formulation being able to solve unsteady flows and the implicit formulation being able to solve for steady-state solutions faster. These two codes will be used in the next two chapters to solve for laminar and turbulent flow in wavy and planar channels.

Chapter 4

Laminar Study

4.1 Introduction

This chapter presents the results on heat transfer, pressure drop, and soot deposition for laminar flow in a wavy channel. Various Reynolds numbers and temperature gradients are tested and the effects described. This chapter will begin by describing the runs performed and geometry used. Then the results for wavy channels will be discussed, specifically looking at the effect on heat transfer, pressure drop, and soot deposition. Finally the wavy channel will be compared with a planar channel in order to show the effect of geometry.

4.2 Wavy Channel Study

The list of runs completed can be seen below in table 4.1. Three different Reynolds numbers were used, 300, 400, and 1000. For each Reynolds number 4 different wall temperatures were used; 300 K, 400 K, 500 K, and 750 K. It was found that the laminar flow becomes unsteady at high temperature gradients for a Reynolds number of 400 and for all non-isothermal cases at a Reynolds number of 500. Figure 4.1 below shows the momentum residual for a run with a Reynolds number of 400 and a wall temperature 300 K. It shows how the unsteadiness causes the implicit code's solution to become unstable and fail. So in order to study non-isothermal flow in a wavy channel at a high laminar Reynolds number, the explicit formulation of the code was used. The code used for each run can also be seen below in table 4.1

Table 4.1: Matrix of laminar wavy channel simulations

Reynolds Number	Inlet Temperature [K]	Wall Temperature [K]	Code
Laminar Runs			
300	750	750	Implicit
300	750	500	Implicit
300	750	400	Implicit
300	750	300	Implicit
400	750	750	Implicit
400	750	500	Implicit
400	750	400	Implicit
400	750	300	Implicit
1000	750	750	Explicit
1000	750	500	Explicit
1000	750	400	Explicit
1000	750	300	Explicit

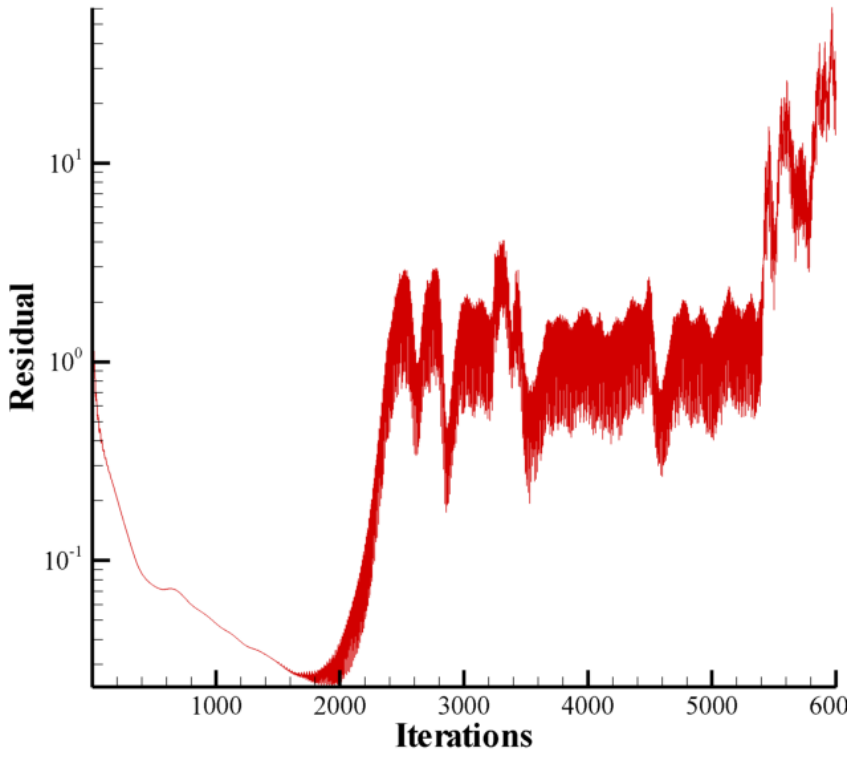

Figure 4.1: Unsteady momentum residual, Re = 400 T_{wall} = 300 K

4.2.1 Geometry and Boundary Conditions

A single sinusoidal wavy geometry is used for both the laminar study in this chapter as well as the turbulence study in chapter 5. The seven wave geometry can be seen below in figure 4.2, where A is the amplitude, H is the channel height, L is the channel length, and λ_{wave} is the wave length. A grid with 65 nodes in the cross stream direction and 2049 nodes in the stream-wise direction is used. Also for extra near-wall refinement, grid stretching of 2 percent is used in the cross stream direction.

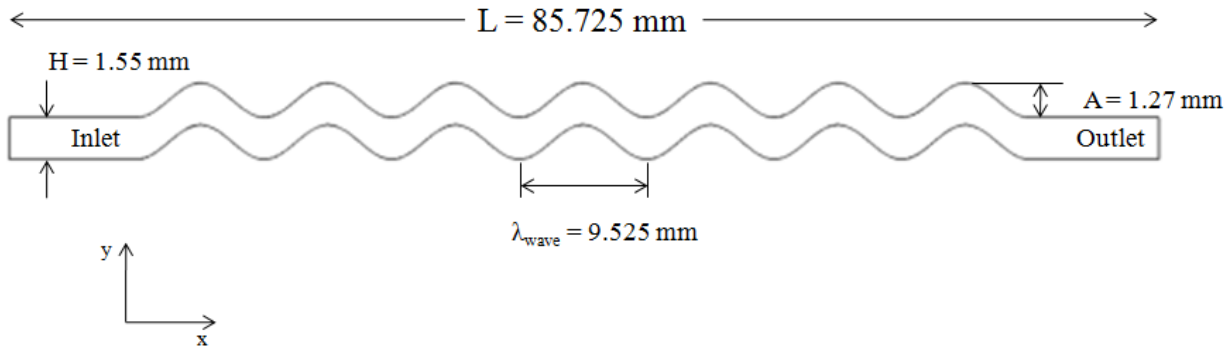

Figure 4.2: Wavy channel geometry

At the inlet a uniform velocity profile is prescribed and the fluid temperature is set to a constant 750 K. The walls use a no-slip condition and a temperature is prescribed specific to each run. A zero derivative condition is then used for all variables at the outlet. The pressure solver also uses a zero derivative condition at the walls.

4.2.2 Flow Field

Figures 4.3 and 4.4 show the u-velocity contours for the inlet and outlet respectively. The contour is for a Reynolds number of 400 and a wall temperature of 400 K. A low velocity recirculation region can be seen at the top and bottom of each wave. These regions become larger further down the channel as the fluid cools and slows down. This slowing due to cooling is apparent when the inlet and outlet velocities are compared. The total temperature change can be seen in figures 4.5 and 4.6, which display the temperature profiles at the inlet and outlet respectively. Significant cooling is seen near the inlet, but near the end of the channel the fluid is not cooling as quickly. Also it is seen that although the channel is relatively long the fluid has not cooled all the way to the wall temperature. Concentration contour plots can be seen in figures

4.7 and 4.8, which shown the inlet and outlet respectively. Higher levels concentrations of soot are shown at the top and bottom of each wave, where the soot particles get trapped in the recirculation regions. This capture of the particles allows for higher soot deposition in wavy channels when compares to straight channels which lack this effect.

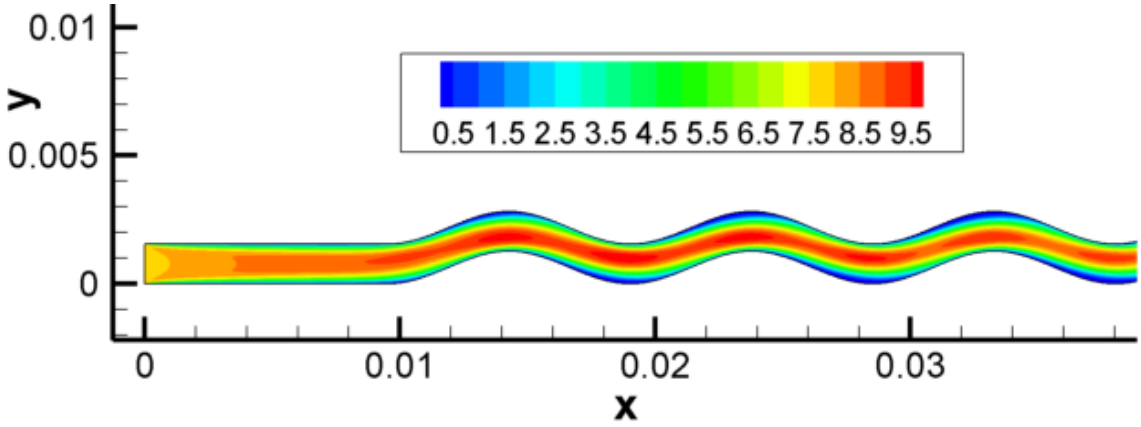

Figure 4.3: Contour of u-velocity at the inlet, Re = 400 and T_{wall} = 400

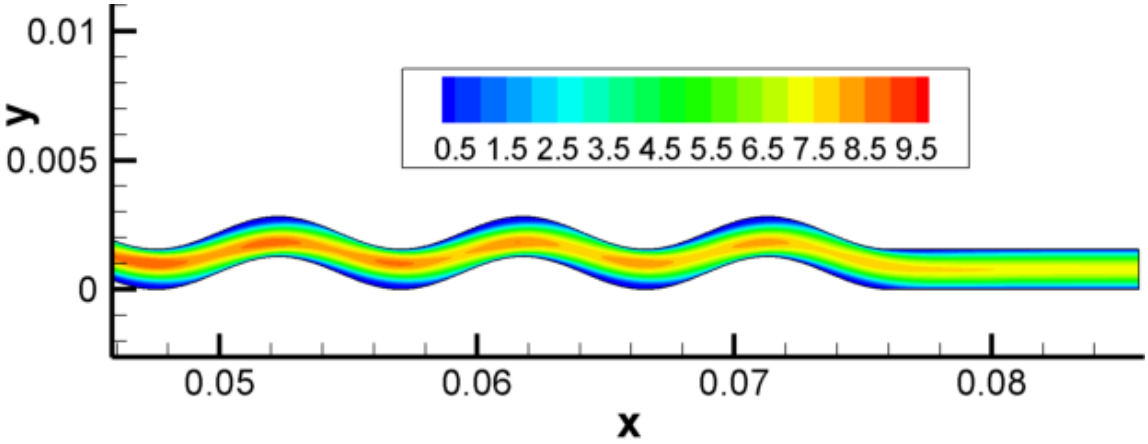

Figure 4.4: Contour of u-velocity at the outlet, Re = 400 and T_{wall} = 400

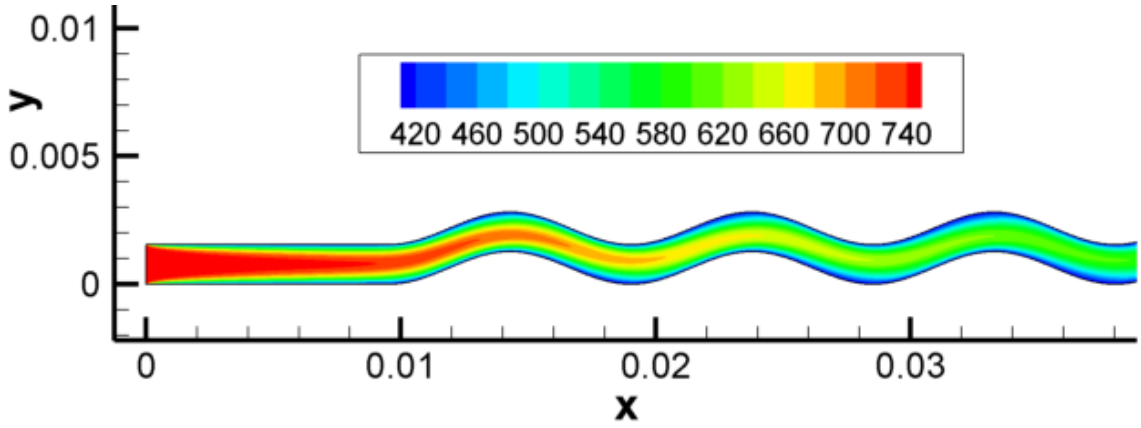

Figure 4.5: Contour of temperature at the inlet, Re = 400 and T_{wall} = 400

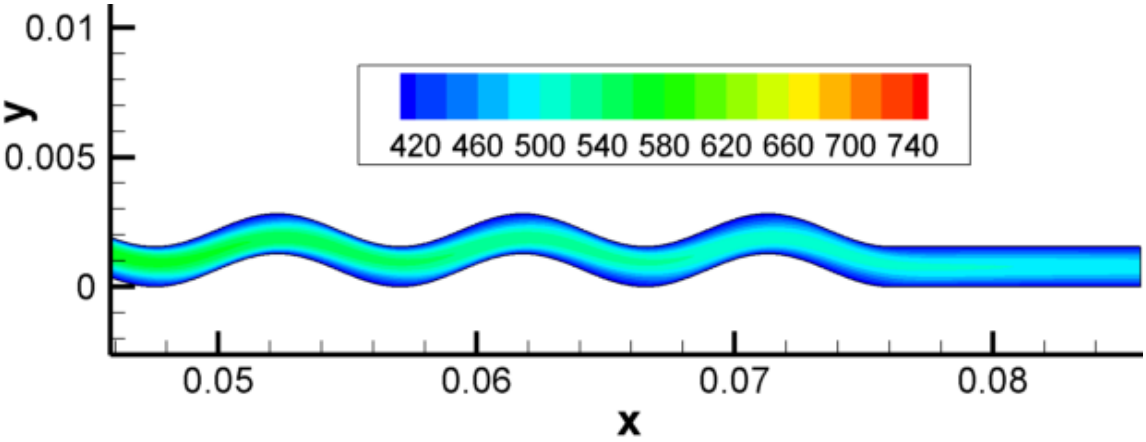

Figure 4.6: Contour of temperature at the outlet, Re = 400 and T_{wall} = 400

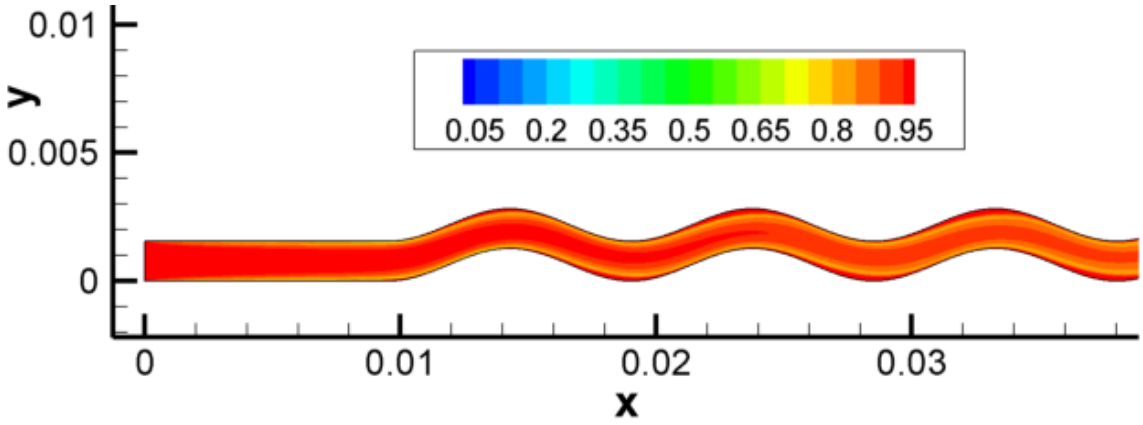

Figure 4.7: Contour of concentration at the inlet, Re = 400 and T_{wall} = 400

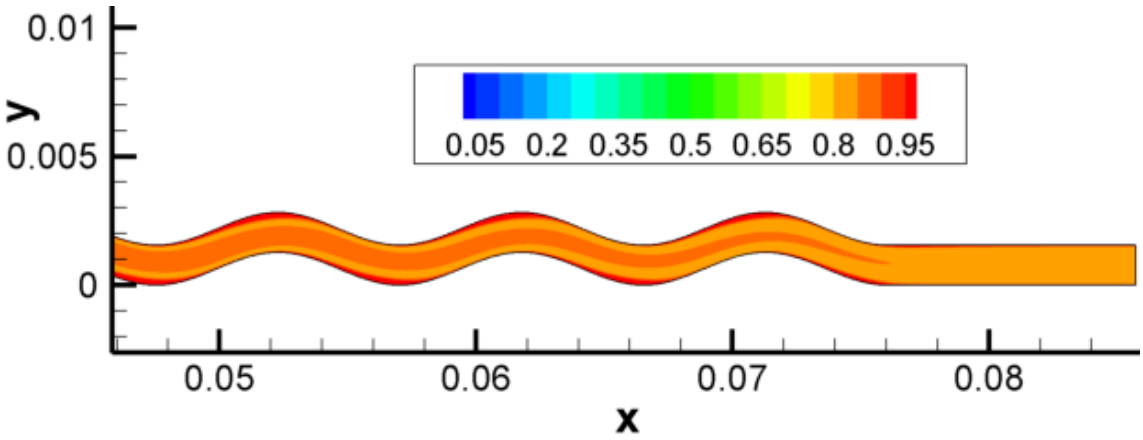

Figure 4.8: Contour of concentration at the outlet, Re = 400 and T_{wall} = 400

4.2.3 Pressure Drop

Figures 4.9, 4.10, 4.11, and 4.12 show the predicted values for f*Re at different Reynolds numbers for wall temperature of 300 K, 400 K, 500 K, and 750 K respectively. The plots show oscillations which are caused by the wavy geometry. The first wave starts at an x/H of about 6, which the figures show with a sharp increase in the f*Re. The sharp increase occurs when the flow is required to change direction. So the first peak corresponds to the first time the flow turns the corner to go up and the first minimum occurs after the fluid has changed direction and is simply going straight up the wave. At the top of the first wave the fluid must change direction again so another peak occurs. Since each wave causes the flow to change direction twice, two maxima and two minima correspond to each wave. The maxima and minima of f*Re for Reynolds numbers of 300 and 400 stay relatively constant throughout the channel, but for a Reynolds number of 1000 the maxima get larger and minima get smaller as the fluid goes down the channel. This is due to the unsteadiness of the flow at a Reynolds number of 1000. Consequently the values of f*Re are much larger for the Reynolds number of 1000.

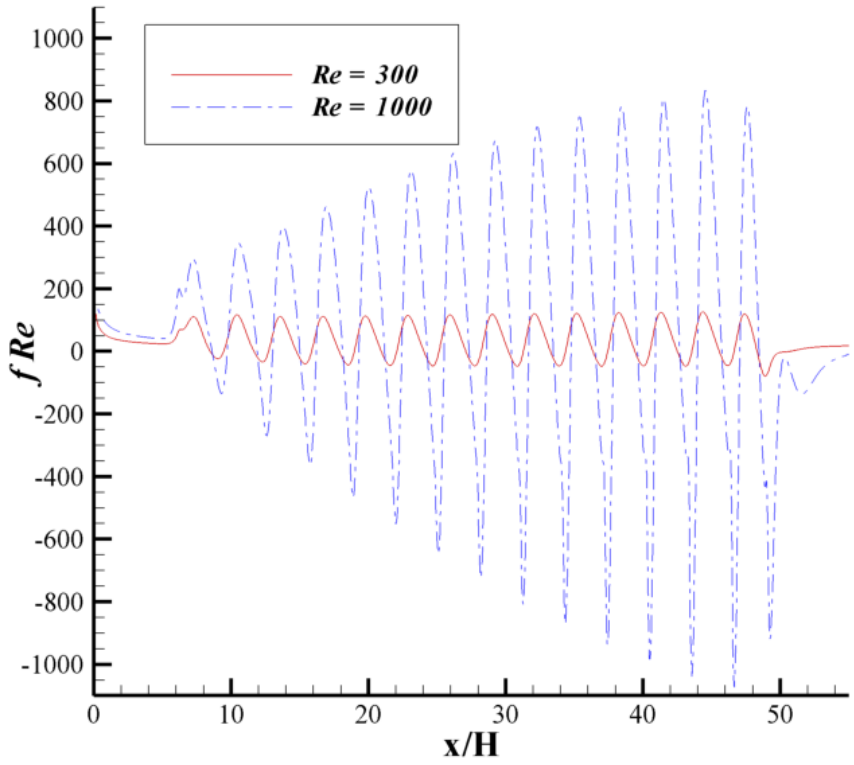

Figure 4.9: *f Re* for laminar flow in a wavy channel, T_{wall} = 300 K

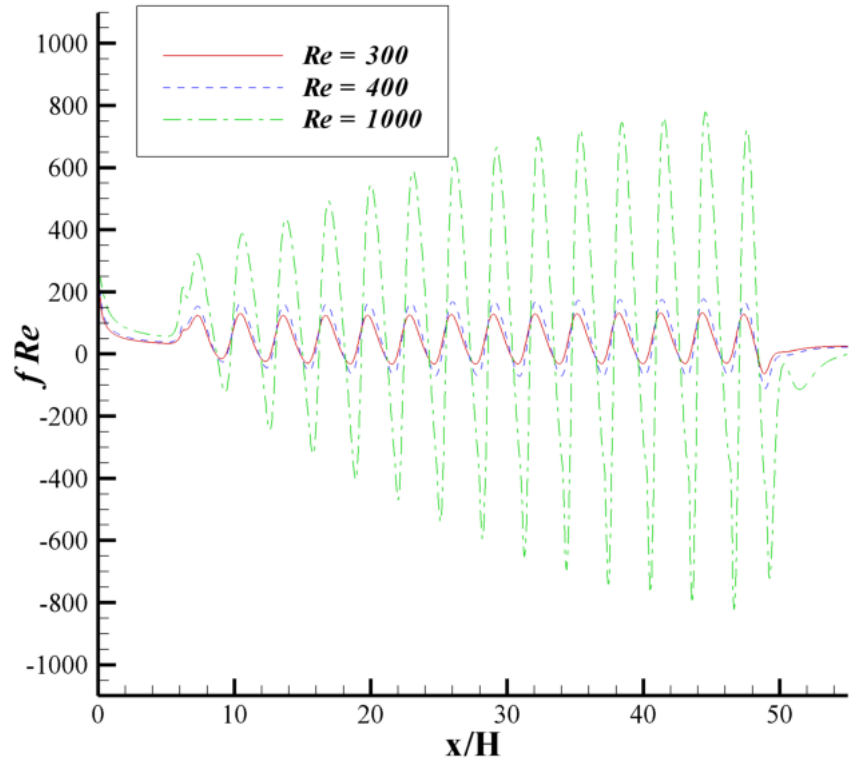

Figure 4.10: *f Re* for laminar flow in a wavy channel, T_{wall} = 400 K

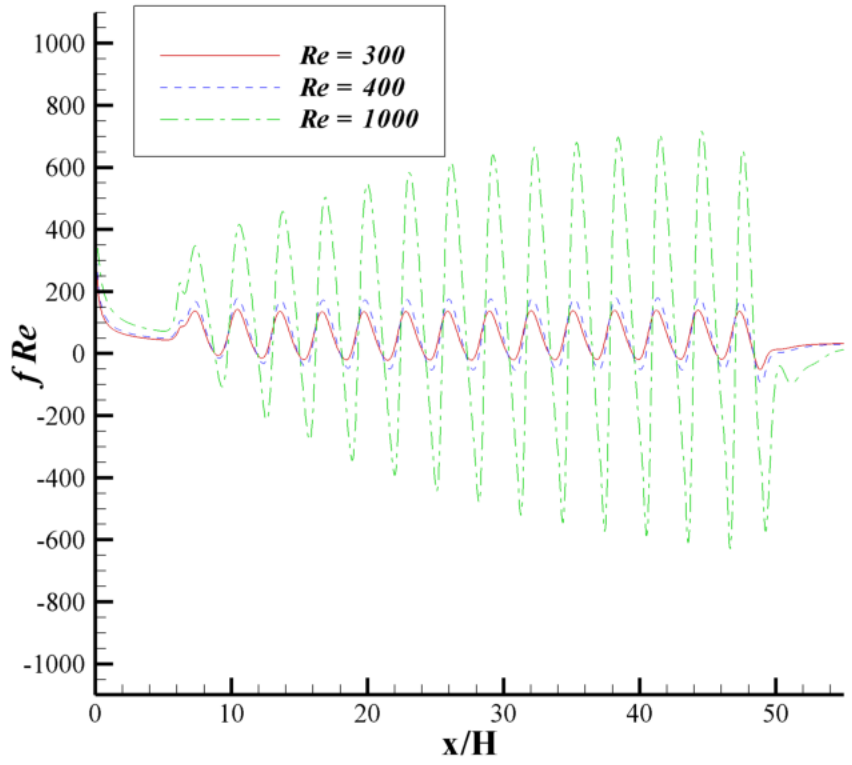

Figure 4.11: *f Re* for laminar flow in a wavy channel, T_{wall} = 500 K

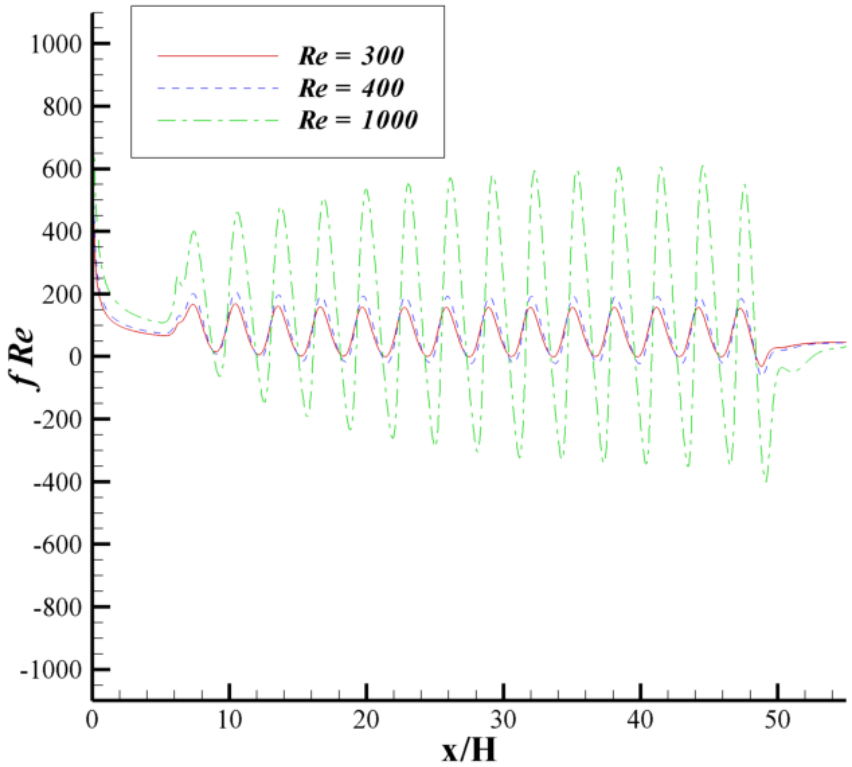

Figure 4.12: *f Re* for laminar flow in a wavy channel, T_{wall} = 750 K

Table 4.2 shows the total pressure drop for each test case. As expected the pressure drop increases with Reynolds number. But it also decreases with increasing temperature gradient. This could be due to the fluid cooling and slowing down, as shown in the contour plots in figures 4.3 and 4.4.

Table 4.2: Pressure drop [Pa] for all laminar wavy channel runs

Wall Temperature	Re = 300	Re = 400	Re = 1000
300 K	38.53	NA	322.97
400 K	56.56	86.45	424.04
500 K	76.56	115.01	523.35
750 K	133.84	195.39	777.92

4.2.4 Heat Transfer

Nusselt number predictions for various Reynolds numbers at wall temperatures of 300 K, 400 K, and 500 K can be seen below in figures 4.13, 4.14, and 4.15 respectively. The plots show that the Nusselt number is strongly dependant on Reynolds number, while only slightly dependant on the wall temperature. The difference between the Nusselt number for a Reynolds number of 300 and a Reynolds number of 400 is slight, while there is a big jump for a Reynolds number of 1000. This could be due to both the large difference in Reynolds number as well as the unsteadiness. Also, similar to the friction factors, the maxima get larger the farther down the channel for the higher Reynolds number flow. This is likely due to the unsteadiness as well. The biggest effect of the wall temperature appears to be a dampening of the oscillations as it is brought closer to the inlet fluid temperature.

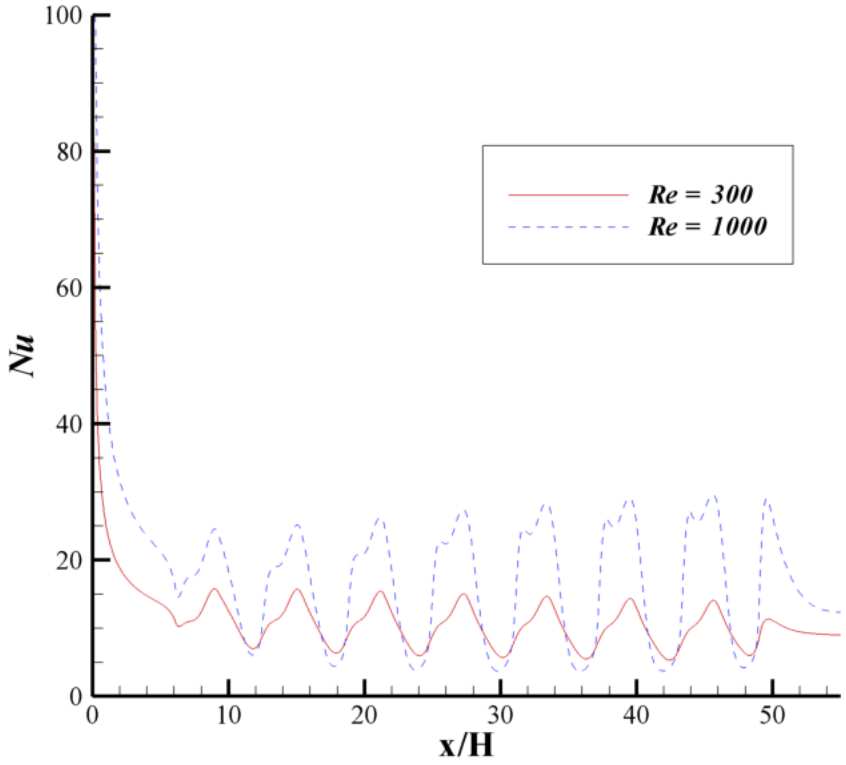

Figure 4.13: Nusselt number for laminar flow in a wavy channel, T_{wall} = 300 K

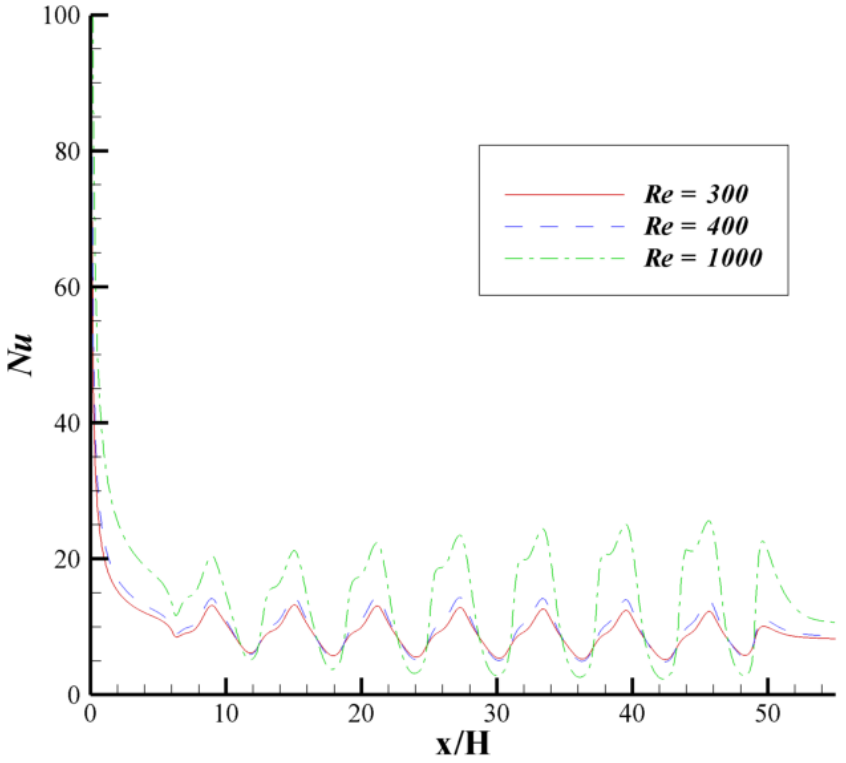

Figure 4.14: Nusselt number for laminar flow in a wavy channel, T_{wall} = 400 K

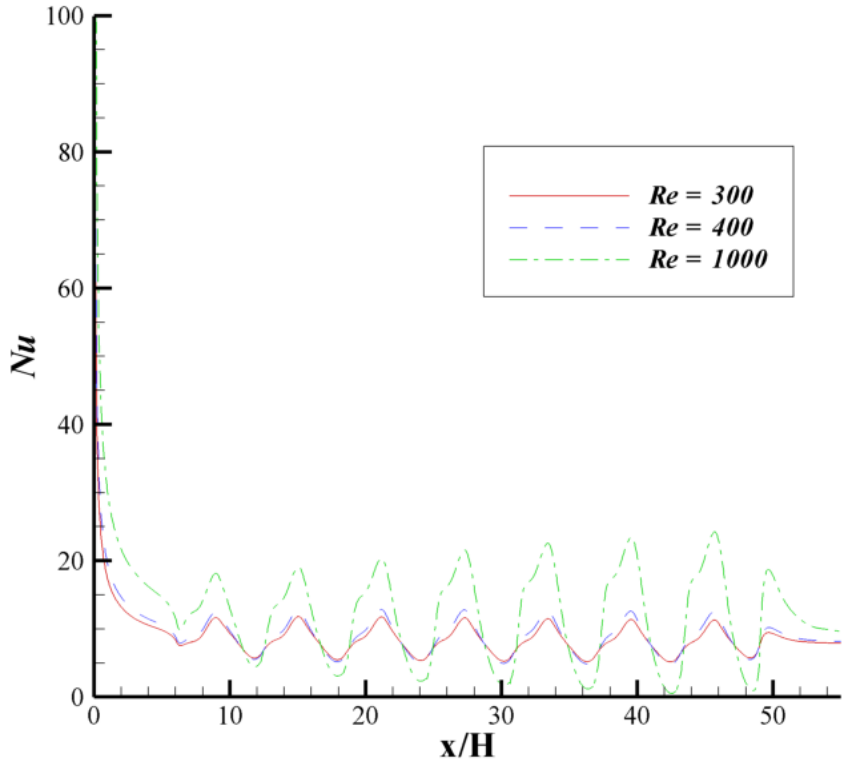

Figure 4.15: Nusselt number for laminar flow in a wavy channel, T_{wall} = 500 K

4.2.5 Deposition

Predicted deposition efficiencies for various Reynolds numbers and wall temperature of 300 K, 400 K, 500 K, and 750 K are shown in figures 4.16, 4.17, 4.18, and 4.19 respectively. The plots show that the deposition efficiencies go down with increasing Reynolds number, which is likely due to the unequal residence times. Since at higher Reynolds number the flow goes through the channel faster, there is less time for the soot particles to deposit. This effect of un-equal residence time was shown by Goodwin [54] for straight channels, and is true also for wavy geometries. The figures also show that deposition is strongly dependant on wall temperature, with the efficiency going down with decreasing temperature gradient. The isothermal case, shown in figure 4.19, predicts very low deposition when compared to the non-isothermal cases, indicating the importance of thermophoresis.

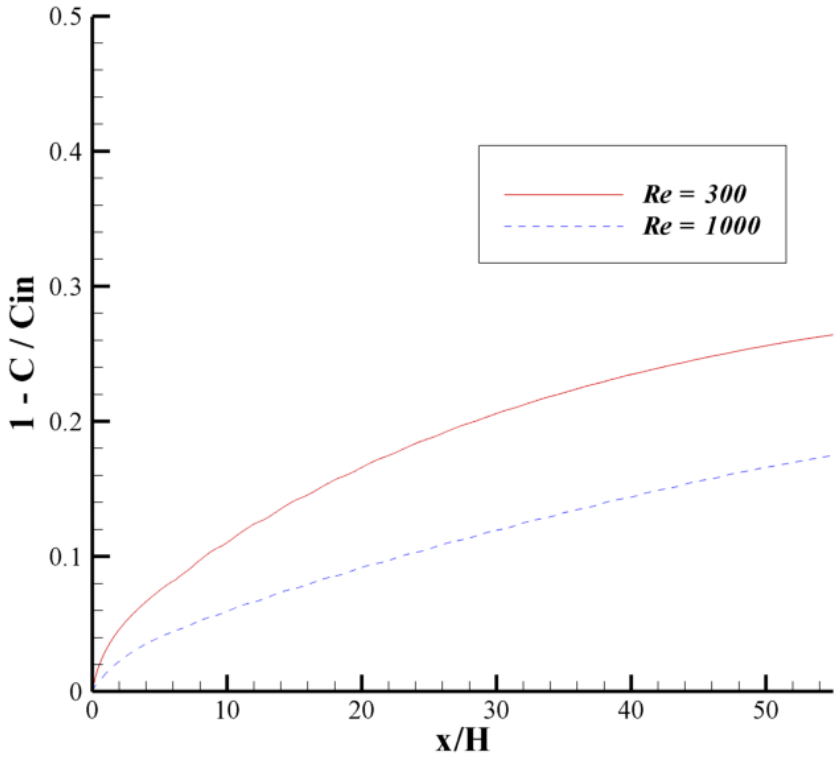

Figure 4.16: Deposition efficiency for laminar flow in a wavy channel, T_{wall} = 300

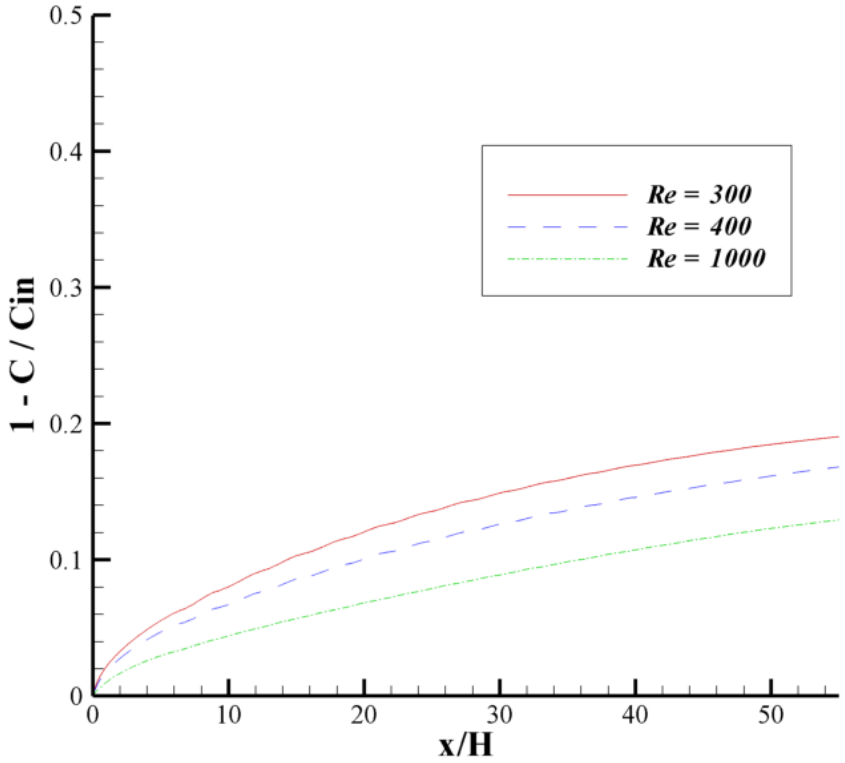

Figure 4.17: Deposition efficiency for laminar flow in a wavy channel, T_{wall} = 400

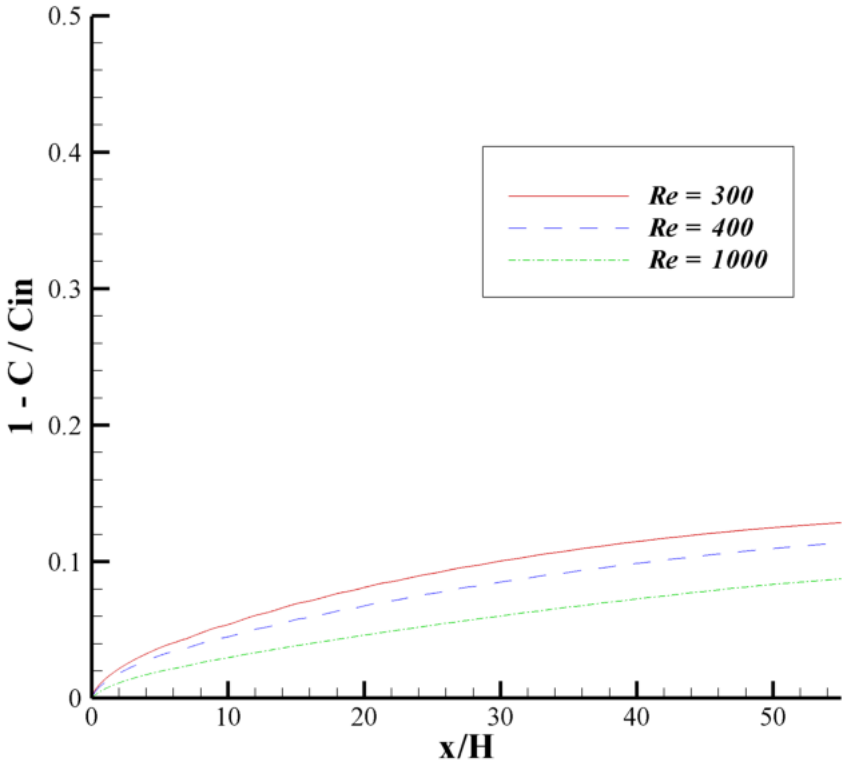

Figure 4.18: Deposition efficiency for laminar flow in a wavy channel, T_{wall} = 500

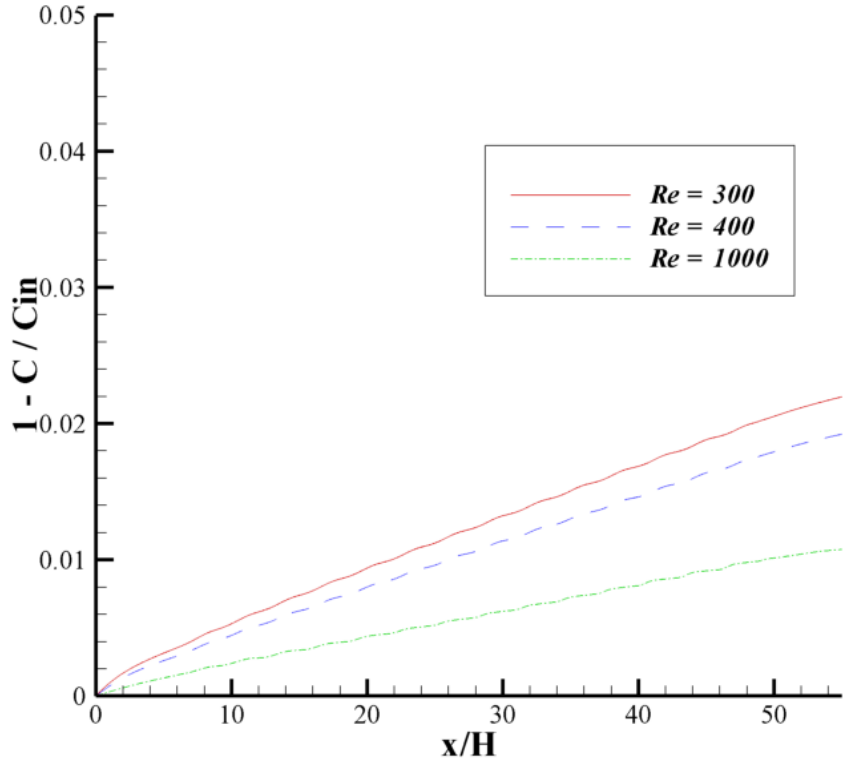

Figure 4.19: Deposition efficiency for laminar flow in a wavy channel, T_{wall} = 750

Table 4.3 below lists the predicted deposition efficiency percentage for all of the laminar way runs. The effect of thermophoresis can be seen clearly, since the efficiency of the isothermal case is nearly an order of magnitude lower than the efficiencies of the non-isothermal cases.

Table 4.3: Summary of Total Deposition Percentage

Reynolds Number	Twall	65x2049
300	750	2.2%
300	500	12.8%
300	400	19.0%
300	300	26.4%
400	750	1.9%
400	500	11.4%
400	400	16.8%
400	300	NA
1000	750	1.0%
1000	500	8.8%
1000	400	12.9%
1000	300	17.5%

4.3 Wavy and Planar Channel Comparison

This section presents the effect of geometry on the pressure drop, heat transfer, and deposition efficiency in laminar flow. The addition of waves to a channel disturbs the boundary layer development and causes recirculation regions to form which increase the heat transfer, soot deposition, and pressure drop. For this portion of the study, wavy and planar channels were studied for a Reynolds number of 400 and wall temperatures of 400 K, 500 K, and 750 K. The inlet fluid temperature was once again held at a constant 750 K. Runs were not performed for a wall temperature of 300 K due to the flow becoming unsteady for that case.

4.3.1 Pressure Drop

Figures 4.20, 4.21, and 4.22 show the predicted values of f*Re for planar and wavy channels with wall temperatures of 400 K, 500 K, and 750 K respectively. The wavy and planar curves match exactly at the inlet and deviate only once the waviness begins. Also it appears that although the f*Re dips below the values for the planar channel, the average value for the wavy channel is larger than for the planar channel. These trends appear to be independent of wall temperature, as all three plots show them.

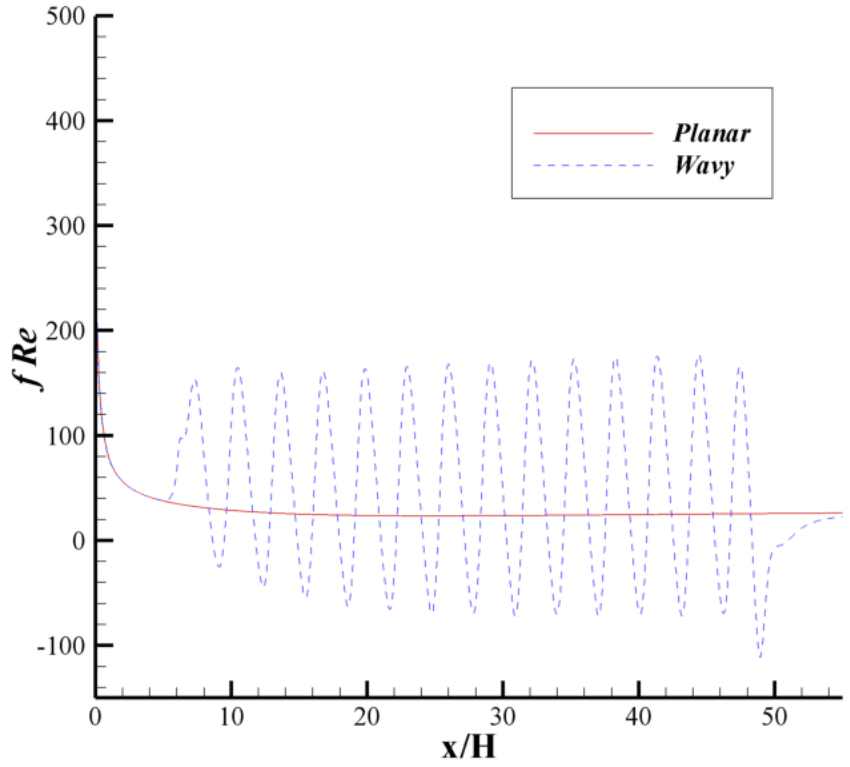

Figure 4.20: Comparison of *f Re* in wavy and planar channels, Re = 400, T_{wall} = 400 K

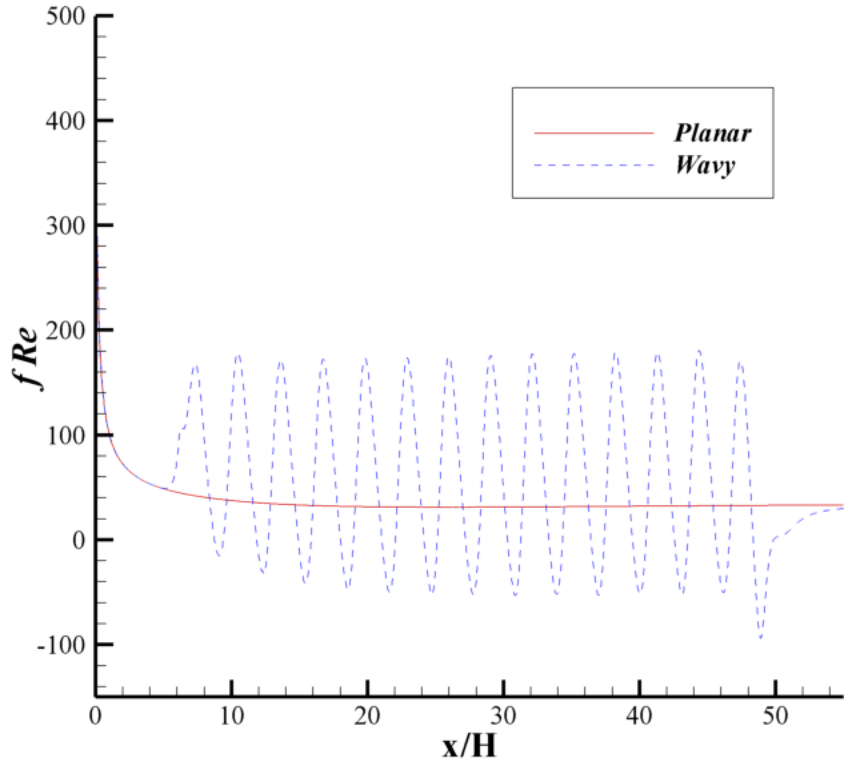

Figure 4.21: Comparison of *f Re* in wavy and planar channels, Re = 400, T_{wall} = 500 K

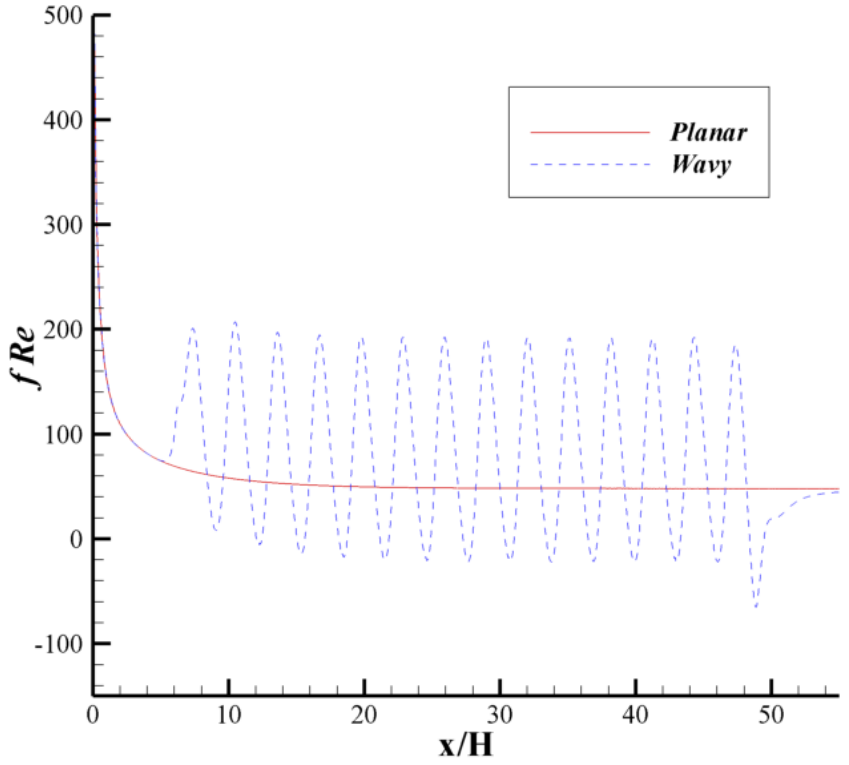

Figure 4.22: Comparison of *f Re* in wavy and planar channels, Re = 400, T_{wall} = 750 K

Table 4.4 below lists the total pressure drops for both the wavy and planar channel runs. The wavy channel geometry clearly increases the pressure drop. The pressure drop seems to be about 1.5 times higher in the wavy channel for the non-isothermal cases, and the isothermal cases shows a slightly lower increase.

Table 4.4: Pressure drops [Pa] for wavy and planar channels, Re = 400

Wall Temperature	Wavy Channel	Planar Channel
400 K	86.45	54.69
500 K	115.01	77.51
750 K	195.39	143.18

4.3.2 Heat Transfer

Direct comparisons of the predicted Nusselt numbers for planar and wavy channels are shown below for two wall temperatures, 400 K and 500 K, in figures 4.23 and 4.24 respectively. Similar to the f*Re plots, the planar and wavy curves match exactly at the inlet and deviate once the wavy geometry begins. But although the wavy channel curve oscillates around the planar channel curve, the average Nusselt number for the wavy channel seems to be very close to the planar channel value. This could be due to the low Reynolds number allowing the flow to follow the curves exactly and behave like a planar channel. The positive heat transfer effect of the wavy geometry could be increased by increasing the either the Reynolds number or the severity of the waviness.

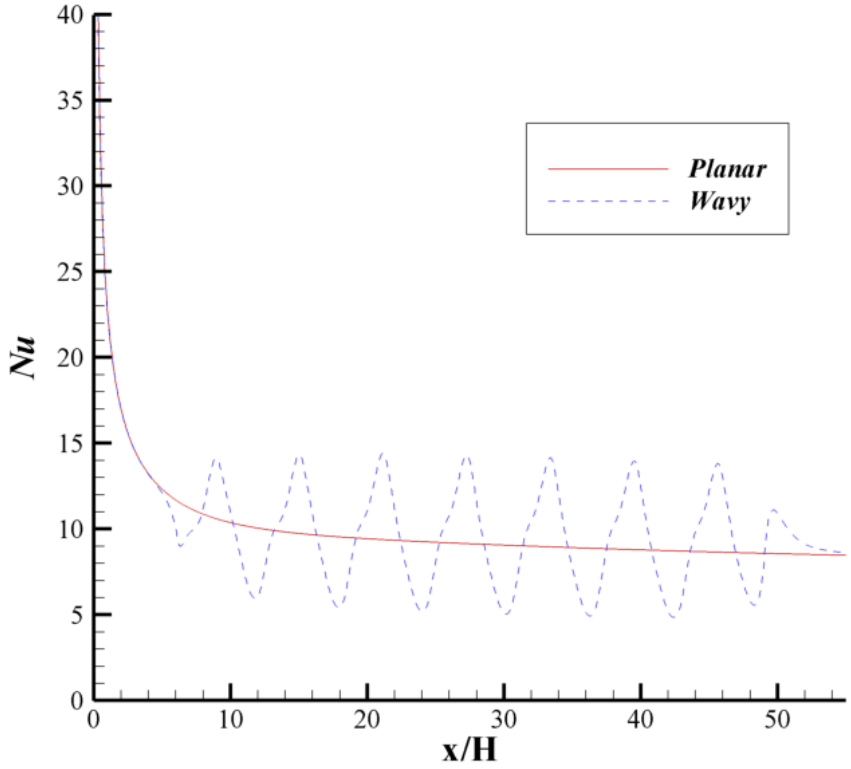

Figure 4.23 Comparison of Nusselt number in wavy and planar channels, Re = 400, T_{wall} = 400 K

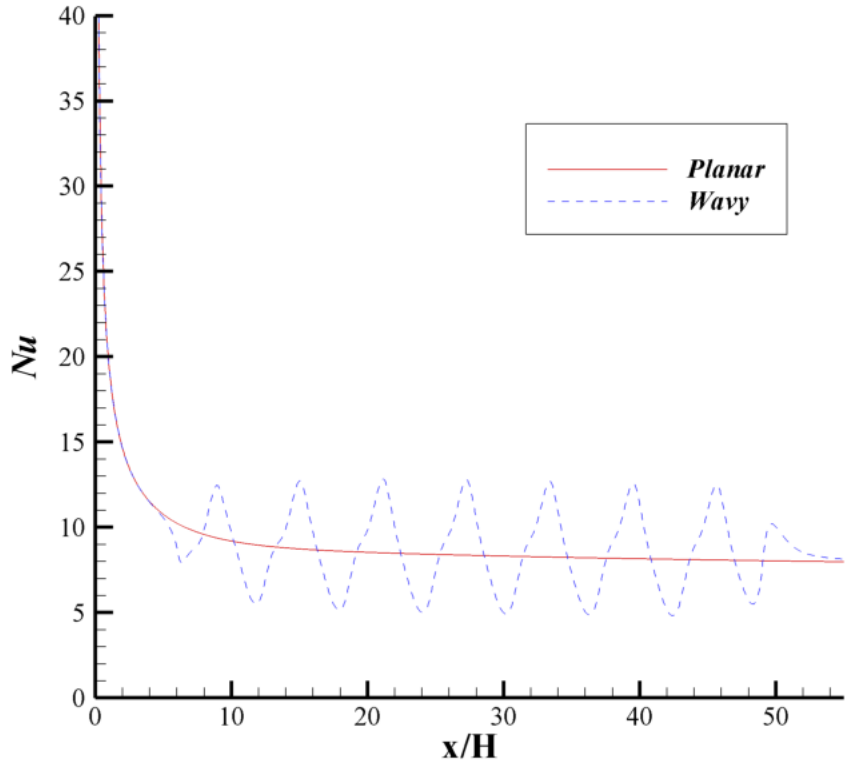

Figure 4.24: Comparison of Nusselt number in wavy and planar channels, Re = 400, T_{wall} = 500 K

4.3.3 Deposition

Deposition efficiency predictions for planar and wavy channels for wall temperature for 400 K, 500 K, and 750 K, are shown in figures 4.25, 4.26, and 4.27 respectively. For the two non-isothermal cases, shown in figures 4.25 and 4.26, there is nearly no difference between the wavy and planar channels. But for the isothermal case in figure 4.27, the wavy channel causes significantly more deposition. This shows that the geometry is important for Brownian diffusion but once a temperature gradient is applied thermophoresis dominates. So for a Reynolds number of 400, the geometry effect is negligible.

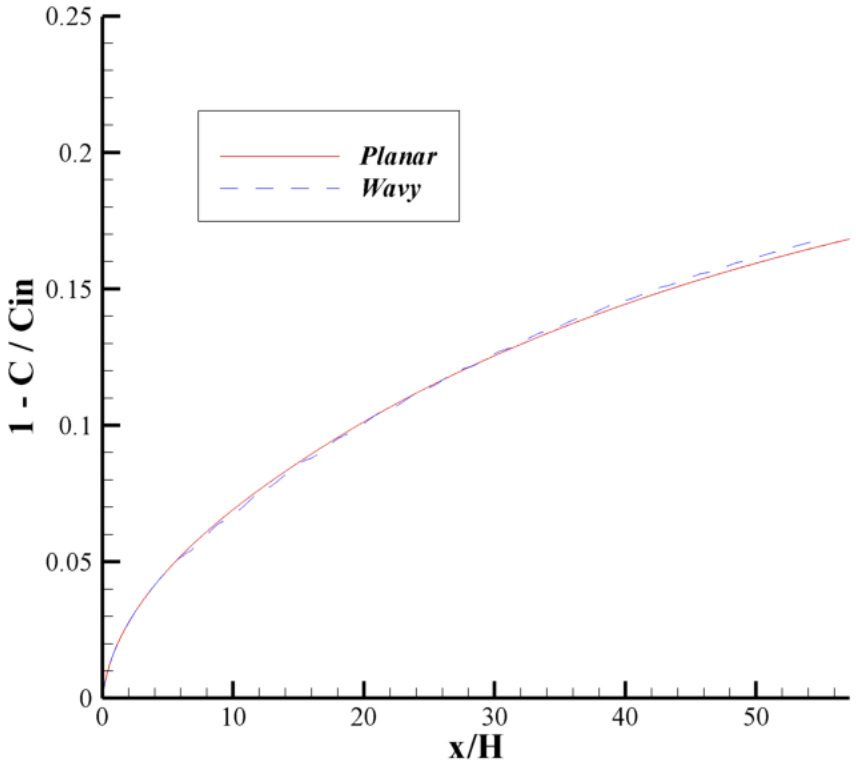

Figure 4.25: Comparison of deposition in wavy and planar channels, Re = 400, T_{wall} = 400 K

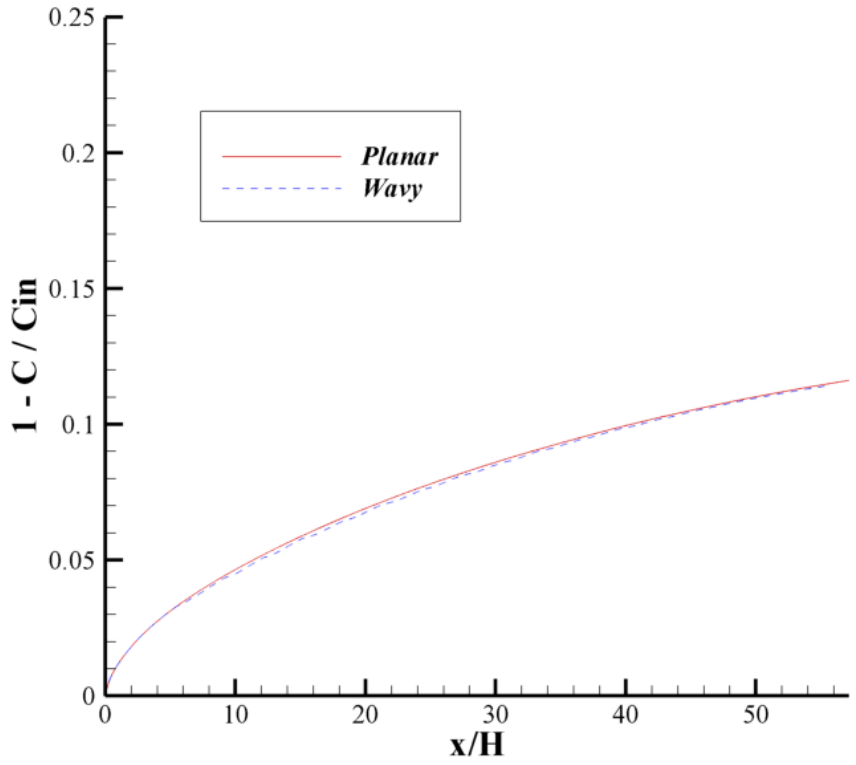

Figure 4.26: Comparison of deposition in wavy and planar channels, Re = 400, T_{wall} = 500 K

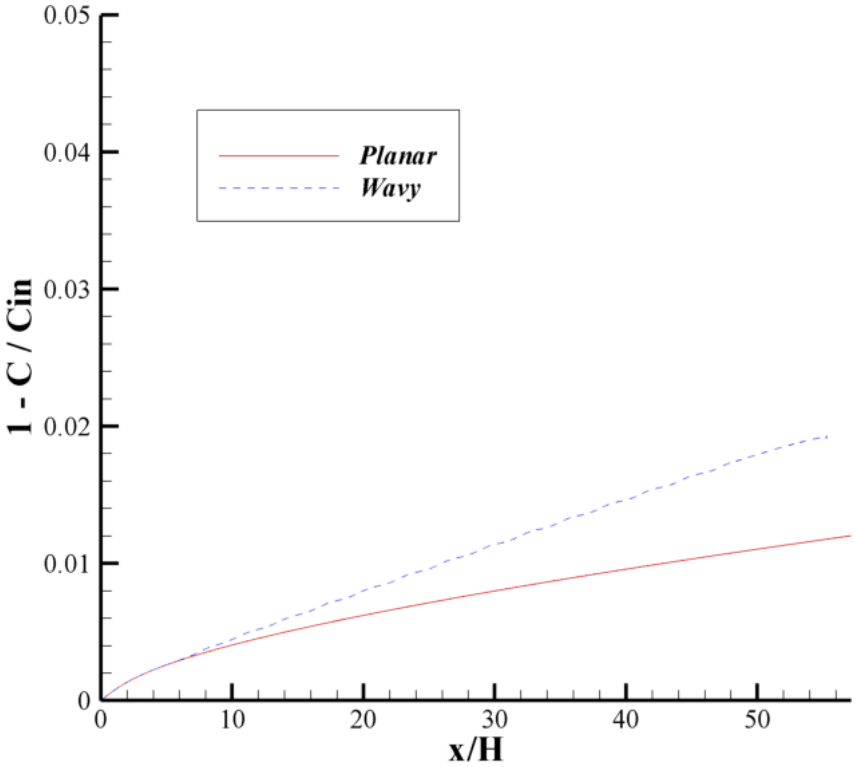

Figure 4.27: Comparison of deposition in wavy and planar channels, Re = 400, T_{wall} = 750 K

Table 4.5 below summarizes the total deposition for all of the wavy and planar channel runs. As shown in the previous plots, the difference between the wavy and planar channels is negligible for the non-isothermal cases. But for the isothermal case the wavy channel causes a deposition efficiency over 1.5 times as high as the planar channel.

Table 4.5: Summary of total deposition percentage for wavy and planar channels

Reynolds Number	Twall	Wavy	Planar
400	750	1.9%	1.2%
400	500	11.4%	11.6%
400	400	16.8%	16.8%

4.4 Laminar Results Summary

This section presented results for laminar flow in wavy and planar channels. For wavy channels, the pressure drop was shown to increase with increasing wall temperature and decrease with increasing temperature gradient. The Nusselt number was shown to increase with both increasing Reynolds number and increasing temperature gradient. Deposition efficiency was shown to decrease with Reynolds number and increase with temperature gradient. When comparing wavy and planar channels, the pressure drop, heat transfer, and deposition efficiency were all shown to be higher in wavy channels. The next chapter will present similar results, but for turbulent flow.

Chapter 5

Turbulence Study

5.1 Introduction

Since the EGR coolers studied in this thesis have fast moving exhaust gas flowing through them, it is important to study the effects of turbulence on the fluid flow, heat transfer, and soot deposition in a wavy channel. Turbulent flow should increase the soot deposition due to the increased diffusion and impaction. This chapter will start with a study of turbulent flow in a wavy channel. The effect of Reynolds number and temperature gradient on the heat transfer, the pressure drop, and the soot deposition will be investigated. Then wavy channels will be compared with planar channels in order to show the effect of geometry on the same factors.

5.2 Wavy Channel Study

The geometry for the turbulent study is the same seven wave channel used in the laminar study detailed in chapter 4. The grid used is also the same as the grid in chapter 4. Three Reynolds numbers and four different wall temperatures will be studied with a constant inlet fluid temperature of 750 K. A summary of the runs is shown below in table 5.1. For the wavy runs with Reynolds number equal to 10,000 the relaxation factors for momentum, pressure, energy, turbulent kinetic energy, turbulent dissipation, turbulent viscosity, and density were all set at 0.5. The runs then required roughly 11,000 iterations to converge. For the rest of the wavy runs the relaxation factors for pressure, turbulent kinetic energy, turbulent dissipation, and turbulent viscosity had to be lowered to 0.3 to achieve stability. Due to the lowered relaxation factors the runs took around 16,000 iterations to converge.

Table 5.1: Matrix of turbulent wavy channel simulations

Reynolds Number	Inlet Temperature [K]	Wall Temperature [K]
Turbulent Runs		
5000	750	750
5000	750	500
5000	750	400
5000	750	300
7500	750	750
7500	750	500
7500	750	400
7500	750	300
10000	750	750
10000	750	500
10000	750	400
10000	750	300

Due to the high Schmidt number a finer grid was needed to accurately model the soot deposition. So the concentration was solved on two successively finer grids, 129x4097 with 2% stretching and 257x8193 with 2% stretching, using the flow field developed by the original grid. The concentration solver on the medium grid takes about 600 iterations to converge and the finest takes about 1600.

5.2.1 Flow Field

Shown below are inlet and outlet contour plots of u-velocity, temperature, and concentration. Due to the length of the channels the contours were once again broken into two figures so that a better view could be obtained. Figures 5.1, 5.3, and 5.5 show the inlet contours and figures 5.2, 5.4, and 5.6 show the outlet contours of u-velocity, temperature, and concentration respectively. For all figures the Reynolds number is 5000 and the wall temperature is 300 K. The flow development can be seen clearly in all three figures, with the momentum becoming fully developed after 3 waves. Due to the long channel the temperature of the fluid is nearly the same temperature as the wall, as seen in figure 5.4. Also because of the length of the channel, as well as the high temperature gradient, a significant drop in concentration has occurred, shown in figure 5.6. Also by comparing figures 5.3 and 5.5, it can be seen that the temperature boundary layer grows faster than the concentration boundary layer.

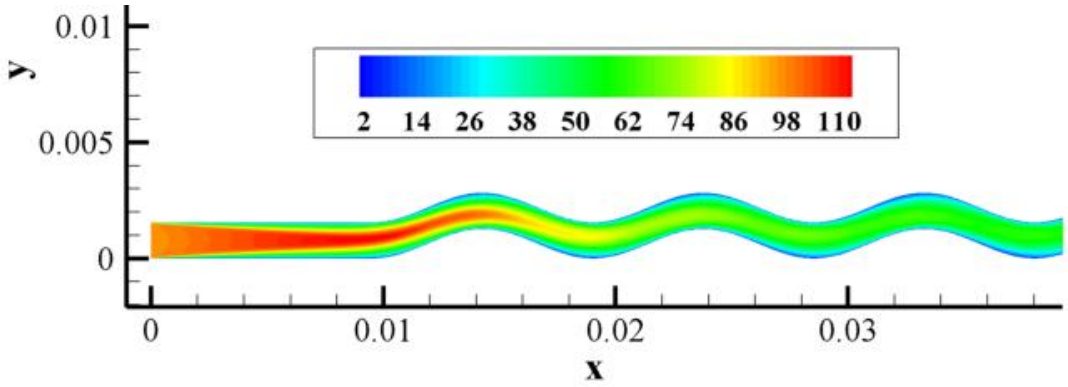

Figure 5.1: Contour of u-velocity at the inlet, Re = 5000 and T_{wall} = 300

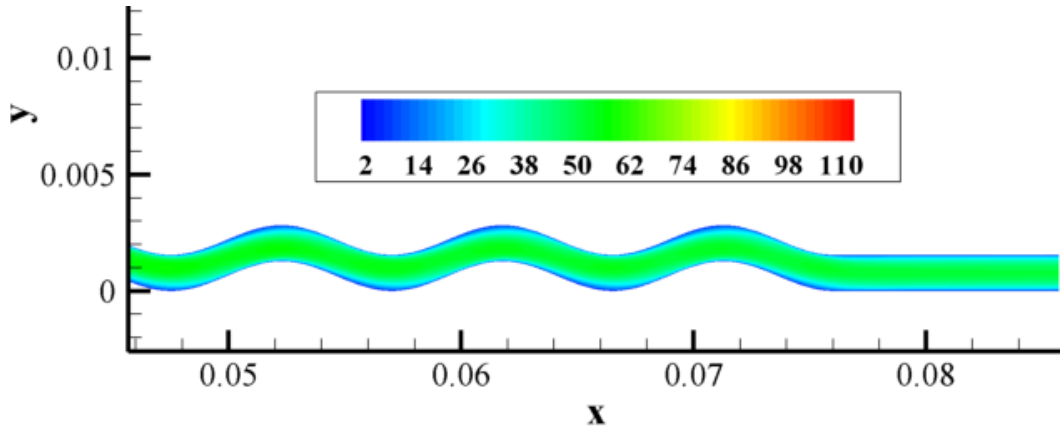

Figure 5.2: Contour of u-velocity at the outlet, Re = 5000 and T_{wall} = 300

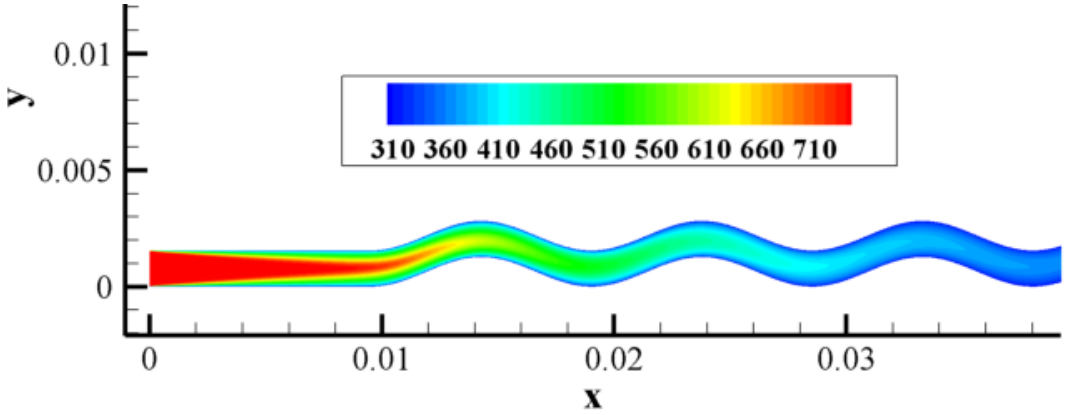

Figure 5.3: Contour of temperature at the inlet, Re = 5000 and T_{wall} = 300

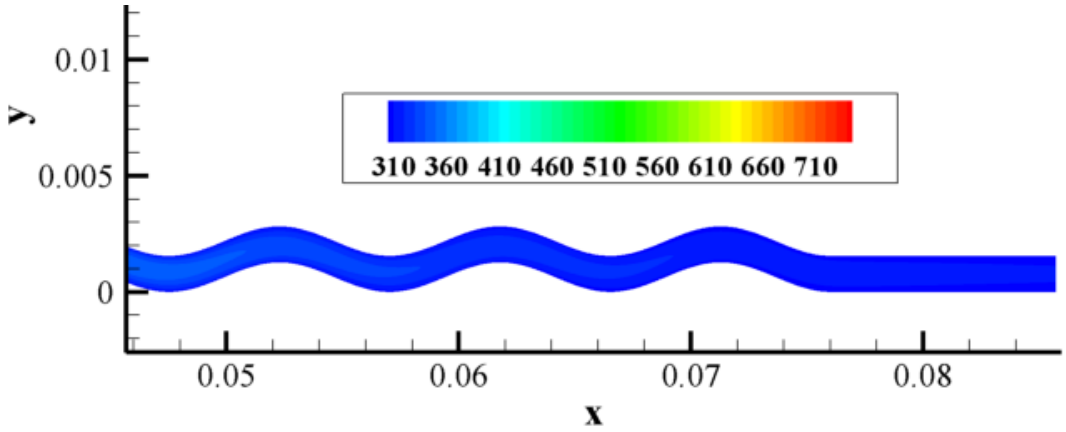

Figure 5.4: Contour of temperature at the outlet, Re = 5000 and T_{wall} = 300

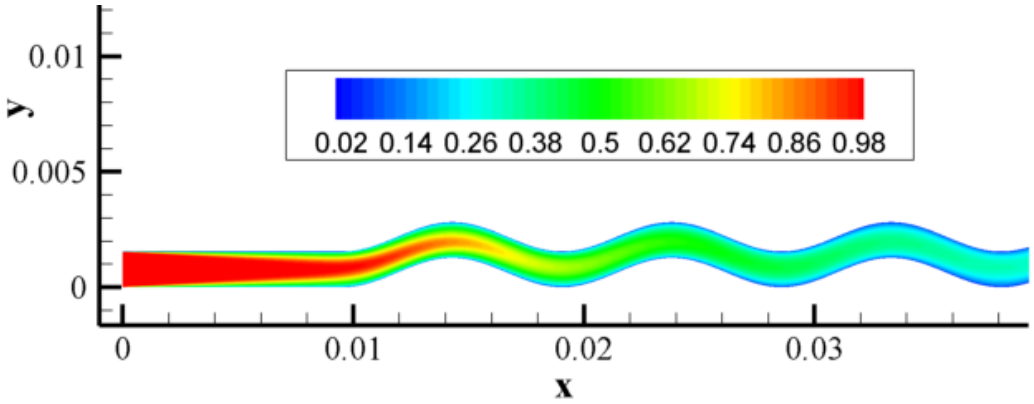

Figure 5.5: Contour of concentration at the inlet, Re = 5000 and T_{wall} = 300

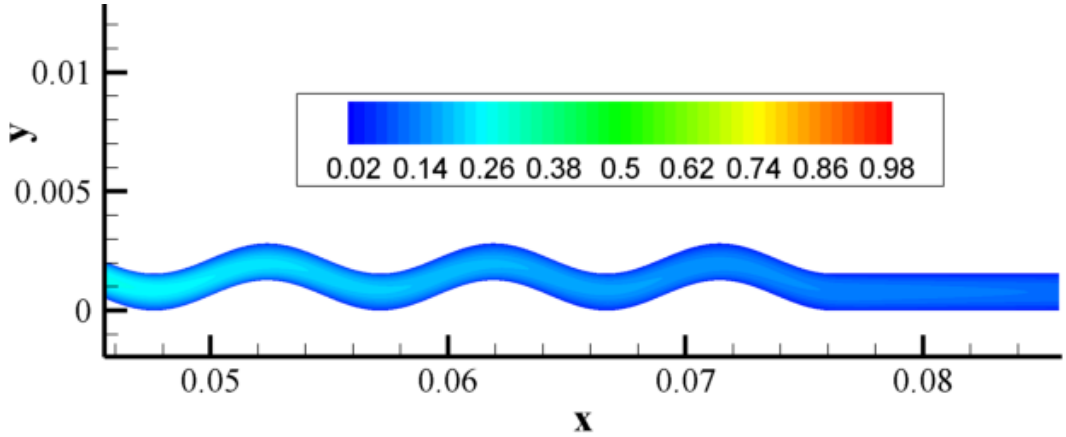

Figure 5.6: Contour of concentration at the outlet, Re = 5000 and T_{wall} = 300

5.2.2 Pressure Drop

Figures 5.7, 5.8, 5.9, and 5.10 show predictions for the product of friction factor and the inlet Reynolds (f*Re) number for four different wall temperatures with a constant inlet fluid temperature. Figures 5.7, 5.8, 5.9, and 5.10 are for wall temperatures of 300 K, 400 K, 500 K, and 750 K respectively. As with laminar flow, f*Re increases with increasing Reynolds number. Also the f*Re is shown in all figures to oscillate periodically, similar to the laminar results, because of the wavy geometry. Each spike in the f*Re corresponds with a change in the direction of the fluid. But the values do not go drastically negative unlike the laminar channels. The figures also show that with decreasing temperature gradient the overall values for f*Re decrease.

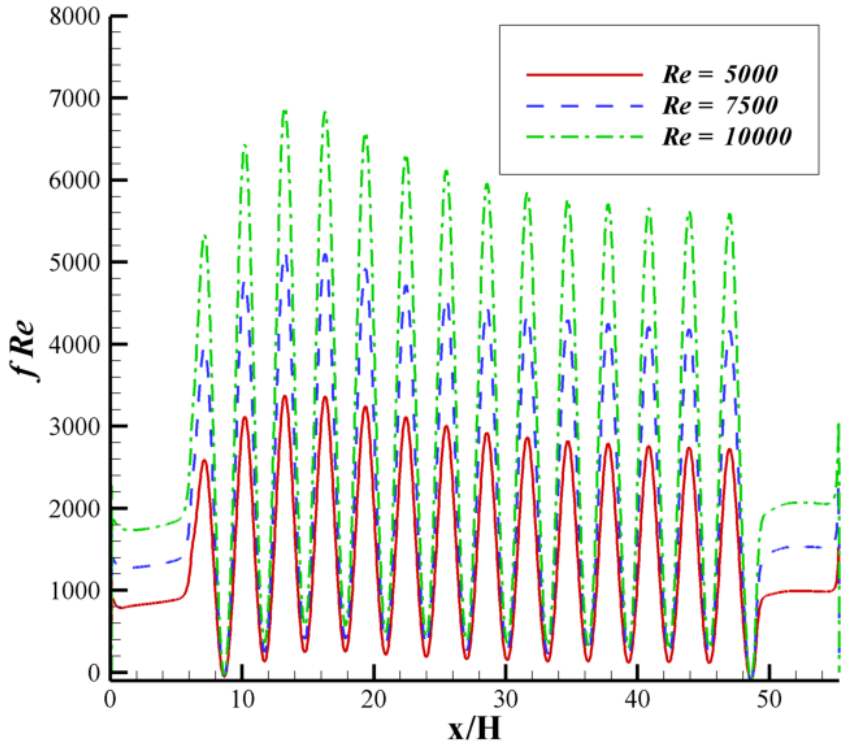

Figure 5.7: *f Re* for turbulent flow in a wavy channel, T_{wall} = 300 K

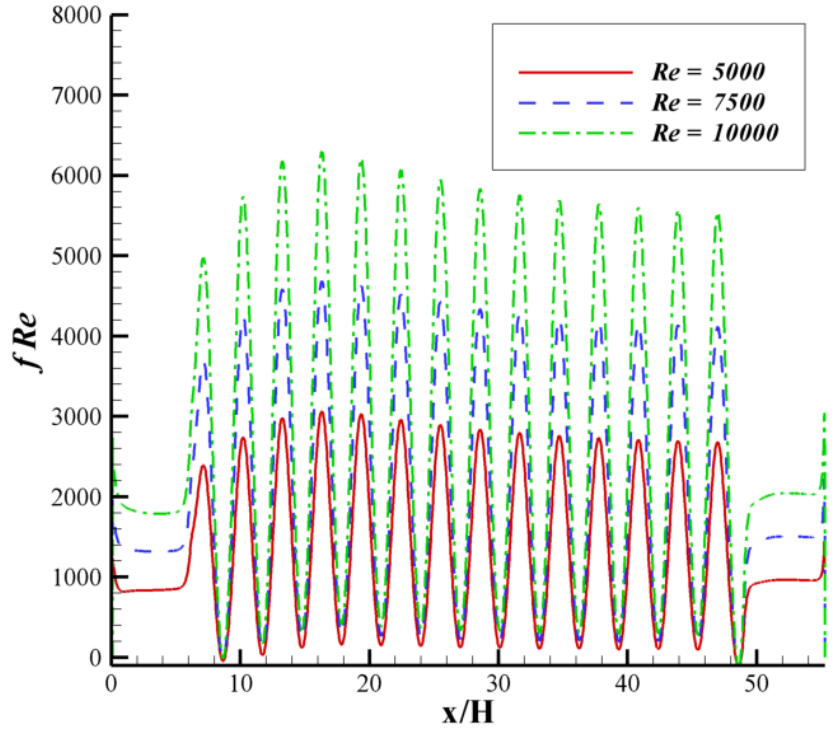

Figure 5.8: *f Re* for turbulent flow in a wavy channel, T_{wall} = 400 K

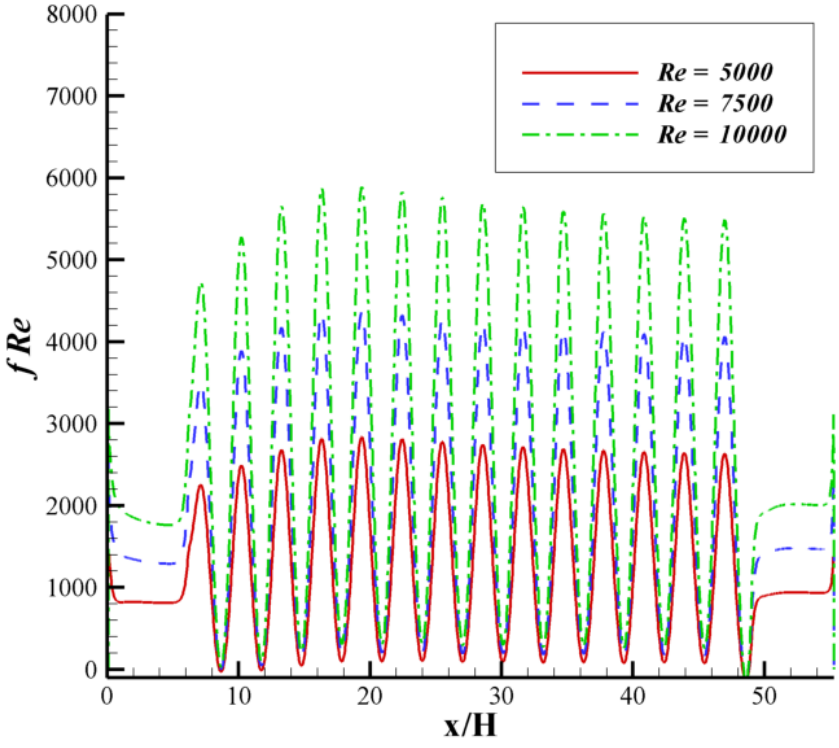

Figure 5.9: *f Re* for turbulent flow in a wavy channel, T_{wall} = 500 K

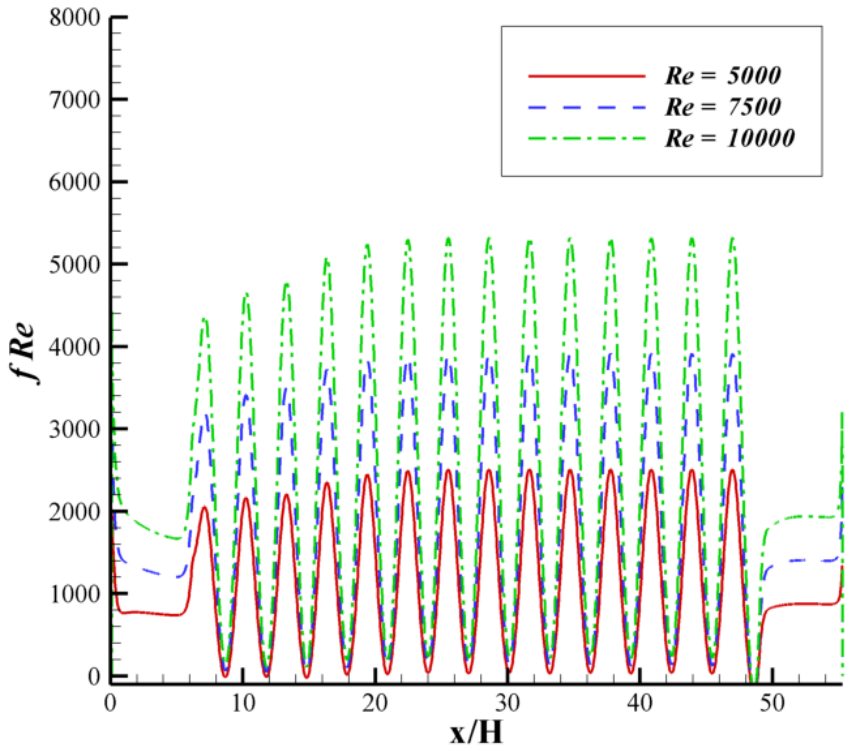

Figure 5.10: *f Re* for turbulent flow in a wavy channel, T_{wall} = 750 K

Also important is the overall pressure drop across the channel. Table 5.2 gives all the pressure drops for the turbulent wavy runs. As expected, the pressure drops for the turbulent runs are much higher than for the laminar runs. Also it shows that like the laminar runs, both decreasing temperature gradient and increasing Reynolds number cause the pressure drop to increase.

Table 5.2: Pressure drop [Pa] for all turbulent wavy channel runs

Wall Temperature	Re = 5000	Re = 7500	Re = 10000
300 K	21,350	48,961	87,786
400 K	25,053	58,073	104,613
500 K	27,909	65,448	118,529
750 K	32,544	78,489	144,292

5.2.3 Heat Transfer

Figures 5.11, 5.12, and 5.13 show the predicted Nusselt numbers for three different Reynolds numbers for wall temperatures of 300 K, 400 K, and 500 K. The most notable feature is the lack of dependence of the Nusselt number on the Reynolds number. Due to the wavy geometry the plots show peaks and valleys similar to the friction plots in the previous section. Each peak corresponds to the top of each wave and each valley corresponds to the bottom of each wave. The plots also show how the flow is fully developed after the third wave. Finally, it appears that the wall temperature does not affect the Nusselt number, so the geometry is the main factor. Also, as expected, the average Nusselt number for the turbulent flow is higher than for laminar flows in chapter 4.

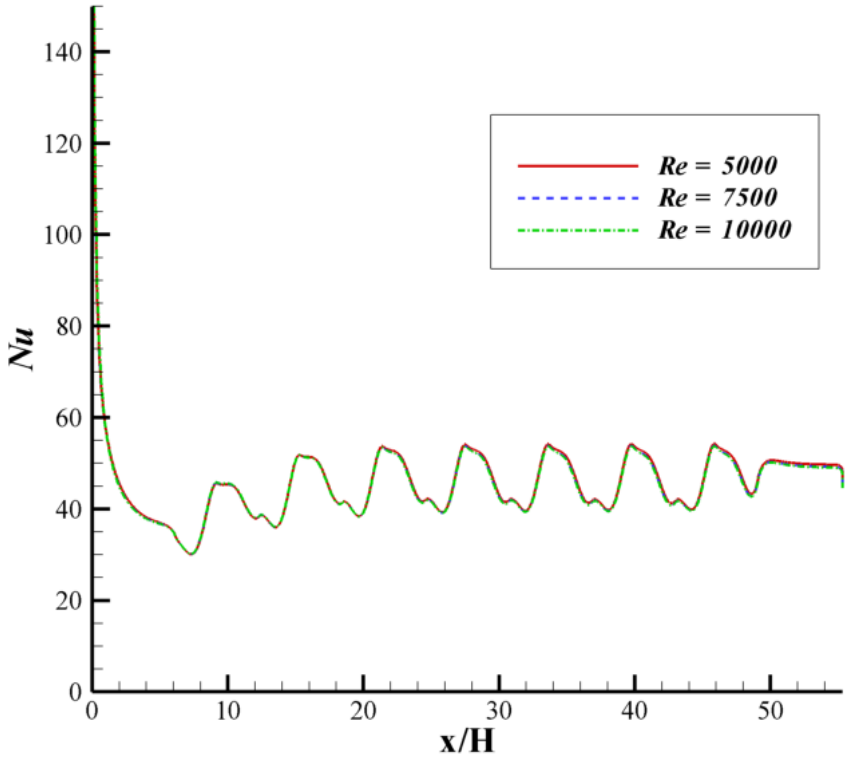

Figure 5.11: Nusselt number for turbulent flow in a wavy channel, T_{wall} = 300 K

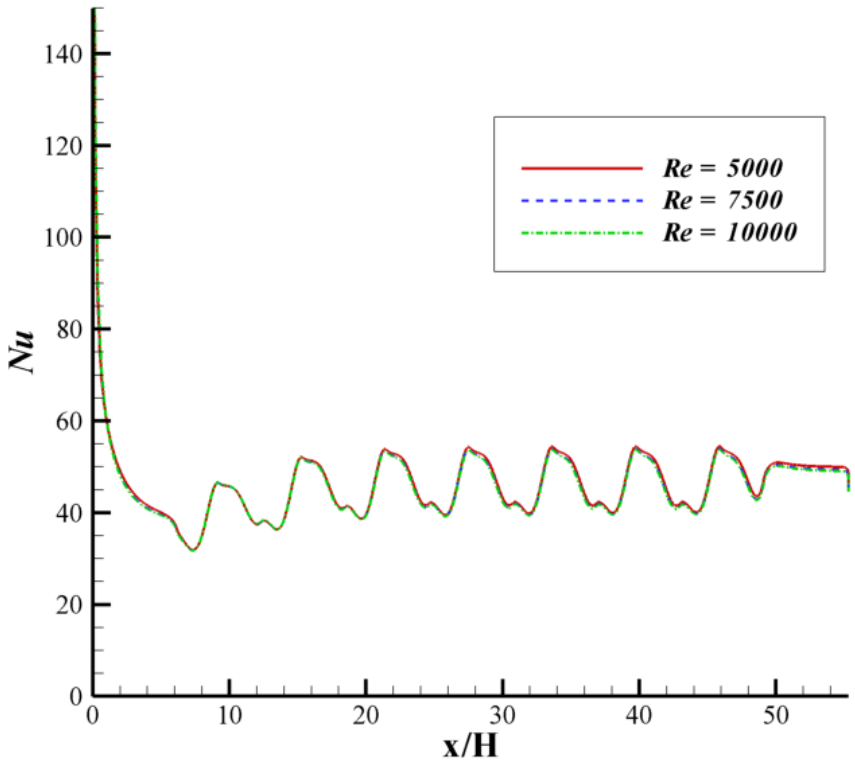

Figure 5.12: Nusselt number for turbulent flow in a wavy channel, T_{wall} = 400 K

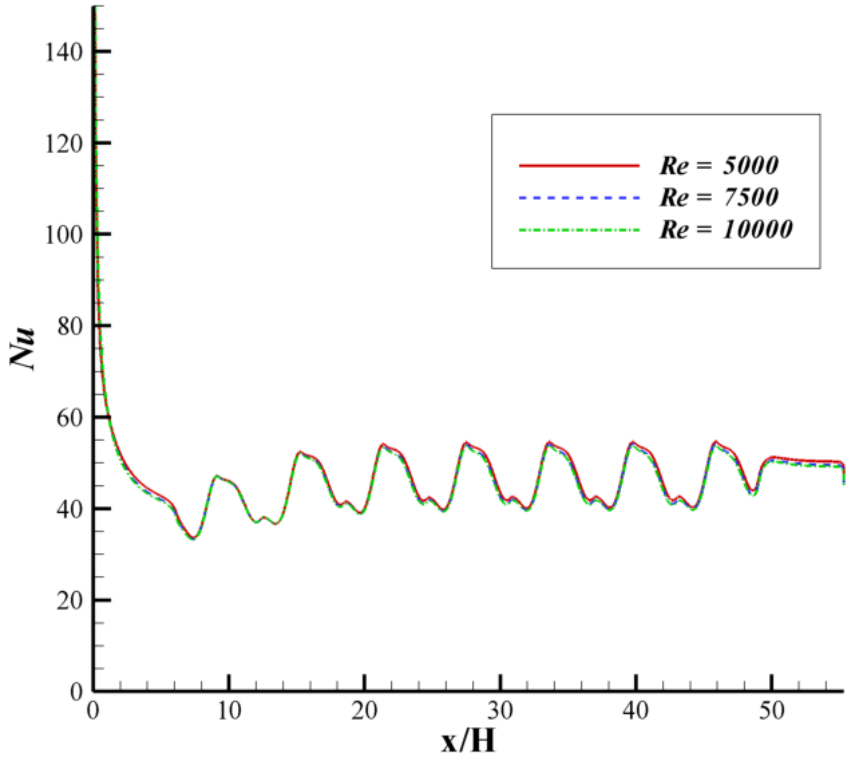

Figure 5.13: Nusselt number for turbulent flow in a wavy channel, T_{wall} = 500 K

5.2.4 Deposition

Figures 5.14, 5.15, 5.16, and 5.17 show the predicted deposition efficiencies for turbulent flow in a wavy channel. The plots show that the Reynolds number causes a slight increase in the deposition efficiency. By comparing the four plots, it is clear that for a constant inlet temperature the deposition efficiency increases with decreasing wall temperature. In other words, as expected, the higher the temperature gradient the more soot is deposited. This is due to thermophoresis acting on the particles in the presence of a temperature gradient. But, by looking at the isothermal case in figure 5.17, it is clear that turbulent diffusion is an important mechanism in soot deposition. In laminar flow, thermophoresis is the dominant mechanism but in turbulent flow, although thermophoresis is important, eddy diffusion dominates. Finally, all of the non-isothermal plots show a steep initial slope that decreases farther down the channel. This is due to the fluid cooling and thermophoresis becoming less important. Therefore it is logical for the isothermal case shown in figure 5.17 to have a nearly constant slope due to the lack of a temperature gradient.

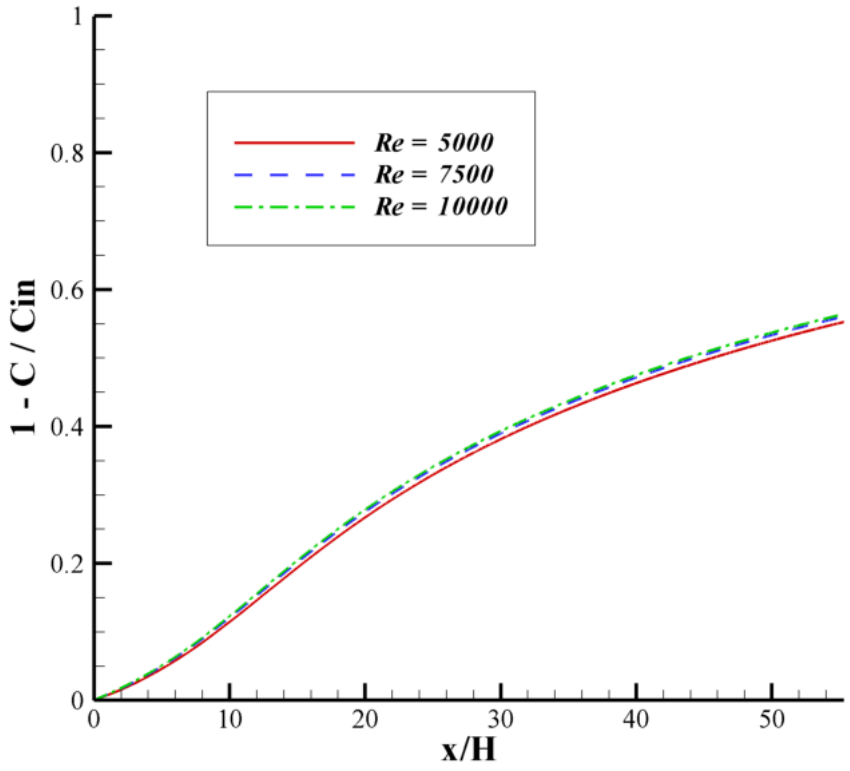

Figure 5.14: Deposition efficiency for turbulent flow in a wavy channel, T_{wall} = 300

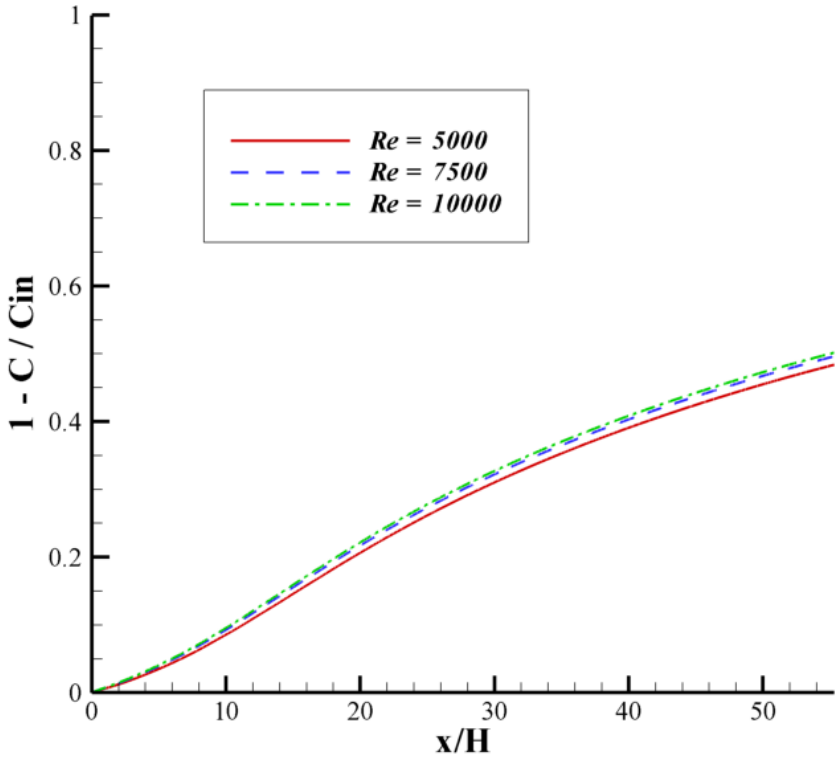

Figure 5.15: Deposition efficiency for turbulent flow in a wavy channel, T_{wall} = 400

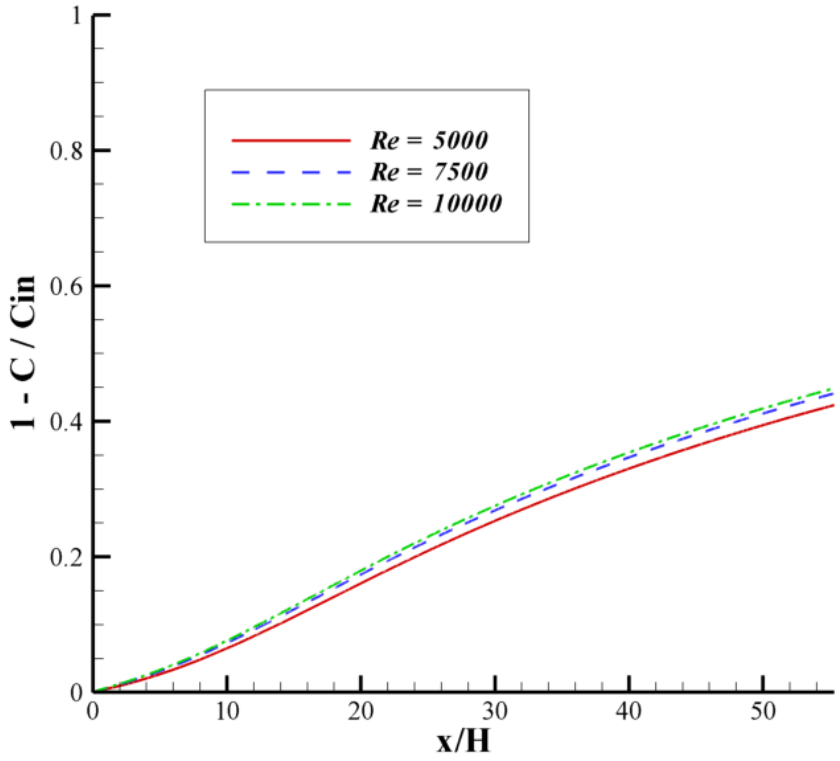

Figure 5.16: Deposition efficiency for turbulent flow in a wavy channel, T_{wall} = 500

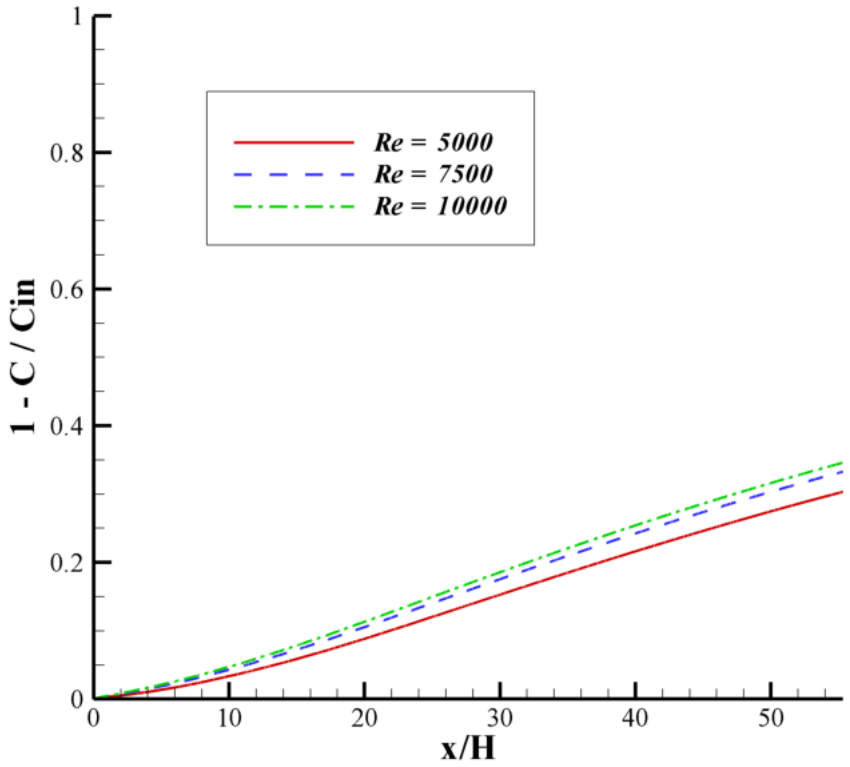

Figure 5.17: Deposition efficiency for turbulent flow in a wavy channel, T_{wall} = 750

Below in table 5.3 the total deposition efficiencies for all of the runs are listed. All three grids used are shown as well to illustrate the required grid refinement in order to accurately model the soot deposition. As stated before the results show that the deposition increases with both increasing temperature gradient and increasing Reynolds number. Although the trends appear correct, the overall depositions appear large. This may be a result of the turbulence modeling. However, in the absence of experimental data, the accuracy of the current predictions cannot be ascertained.

Table 5.3: Summary of Total Deposition Percentage

Reynolds Number	Twall	65x2049	129x4097	257x8193
5000	750	87.7%	38.9%	30.3%
5000	500	94.6%	52.2%	42.3%
5000	400	96.6%	58.5%	48.3%
5000	300	98.1%	65.4%	55.2%
7500	750	90.3%	42.5%	33.2%
7500	500	95.5%	54.2%	44.1%
7500	400	97.0%	59.8%	49.6%
7500	300	98.2%	66.2%	56.0%
10000	750	91.4%	44.0%	34.5%
10000	500	95.8%	55.0%	44.8%
10000	400	97.2%	60.4%	50.1%
10000	300	98.3%	66.6%	56.4%

5.3 Wavy and Planar Channel Comparison

In order to show the effect of the wavy channel geometry on turbulent flow, flow in a planar channel is compared to flow in a wavy channel. The heat transfer, pressure drop, and soot deposition are compared for identical cases. One Reynolds number, 7500, is used for both the planar and wavy channels. The inlet fluid temperature is set at 750 K and four different wall temperatures are used; 300 K, 400 K, 500 K, and 750 K. The relaxation factors were the same as for the wavy channel runs described in section 5.2.

5.3.1 Pressure Drop

Figures 5.18, 5.19, 5.20, and 5.21 below show a direct comparison between the predicted f*Re for wavy and planar channels at four different temperature gradients. First, the plots show that the f*Re's are identical at the straight inlet section before any waviness begins. The lines follow the same trend and the plots show that the average f*Re's for the wavy channels are higher than for the planar channels. This increased friction due to the wavy geometry agrees with previous research studies on wavy channels covered in chapter 2.

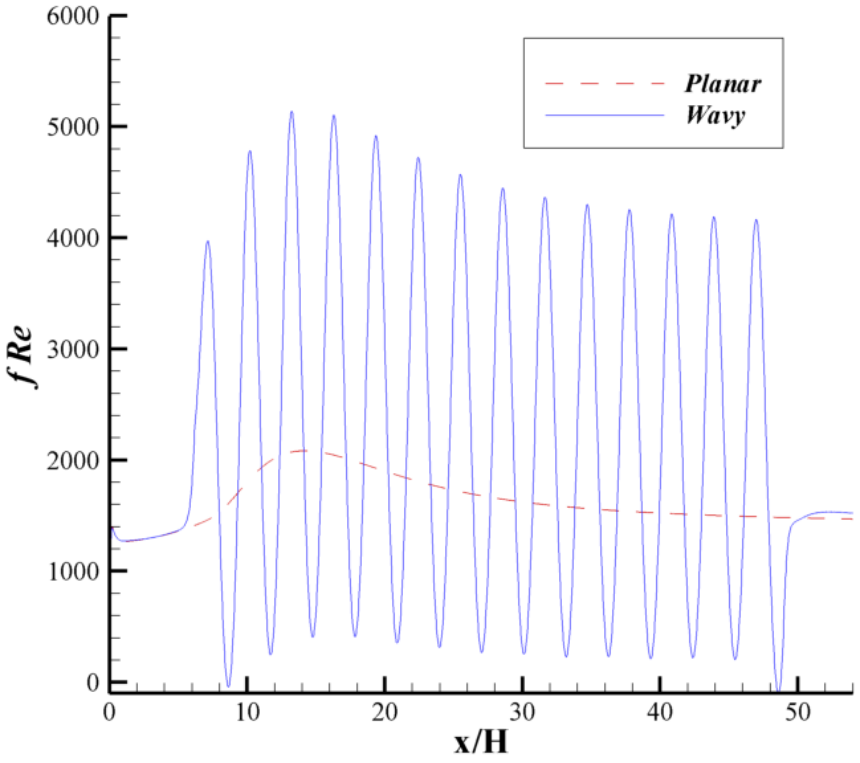

Figure 5.18: Comparison of *f Re* in wavy and planar channels, Re = 7500, T_{wall} = 300 K

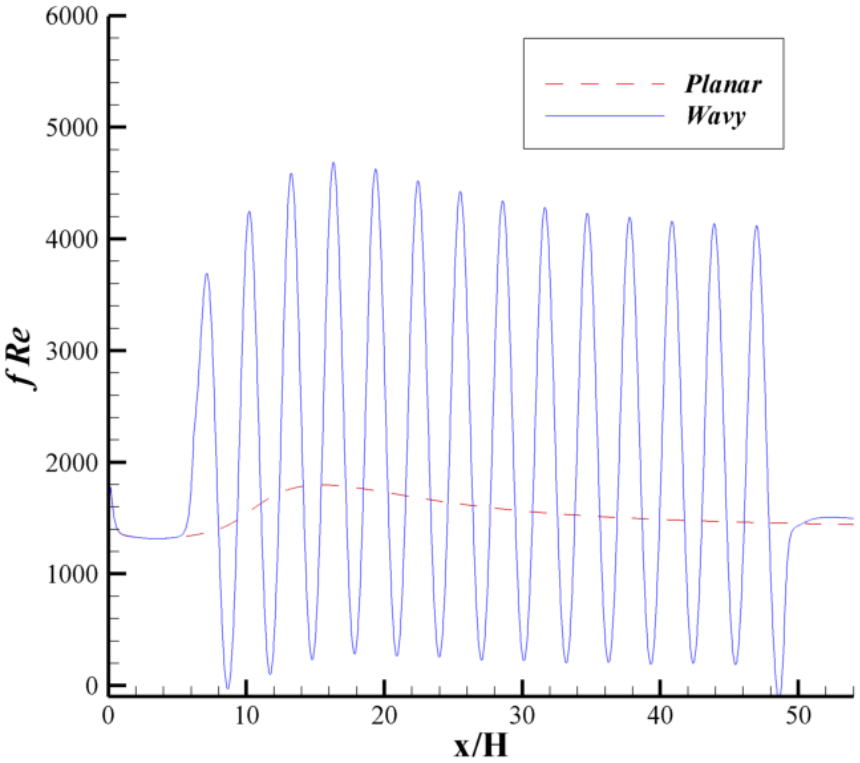

Figure 5.19: Comparison of *f Re* in wavy and planar channels, Re = 7500, T_{wall} = 400 K

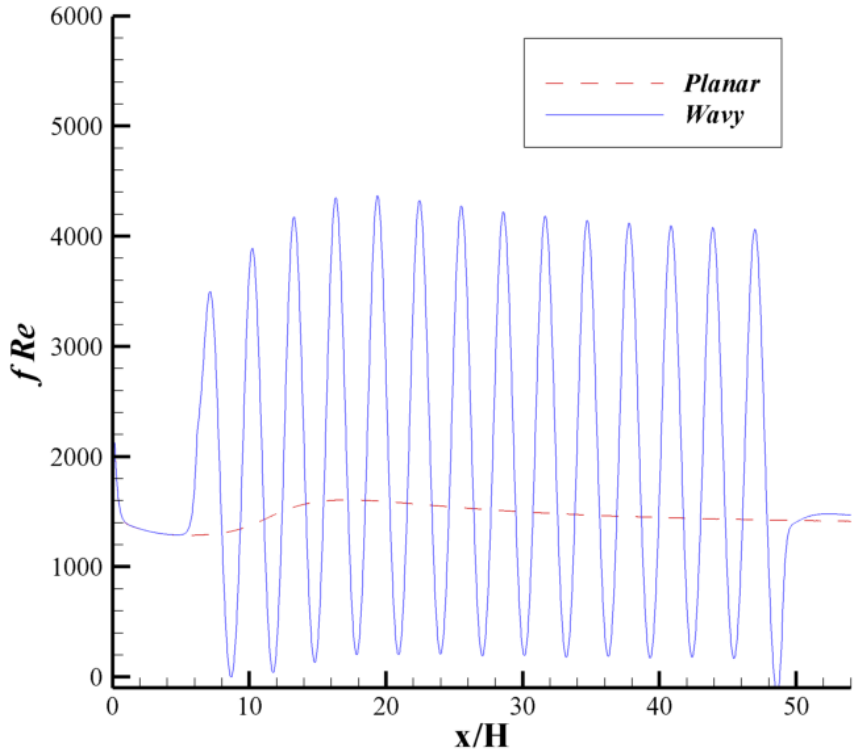

Figure 5.20: Comparison of *f Re* in wavy and planar channels, Re = 7500, T_{wall} = 500 K

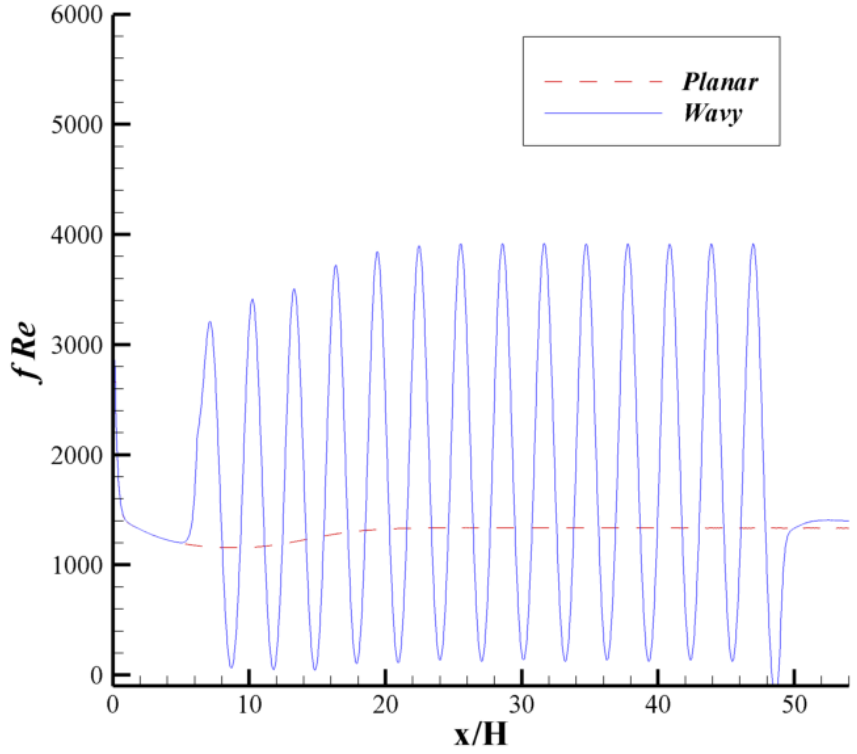

Figure 5.21: Comparison of *f Re* in wavy and planar channels, Re = 7500, T_{wall} = 750 K

In table 5.4 below the total pressure drops for the wavy channel runs and the planar runs can be seen. As expected based on previous research the wavy channel has a much higher pressure drop, roughly 1.5 times as much as the pressure drop in the planar channels.

Table 5.4: Pressure drops [Pa] for wavy and planar channels, Re = 7500

Wall Temperature	Wavy Channel	Planar Channel
300 K	48,961	39,427
400 K	58,073	45,237
500 K	65,448	50,376
750 K	78,489	58,460

5.3.2 Heat Transfer

Predictions for the Nusselt numbers in wavy and planar channels are shown below in figures 5.22, 5.23, and 5.24. Each plot shows a direct comparison of a wavy and a planar channel at a different wall temperature. For all of the cases, the wavy channel Nusselt number oscillates around the planar channel Nusselt number as a result of the wavy geometry. Although the wavy geometry causes peaks in the Nusselt number that are higher than the planar channel values, the average Nusselt number in the wavy channel seems to be lower than in the planar channel. But the Nusselt number near the end of the channel is higher for the wavy channel. Also, similar to the f*Re presented in the previous section, the predicted Nusselt numbers are identical up until the point the waviness begins.

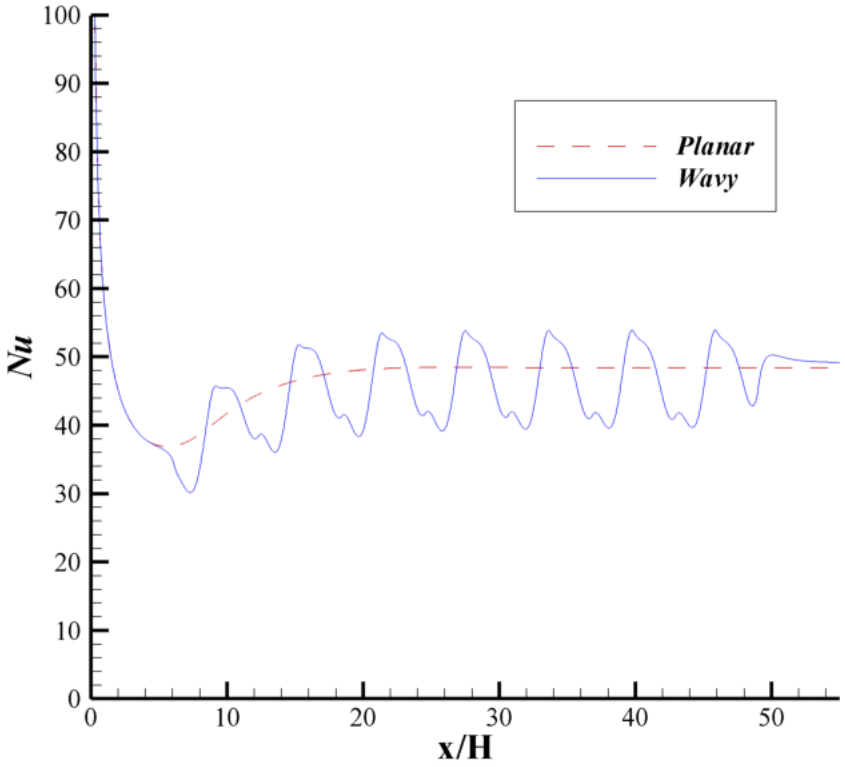

Figure 5.22: Comparison of Nusselt number in wavy and planar channels, Re = 7500, T_{wall} = 300 K

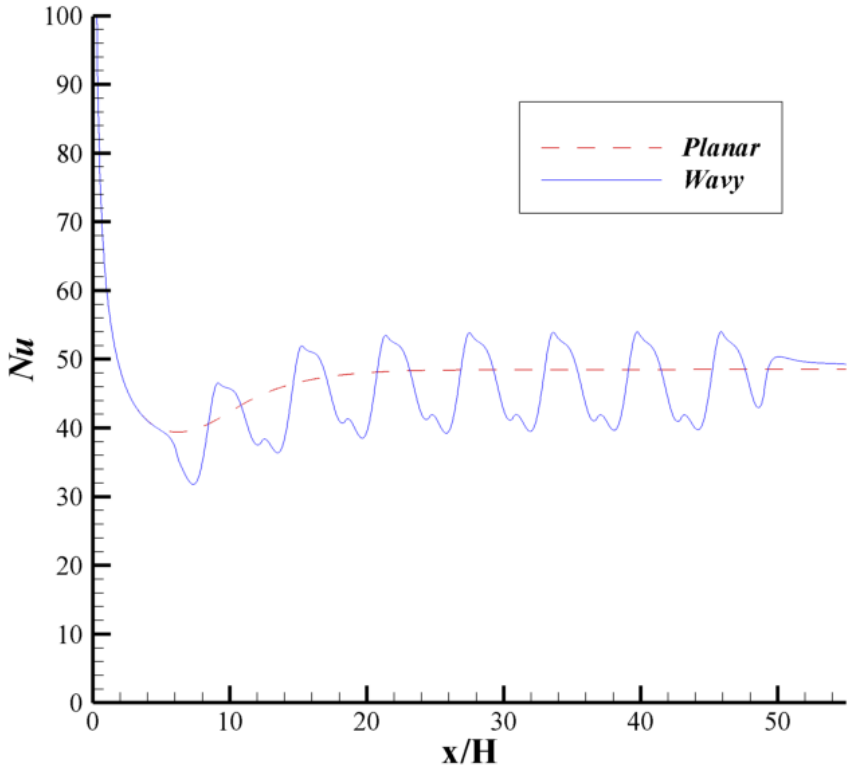

Figure 5.23 Comparison of Nusselt number in wavy and planar channels, Re = 7500, T_{wall} = 400 K

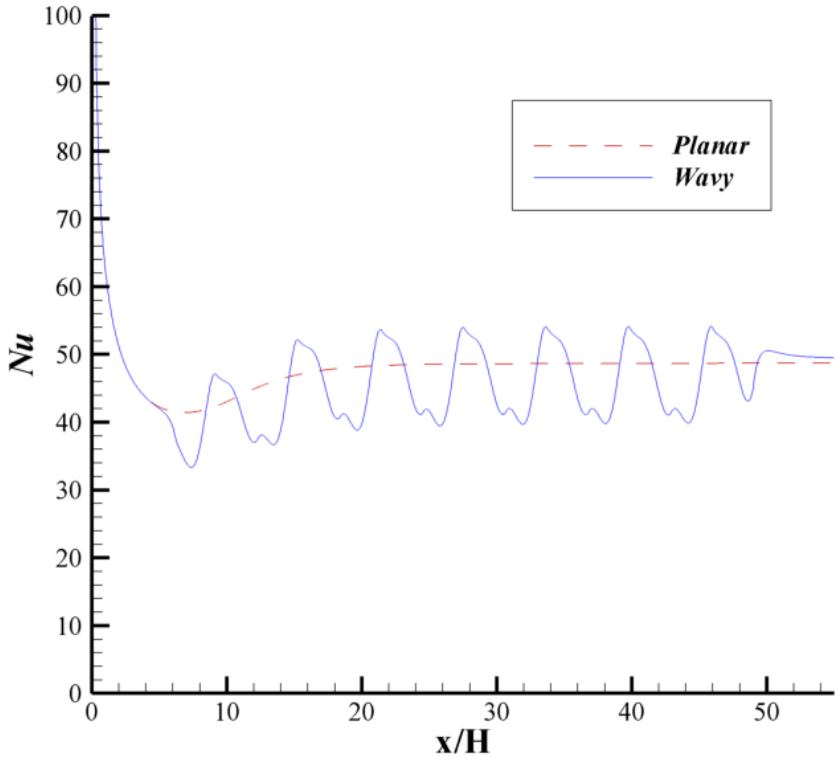

Figure 5.24: Comparison of Nusselt number in wavy and planar channels, Re = 7500, T_{wall} = 500 K

5.3.3 Deposition

Figures 5.25, 5.26, 5.27 and 5.28 show wavy and planar soot deposition along the length of the channel for wall temperatures of 300 K, 400 K, 500 K, and 750 K respectively. As with all of the results in this section the Reynolds number for all runs was set at 7500. All of the plots show that in general the wavy and planar channels follow the same deposition trends. But in all of the plots the two lines diverge and the wavy channel causes more soot to be deposited for all cases.

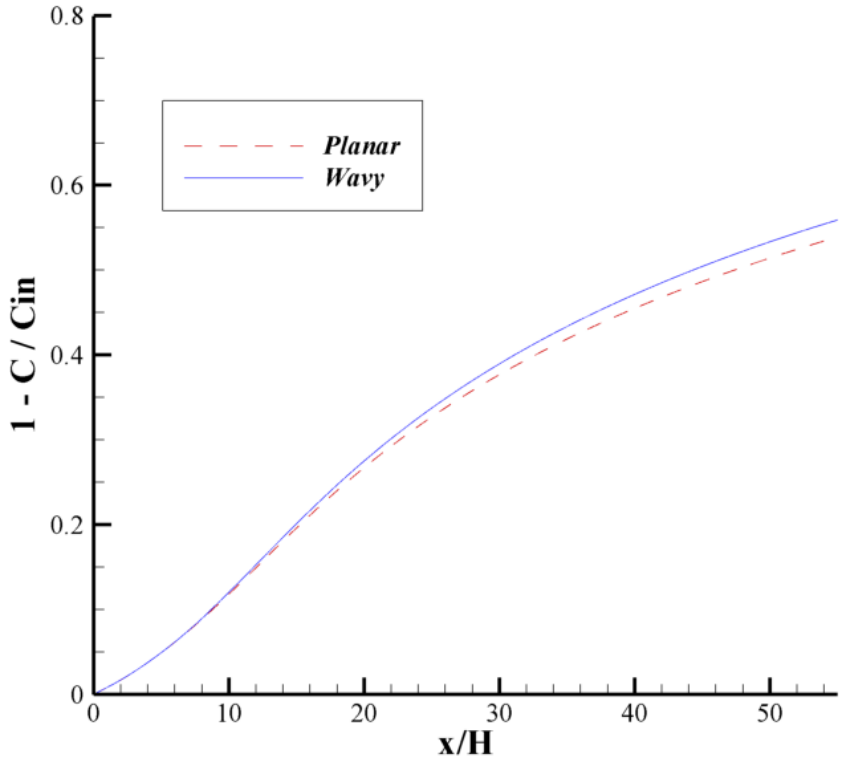

Figure 5.25: Comparison of deposition in wavy and planar channels, Re = 7500, T_{wall} = 300 K

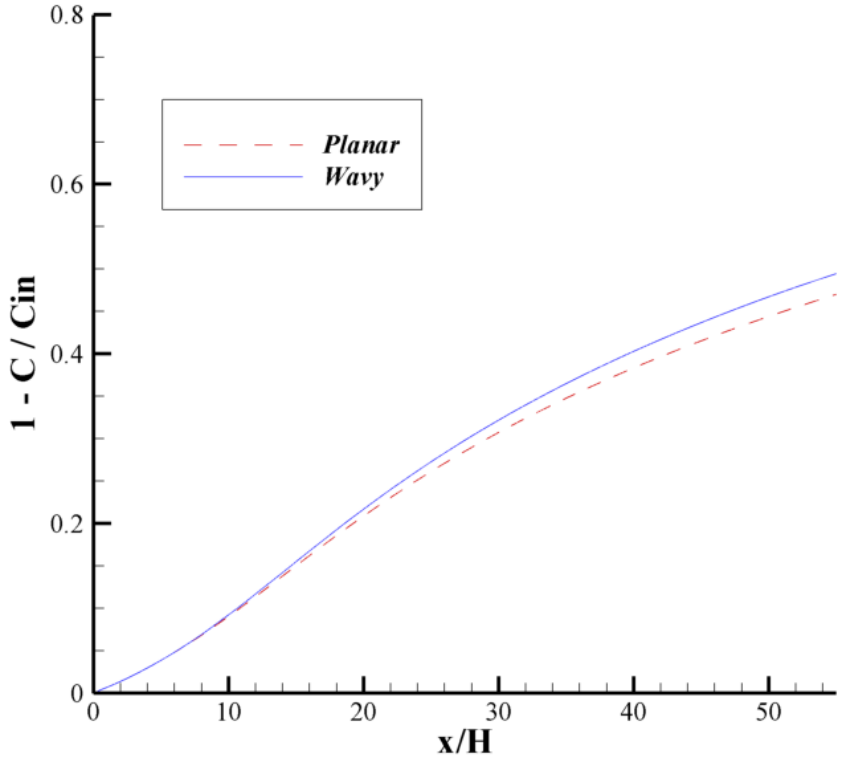

Figure 5.26: Comparison of deposition in wavy and planar channels, Re = 7500, T_{wall} = 400 K

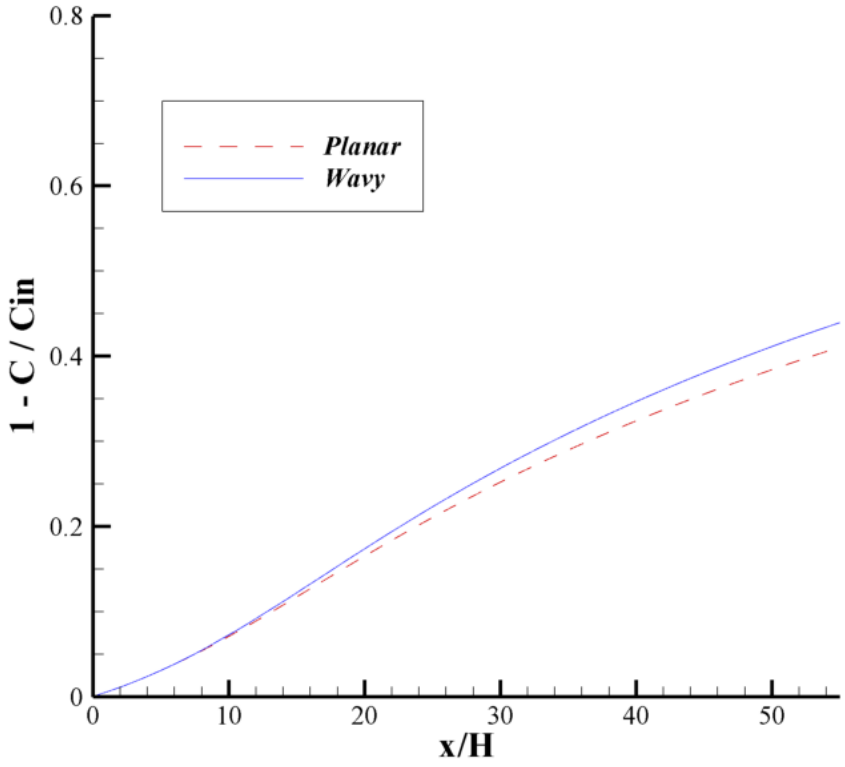

Figure 5.27: Comparison of deposition in wavy and planar channels, Re = 7500, T_{wall} = 500 K

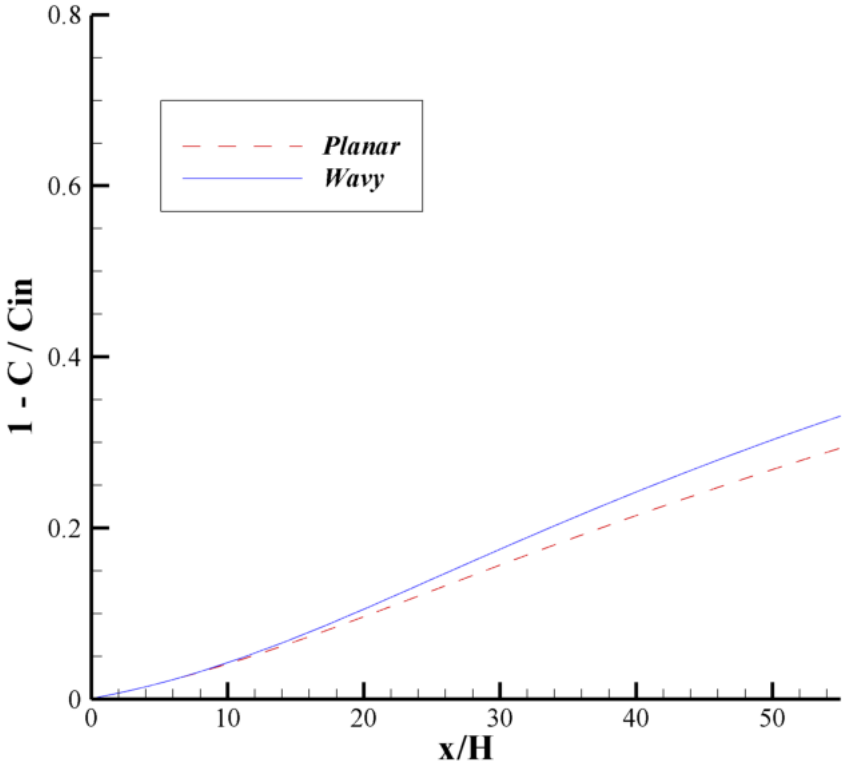

Figure 5.28: Comparison of deposition in wavy and planar channels, Re = 7500, T_{wall} = 750 K

Table 5.5 below summarizes the total deposition for all of the runs, both wavy and planar, for the three different grids used. As with the wavy channel runs in the previous section the grid refinement allows the deposition to be modeled more accurately. The planar channels follow the same trends as the wavy channels, with deposition increasing with increasing temperature gradient. The results show that the deposition in the planar channels is only slightly less than in wavy channels. But the planar channel results are far too high. In a previous study by Goodwin [54], a planar channel with a similar non-dimensional length was studied. For a Reynolds number of 8000 and a wall temperature of 300 K the deposition efficiency was 13.9% which is roughly a quarter of the amount predicted by the current code. For the isothermal case Goodwin's [54] results showed that for a Reynolds number of 8000 the deposition was 0.63%, which is 46 times lower than the current results. When the results were looked at closely, the turbulence model in the current code was converging to a turbulent viscosity nearly three times larger than the code developed by Goodwin [54]. This abnormally large addition to the viscosity causes the predicted soot deposition to increase drastically. The error could be due to either convergence issues caused by the length of the domain or the incorrect behavior of the turbulence model. This needs to be investigated further.

Table 5.5: Summary of total deposition percentage for wavy and planar channels

Reynolds Number	Twall	Wavy Channel			Planar Channel		
		65x2049	129x4097	257x8193	65x2049	129x4097	257x8193
7500	750	90.3%	42.5%	33.2%	86.3%	38.8%	29.5%
7500	500	95.5%	54.2%	44.1%	93.7%	51.6%	41.2%
7500	400	97.0%	59.8%	49.6%	95.9%	57.8%	47.1%
7500	300	98.2%	66.2%	56.0%	97.8%	65.5%	54.8%

5.4 Turbulent Results Summary

This section presented results for turbulent flow in wavy and planar channels. The trends were similar to those found for laminar flow. Once again for wavy channels the pressure drop was shown to increase with increasing wall temperature and decrease with increasing temperature gradient and deposition efficiency was shown to increase with temperature gradient. But the Nusselt number was shown to be nearly independent of both Reynolds number and temperature gradient and the deposition efficiency was shown to increase with increasing Reynolds number. When comparing wavy and planar channels, the pressure drop, heat transfer, and deposition efficiency were all shown to be slightly higher in wavy channels.

Chapter 6

Conclusions

This thesis was focused on modeling the soot deposition in serpentine wavy channels and comparing wavy and planar channels to see the effect of geometry on deposition. A fully implicit BFC code was developed to solve the Navier-Stokes equations in conjunction with the energy and concentration equations. The concentration equation considered both Brownian diffusion and thermophoresis as they are the two dominant deposition mechanisms for nano-particles like soot. Due to the high Schmidt number, a very fine grid is required to accurately model the soot deposition in a turbulent flow. So the concentration equation was solved on two successively finer grids. For turbulent flow the Launder-Sharma k-ε model was employed. Boundary fitted coordinates were used in order to study complex geometries, such as the serpentine wavy channel. Finally because of the high temperature gradient, variable properties were used to accurately model the effect of temperature on the flow. The code was then used to study both laminar and turbulent flow for planar and wavy channels.

The first set of test cases were for laminar flow. Three different Reynolds numbers and four different wall temperatures were used. While performing the runs it was discovered that flow at a Reynolds number of 500 or greater became unsteady, which agreed with previous studies on wavy channel flow. The friction factor times the Reynolds number was shown to oscillate periodically due to the wavy geometry, with peaks in the values occurring every time the flow was required to change direction. Overall the pressure drop was shown to increase with increasing wall temperature and decrease with increasing wall temperature. Compared to the planar channel the pressure drop was larger, as expected. The Nusselt number was also shown to oscillate, and increase with both increasing Reynolds number and increasing temperature gradient. Again, the overall heat transfer was larger for a wavy channel than for a planar channel. Finally the deposition efficiency was shown to increase with temperature gradient and decrease

with Reynolds number. But the decrease with Reynolds number is likely due to the lower fluid residence time for larger Reynolds numbers. The comparison between wavy and planar channels showed that the wavy geometry does cause the deposition to increase.

The second set of results was for turbulent flow in a wavy channel. Similar to the laminar results, three Reynolds numbers and four wall temperatures were used. Once again the wavy geometry caused the product of friction factor and Reynolds number to oscillate and the overall pressure drop to increase. The pressure drop was once again shown to increase with decreasing temperature gradient and increasing Reynolds number. The heat transfer, represented by the Nusselt number, was predicted to oscillate for turbulent flow just like the laminar cases. But the heat transfer was predicted to be nearly independent of Reynolds number and temperature gradient. The heat transfer was also predicted to be only marginally higher for a wavy channel than for a planar channel. Finally the predicted soot deposition was shown to increase with increasing Reynolds number and increasing temperature gradient. This trend does appear correct, but the deposition rates seem high. When planar results were compared to the wavy channel results, they came out very similar, which indicates the code is over predicting deposition for a planar channel. For the isothermal cases the rates are significantly larger when compared with previous results from Goodwin [54]. The error appears to come from the turbulence model. This will be considered in future investigations.

References

[1] "Advancements in Heat Exchange Technology," Modine Manufacturing Company, 2008, http://www.modine.com/v2portal/page/portal/modine/modineTechnologyDefault/ modine com/technology/level 2 content 012.htm.

[2] Schadt, C. and Cadle, R., "Thermal forces on aerosol particles," Journal of Physical Chemistry, Vol. 65, No. 10, 1961, pp. 1689–94.

[3] Brock, J., "On the theory of thermal forces acting on aerosol particles," Journal of Colloid Science, Vol. 17, No. 8, 1962, pp. 768–80.

[4] Talbot, L., Cheng, R.K., Schefer, R.W. and Willis, D.R., 1980, "Thermophoresis of particles in a heated boundary layer," Journal of Fluid Mechanics, 101(4), pp. 737-758.

[5] Tsai, C., Lin, J., Aggarwal, S. and Chen, D., 2004, "Thermophoretic deposition of particles in laminar and turbulent tube flows," Aerosol Science and Technology, 38(2), pp. 131-139.

[6] Leong, K., 1984, "Thermophoresis and diffusiophoresis of large aerosol particles of different shapes," Journal of Aerosol Science, 15(4), pp. 511-517.

[7] Guha, A., 1997, "A unified Eulerian theory of turbulent deposition to smooth and rough surfaces," Journal of Aerosol Science, 28(8), pp. 1517-1537.

[8] Batchelor, G.K. and Shen C., 1985, "Thermophoretic deposition of particles in gas flowing over cold surfaces," Journal of Colloid and Interface Science, 207(1), pp. 21-37.

[9] Bakanov, S., "Future directions for experiments in thermophoresis: A commentary," Journal of Aerosol Science, Vol. 26, No. 1-4, 1995.

[10] Nishio, G., Kitani, S. and Takahashi, K., 1974, "Thermophoretic deposition of aerosol particles in a heat exchanger pipe," Industrial and Engineering Chemistry Process Design and Development, 13(4), pp. 408-415.

[11] Ciro, W.D., Eddings, E.G. and Sarofim, A.F., 2006, "Experimental and numerical investigation of transient soot buildup on a cylindrical container immersed in a jet fuel pool fire," Combustion Science and Technology, 178(12), pp. 2199-2218.

[12] Walker, K.L., Homsy, G.M. and Geyling, F.T., 1979, "Thermophoretic deposition of small particles in laminar tube flow," Journal of Colloid and Interface Science, 69(1), pp. 138-147.

[13] Montassier, N., Boulaud, D., and Renoux, A., "Experimental study of thermophoretic particle deposition in laminar tube flow," Journal of Aerosol Science, Vol. 22, No. 5, 1991, pp. 677–87.

[14] Chang, Y.C., Ranade, M.B. and Gentry, J.W., 1995, "Thermophoretic deposition in flow along an annular cross-section: Experiment and simulation," Journal of Aerosol Science, 26(3), pp. 407-428.

[15] Chiou, M.C. and Cleaver, J.W., 1996, "Effect of thermophoresis on sub-micron particle deposition from a laminar forced convection boundary layer flow onto an isothermal cylinder," Journal of Aerosol Science, 27(8), pp. 1155-1167.

[16] Messerer, A., Niessner, R. and Poschl, U., 2003, "Thermophoretic deposition of soot aerosol particles under experimental conditions relevant for modern diesel engine exhaust gas systems," Journal of Aerosol Science, 34(8), pp. 1009-1021.

[17] Lee, B.U., Byun, D.S., Bae, G.N. and Lee, J.H., 2006, "Thermophoretic deposition of ultrafine particles in a turbulent pipe flow: Simulation of ultrafine particle behavior in an automobile exhaust pipe," Journal of Aerosol Science, 37(12), pp. 1788-1796.

[18] Lin, J., Tsai, C., 2003, "Thermophoretic deposition efficiency in a cylindrical tube taking into account developing flow at the entrance region," Journal of Aerosol Science, 34(5), pp. 569-583.

[19] Sasse, A.G., Nazaroff, W.W. and Gadgil, A.J., 1994, "Particle filter based on thermophoretic deposition from natural convection flow," Aerosol Science and Technology, 20(3), pp. 227-238.

[20] Changfu, Y. and Guanghui, L., 2008, "Direct numerical simulation of microparticle motion in channel flow with thermophoresis," Journal of Environmental Engineering, 134(2), pp. 138-144.

[21] Zahmatkesh, I., 2008, "On the importance of thermophoresis and Brownian diffusion for the deposition of micro and nanoparticles," International Communications in Heat and Mass Transfer, 35(3), pp. 369-375.

[22] He, C. and Ahmadi, G., 1998, "Particle deposition with thermophoresis in laminar and turbulent flows," Aerosol Science and Technology, 29(6), pp. 525-546.

[23] Chein, R. and Liao, W., 2005, "Thermophoretic effects on nano-particle deposition in channel flow," Heat and Mass Transfer, 42(1), pp. 71-79.

[24] Pratsinis, S. and Kim, K., 1989, "Particle coagulation, diffusion and thermophoresis in laminar tube flows," Journal of Aerosol Science, 20(1), pp. 101-111.

[25] Neer, A. and Koylu, U.O., 2006, "Effect of operating conditions on the size, morphology, and concentration of submicrometer particulates emitted from a diesel engine," Combustion and Flame, 146(1-2), pp. 142-154.

[26] Assanis, D., Hoard, J., Abarham, M., and Goje, A., "EGR Cooler Fouling," Walter E. Lay Automotive Laboratory, University of Michigan, 2009, http://me.engin.umich.edu/autolab/Projects/EGRCoolerFouling.html.

[27] Zhang,W. and Watkinson, A. P., "Carbonaceous Material Deposition from Heavy HydrocarbonVapors. 2. Mathematical Modeling," Journal of Industrial Engineering and Chemical Research, Vol. 44, 2005, pp. 4092-98.

[28] Nishimura, T., Ohori, Y., and Kawamura, Y., "Flow characteristics in a channel with symmetric wavy wall for steady flow," Journal of Chemical Engineering of Japan, Vol. 17, No. 5, 1984, pp. 466–71.

[29] Nishimura, T., Ohori, Y., and Kawamura, Y., "Mass transfer characteristics in a channel with symmetric wavy wall for steady flow," Journal of Chemical Engineering of Japan, Vol. 18, No. 6, 1985, pp. 450–5.

[30] Nishimura, T., Kajimoto, Y., Tarumoto, A., and Kawamura, Y., "Flow structure and mass transfer for a wavy channel in transitional flow regime," Journal of Chemical Engineering of Japan, Vol. 19, No. 5, 1986, pp. 449–55.

[31] Asako, Y., Nakamura, H., and Faghri, M., "Heat transfer and pressure drop characteristics in a corrugated duct with rounded corners," International Journal of Heat and Mass Transfer, Vol. 31, No. 6, 1988, pp. 1237–45.

[32] Oyakawa, K., Shinzato, T., and Mabuchi, I., "The effects of the channel width on heat-transfer augmentation in a sinusoidal wave channel," JSME International Journal, Vol. 32, No. 3, 1989, pp. 403-10.

[33] Wang, G. and Vanka, S., "Convective heat transfer in periodic wavy passages," International Journal of Heat and Mass Transfer, Vol. 38, No. 17, 1995, pp. 3219–30.

[34] Rush, T., Newell, T., and Jacobi, A., "An experimental study of flow and heat transfer in sinusoidal wavy passages," International Journal of Heat and Mass Transfer, Vol. 42, No. 9, 1999, pp. 1541–53.

[35] Stone, K. and Vanka, S. P., "Numerical Study of Developing Flow and Heat Transfer in a Wavy Passage," Journal of Fluids Engineering, Vol. 121, 1999, pp. 713-19.

[36] Zhang, J., Kundu, J., and Manglik, R., "Effect of fin waviness and spacing on the lateral vortex structure and laminar heat transfer in wavy-plate-fin cores" International Journal of Heat and Mass Transfer, Vol. 47, 2004, pp. 1719-30.

[37] Metwally, H. and Manglik, R., "Enhanced heat transfer due to curvature-induced lateral vortices in laminar flows in sinusoidal corrugated-plate channels," International Journal of Heat and Mass Transfer, Vol. 47, No. 10-11, 2004, pp. 2283–92.

[38] Manglik, R., Zhang, J., and Muley, A., "Low Reynolds number forced convection in three-dimensional wavy-plate-fin compact channels: fin density effects," International

Journal of Heat and Mass Transfer, Vol. 48, No. 8, 2005, pp. 1439–49.

[39] Muley, A., Borghese, J., Manglik, R. M., and Kundu, J., "Experimental and numerical investigation of thermal-hydraulic characteristics of wavy-channel compact heat exchanger," Proceedings of the 12th International Heat Transfer Conference, Vol. 4, 2002, pp. 417-22.

[40] Gradeck, M., Hoareau, B., and Lebouche, M., "Local analysis of heat transfer inside corrugated channel," International Journal of Heat and Mass Transfer, Vol. 48, No. 10, 2005, pp. 1909–15.

[41] Xie, G., Wang, Q., Zeng, M., and Luo, L., "Numerical investigation of heat transfer and fluid flow characteristics inside a wavy channel," Heat and Mass Transfer, Vol. 43, No. 7, 2007, pp. 603–11.

[42] Youn, B. and Kim, N., "An experimental investigation on the airside performance of fin-and-tube heat exchangers having sinusoidal wave fins," Heat and Mass Transfer, Vol. 43, No. 12, 2007, pp. 1249–62.

[43] Naphon, P., "Effect of corrugated plates in an in-phase arrangement on the heat transfer and flow developments" International Journal of Heat and Mass Transfer, Vol. 51, 2008, pp. 3963-71.

[44] Radhmehr, A. and Patankar, S. V., "Computation of boundary layer transistion Using Low-Reynolds number turbulence models," Numerical Heat Transfer, Vol. 39, Part B, 2001, pp. 525-43.

[45] Goldstein, L. and Sparrow, E., "Heat/mass transfer characteristics for flow in a corrugated wall channel," Journal of Heat Transfer, Vol. 99, No. 2, 1977, pp. 187–94.

[46] O'Brien, J. and Sparrow, E., "Corrugated-duct heat transfer, pressure drop, and flow visualization," Transactions of the ASME. Journal of Heat Transfer, Vol. 104, No. 3, 1982, pp. 410–6.

[47] Patel, V. C., Chon, J. T., and Yook, J. Y., "Turbulent flow in a channel with a wavy wall," Journal of Fluids Engineering, Vol. 113, 1991, pp. 579-86.

[48] Snyder, B., Li, K. T., and Wirtz, R. A., "Heat transfer enhancement in a serpentine channel," International Journal of Heat and Mass Transfer, Vol. 36, No. 12, 1993, pp. 2965-76.

[49] Kays, W. M. and London, A. L., Compact Heat Exchangers (3rd Edition), McGraw-Hill, 1984, pp. 204.

[50] Gschwind, P., Regele, A., and Kottke, V., "Sinusoidal wavy channels with Taylor – Goertler vorticies," Experimental Thermal and Fluid Science, Vol. 11, 1995, pp. 270-275.

[51] Maaß, C. and Schumann, U., "Direct Numerical Simulation of Separated Turbulent Flow over a Wavy Boundary," Notes on Numerical Fluid Mechanics, Vol. 52, 1996, pp. 227-41.

[52] Dellil, A., Azzi, A., and Jubran, B., "Turbulent flow and convective heat transfer in a wavy wall channel," Heat and Mass Transfer, Vol. 40, No. 10, 2004, pp. 793–9.

[53] Pham, M., Plourde, F., and Doan, S., "Turbulent heat and mass transfer in sinusoidal wavy channels," International Journal of Heat and Fluid Flow, Vol. 29, No. 5, 2008, pp. 1240–57.

[54] Goodwin, M. A., "Numerical Study of Thermophoretic Deposition in Planar and Wavy Channels," Master's Thesis, 2009, University of Illinois at Urbana Champaign.

[55] Stull, D., "Vapor Pressure of Pure Substances," Industrial and Engineering Chemistry, Vol. 39, No. 4, 1947, pp. 517–40.

Appendix A

Condensate Model

A.1 Introduction

Although the main topic of this thesis was the deposition of soot, the condensation of hydrocarbons is another cause of fouling in EGR coolers. Hydrocarbons condensation is a phenomenon that depends highly on the pressure and temperature of the fluid. This appendix covers a simple model added to the main code to model the creation and deposition of condensates. The methods used to model the condensation will first be discussed in detail, and then some initial results will be presented.

A.2 Methods

In order to model the condensation of hydrocarbons two more concentration models were added to the code. Both models used a simplified form of the concentration equation shown below with *S* being the source term.

$$\frac{\partial}{\partial t}(\rho c) + \frac{\partial}{\partial x}(\rho u c) + \frac{\partial}{\partial y}(\rho v c) = \frac{\partial}{\partial x}\left(D\frac{\partial T}{\partial x}\right) + \frac{\partial}{\partial y}\left(D\frac{\partial T}{\partial y}\right) + S \qquad \text{(A.1)}$$

One equation tracks the hydrocarbons coming into the channel and has a negative source term that subtracts hydrocarbon concentration after the dew point temperature is reached. The second equation tracks the condensates formed by adding the same source term that was subtracted from the hydrocarbon model to its source term. The source term assumes that all of the hydrocarbons coming into a control volume condense as soon as the local temperature drops below the dew point temperature. The first equation has a set inlet concentration of hydrocarbons and a zero gradient boundary condition on the wall. The condensate model has a no slip

condition on the walls and a zero inlet condition. Both models have a zero gradient boundary condition at the outlet as well. Both equations were then solved using the methods presented in chapter 3.

In order to determine the dew point temperature, the charts from Stull [55] were used. The first table presented in [55] has the dew temperatures for organic compounds below atmospheric pressure and the second table has them for pressures above atmospheric pressure. Since the system pressure for our runs was 250,000 Pa, which is roughly 2.5 times atmospheric pressure, values above atmospheric pressure are needed. The hydrocarbon used in this study was HC5, but Stull [55] only presents data at atmospheric pressure and below. So in order to extrapolate, the data from the first table was plotted and a curve fit equation was found. The plot and the curve fit equation are shown below in figure A.1.

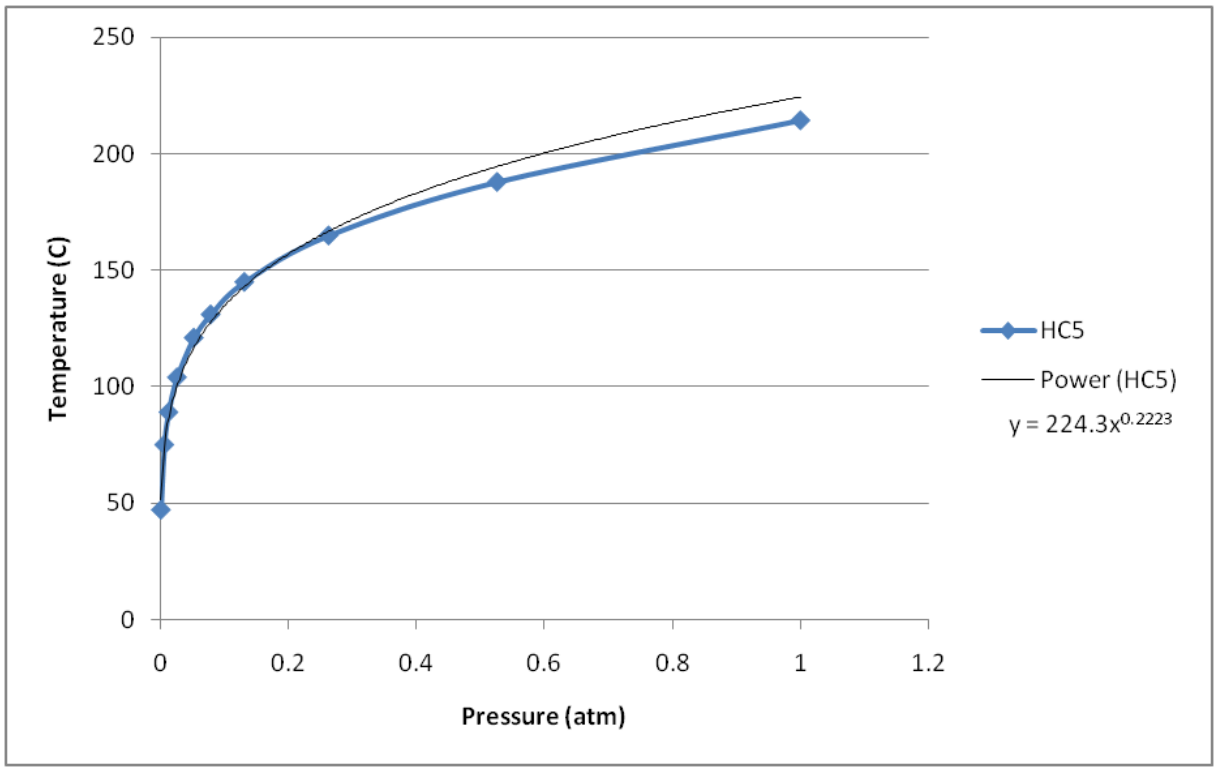

Figure A.1: Dew Point curve for HC5

The equation fits very well, but to be sure its valid a compound with values listed both above and below atmosperic pressure was checked using the same process. The compound $C_{12}H_{26}$ is listed in both tables so it was used as an example. The plot of the data below atmospheric pressure and curve fit are shown below in figure A.2.

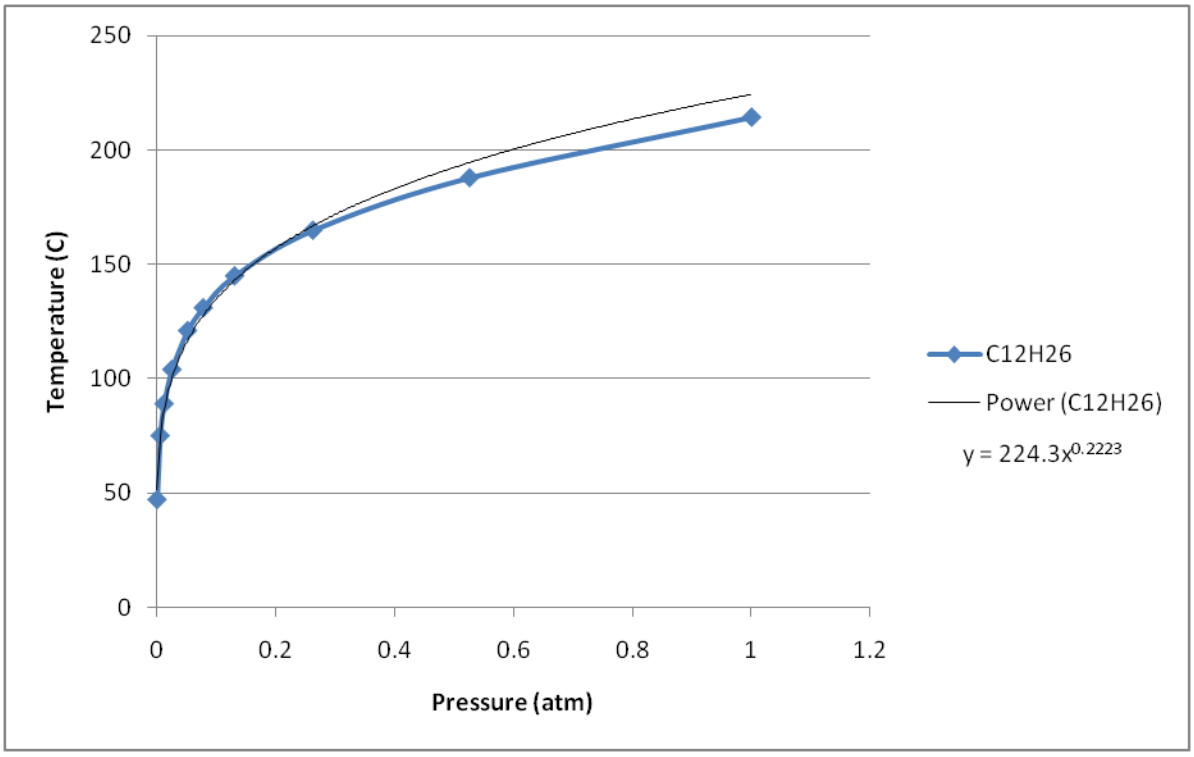

Figure A.2: Dew Point curve for $C_{12}H_{26}$

The curve does not fit as well but it is still good. The value given for $C_{12}H_{26}$ at 2 atmospheres is 248.2 degrees celcius. Using the curve fit equation from figure A.2 it is predicted to be 261.67 degrees celcius. This is higher than it should be but this makes sense since the curve fit shows the same trend. Using the equation in figure A.1 the dew point temperature at 2.5 atmospheres was estimated to be 437.5 degrees Celcius which is roughly 710K.

A.3 Initial Results

A run was performed for a planar channel at a Reynolds number of 6500 with an inlet temperature of 750 K and a wall temperature of 500 K . The channel was 2 mm high and 32 mm long. The inlet concentration was set at 63.735 ppm based on data provided by Modine Manufacturing Company and the dew point temperature was set as 710K. Contour plots of hydrocarbons and condensates can be seen below in figures A.3 and A.4.

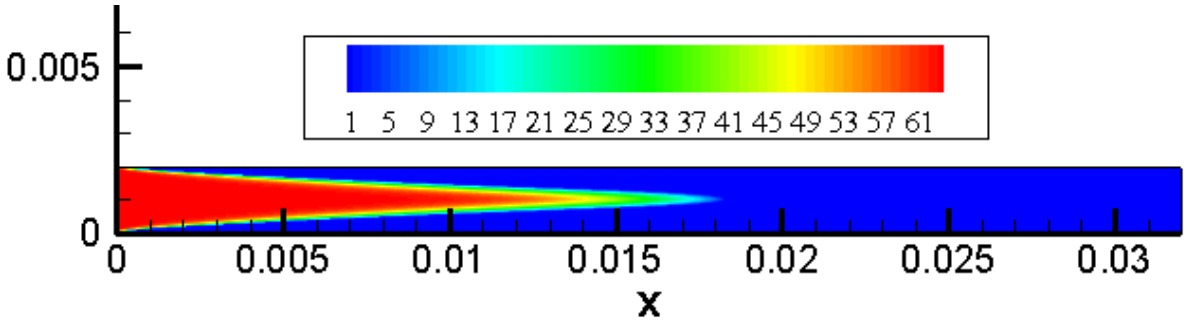

Figure A.3: Contour plot of hydrocarbon concentration, Re = 6500 and Twall = 500 K

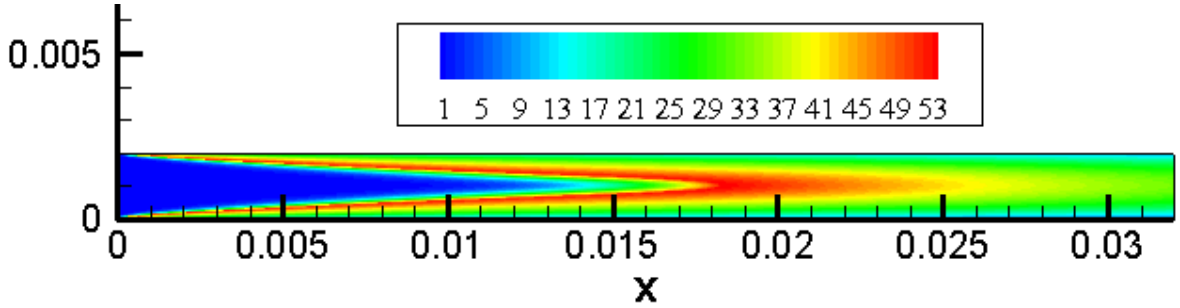

Figure A.4: Contour plot of condensate concentration, Re = 6500 and Twall = 500 K

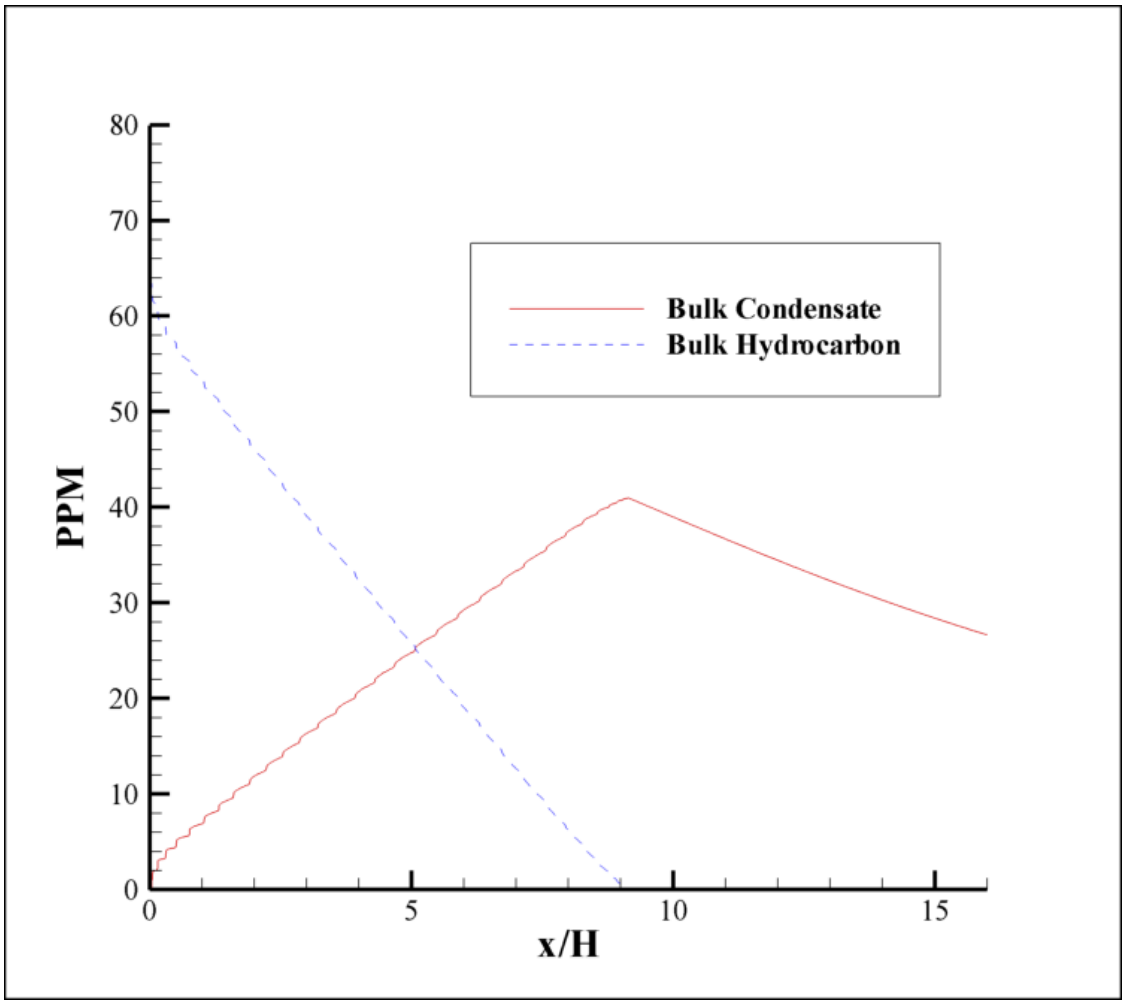

Figure A.5: Condensate and Hydrocarbon Levels, Re = 6500 and Twall = 500 K

The trends seem reasonable and the code appears to be working correctly. The results in figure A.5 show all of the hydrocarbons being condensed, but not all of the condensates collecting on the walls. Without experimental results to compare this numerical model to, it is difficult to state whether or not the results are realistic. But parameters such as the dew point temperature and diffusion coefficients can be changed to match experimental data once it becomes available.